JOHANN WOLFGANG GOETHE
UNIVERSITÄT
FRANKFURT AM MAIN

Master's Thesis

Investigation of electron beam assisted density boosting in plasma traps using the example of a Gabor plasma lens

May 3, 2017

Author:
Christoph Beberweil

Supervisors:
Prof. Dr. Holger Podlech
Dr. Kathrin Schulte

Institut für Angewandte Physik

NNP
Non Neutral Plasma
Physics Group

Abstract

The aim of this thesis is finding a geometric configuration that allows electron insertion into a Gabor plasma lens in order to increase the density of the confined electrons and provide ignition conditions at parameters where ignition is not possible. First, simulations using CST and bender were conducted to investigate several geometric configurations in terms of their performance of inserting electrons manually. One particular design has been chosen as a basis for an experiment. In order to prepare the experiment, further simulations using the code bender have been conducted to investigate the density distribution that is formed inside the Gabor lens when inserting electrons transversally in compliance with the chosen design. Additionally, bender was used to investigate the impact of the initial electron energy on the distribution inside the lens. Simulations with and without space charge effects have shown a significant impact of the space charge effects on the resulting density distribution. Therefore, space charge effects have proven to be the major electron redistribution process.

A given electron source was characterised in order to find the performance under the conditions inside a Gabor lens. In particular, a transversal magnetic field that will be present in the experiment has to be compensated by shielding the inner regions of the source by a μ-metal layer. Using a μ-metal shield, transversal magnetic fields are sufficiently tolerable to perform measurements in a Gabor lens. Additionally, operating close to 100 eV electron energy yields a maximum in the emitted current. Adding a Wehnelt cylinder to the electron source furthermore improves the extracted current to roughly 1 mA.

A test stand consisting of a newly designed anode for the Gabor lens, as well as a terminal for the electron source, was constructed. The electron source was thoroughly characterised in the environment of the Gabor lens and the ignition properties of the new system were evaluated. In further experiments, electron beam assisted ignition by increasing the residual gas pressure was observed and the impact of the position of the electron source on the ignition properties was investigated. In addition, ignition of a sub-critical state, that is a state consisting of potential, magnetic field and pressure that did not yet perform ignition by itself, was performed by increasing the extracted current from the electron source. Finally, the electron source was used to influence a pre-ignited plasma. The density was measured, which was increased by the use of the electron source in most cases.

This project is part of the EDEN collaboration (Electron DENsity boosting) of the NNP Group at IAP Frankfurt with INFN institutes in Bologna and Catania.

Contents

Motivation

Ion beams offer a magnitude of applications in science, engineering and astronautics. In many implementations, a good beam quality is desirable. If left to their own dynamics, low energy ion beams diverge, since the positive or negative charge of the ions acts repulsively on themselves while at higher energies, the magnetic field created by the current in the beam aids in focusing. Therefore, focusing devices are developed with the intention of preserving beam quality as the beam has to be transported in a Low Energy Beam Transport (LEBT) section. The distances a beam travels in an accelerator structure varies between a few meters or less in small devices up to several kilometres in the largest structures. The larger the covered distance is, the better the beam quality has to be.

One among many focusing devices is the Gabor plasma lens. It was developed during the mid-20^{th} century by Dennis Gabor [1]. Unlike similar devices, the Gabor lens does not directly use magnetic or electric fields to achieve a focusing effect on an ion beam. Instead, the fields are used in order to create a confinement for electrons, which form a non-neutral plasma inside the Gabor lens. The electric field created by the space charge of the enclosed electron cloud is used for focusing.

A disadvantage of the Gabor lens is that it relies on a certain amount of residual gas inside the vacuum cavity, so that the electrons forming the non-neutral plasma can be created by ionization of the gas. In a LEBT section of a given accelerator, the residual gas pressure tends to be larger than in other parts of the accelerator structure. Therefore, Gabor lenses can be utilized in the LEBT, while operating a Gabor lens in later accelerator stages is increasingly difficult due to the improving vacuum conditions. Unfortunately, this potentially prevents the use of Gabor lenses in accelerator structures that need a very high quality vacuum, for instance storage rings or high energy sections.

As a solution, the application of electron emitters has been proposed so that a Gabor lens can be operated in ultra-high vacuum. Some accelerator structures use superconductive materials for magnets or resonators. These need to be cooled down close to absolute zero in order to achieve superconductivity. Using cheap thermal electron sources in such a milieu would deposit unnecessary heat into a cryostat. Therefore, the use of field emission electron sources is highly encouraged. Furthermore, this would allow the Gabor lens to be directly part of an cryostat, simplifying the construction of accelerators. Electron sources that rely on field emission and use carbon nano tubes (CNT) in order to achieve a very slim and sharp tip for the field emission seem to be the most promising technology for this project.

The aim of this Master's thesis is to find a geometric configuration that allows the filling of non-neutral electron plasma into a Gabor lens from external electron sources in order to increase the confined density and to achieve ignition at parameters where classical ignition is not possible. Furthermore it has been shown before that electron sources can be used to boost the plasma density in ECR ion sources [2]. Therefore, a second possible benefit from electron sources could be an increased density in the Gabor lens, resulting in a superior focussing performance.

The following problems arise: First, electrons that are injected longitudinally will pass the lens almost completely, as the electric potential used for confinement in this direction is symmetric. The applied magnetic field prevents transversal injection, as the resulting Lorentz force acts azimuthally and thus provides the electron confinement in radial direction. Presumably, electrons that are injected transversally will not be able to move radially inside the lens and form a homogeneous distribution.

In the course of this thesis, simulations will show useful positions of the electron emitters inside the Gabor lens. Furthermore, measurements with a Gabor lens based on a Helmholtz

configuration will test the results of the simulation. The density of captured electrons is expected to increase due to the electron emitters. As a next step, but not in the scope of this thesis, the entire lens could be investigated in a cryostat, so that a high-quality vacuum in the magnitude of 10^{-9} mbar can be achieved. In this case, the electron production by residual gas ionisation is suppressed and the electron emitter becomes the major source of electrons. Since the experiments shown in this thesis are not performed in a cryostat, a thermal electron source was used for the measurements.

The goal of the EDEN collaboration is to investigate the possibility of boosting the electron density in a plasma trap and provide ignition conditions in a system that is not able to ignite naturally by using an external electron source. Apart from the application in a Gabor lens, these principles are also interesting for boosting the electron density in ion sources. Our partners in Italy are, amongst other things, experienced in the field of electron sources in general and CNT sources in particular. The NNP Group provides expertise in Gabor lens systems and advanced simulation codes.

Chapter 1

Theory

1.1 Some historical designs of Gabor lenses

As early as 1947, the physicist Dennis Gabor, who invented the Gabor lens, raised the question of how electrons could be filled into a lens volume[1]. He proposed a setup with two coils generating a cusp-shaped magnetic field. In this area, he installed a circular filament providing electrons. A sketch of this design is shown in figure 1.1a. Other experiments used a similar design. John Palkovic [3] also used two coils to create a cusp shaped field, compare figure 1.1b. He found that the cusp increases the stability of the plasma, along with the losses, but he did not utilize an electron-providing ring in the cusp.

These are two examples of historical Gabor lens design. Far more prototypes have been developed and tested in experiments. Various prototypes were designed at IAP, compare figure 1.2. In these designs, the shape of the anode is varied and the second coil present in the design by Gabor and Palkovic has been removed. Furthermore, both a solenoid and a Helmholtz coil configuration were tested and additional concepts were investigated, such as a segmented anode in order to control the potential distribution inside the plasma chamber or an array of three Helmholtz coil pairs in a row in order to vary the magnetic field along the symmetry axis of the system. Varying the potential distribution was found to be of little use and was discarded in [3]. In spite of these results, a 90°-segmented anode was installed and is currently being tested in a Gabor lens prototype in Frankfurt [4].

1.2 Basic principles of the Gabor lens

1.2.1 Construction

A space charge lens designed by Gabor consists of a magnetic field in beam direction, which may be provided by a solenoid or a pair of Helmholtz coils. Furthermore, a cylindrical electrode

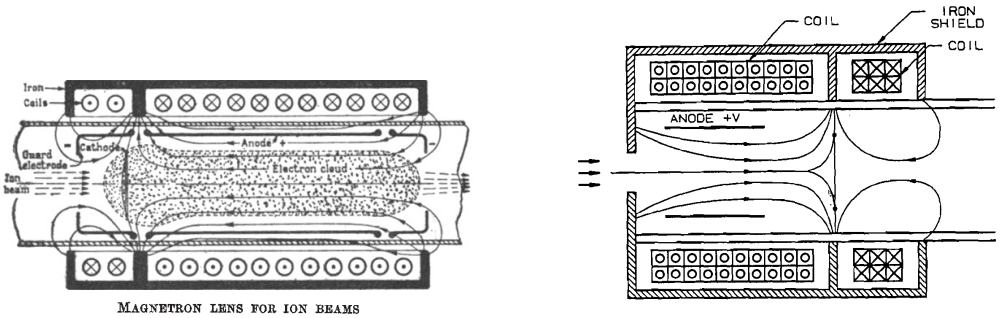

(a) Design by Gabor [1].

(b) Design by Palkovic [3].

Figure 1.1: Different historical designs of the Gabor lens.

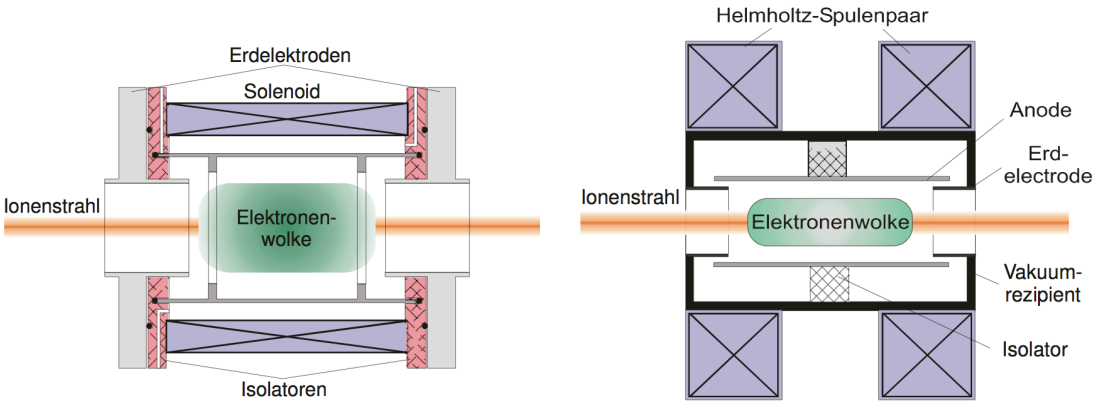

Figure 1.2: Schematics of a Gabor lens. Both a solenoid and a pair of Helmholtz coils can be used to create the magnetic field. Furthermore, the anode stucture can be complex or a simple cylinder. Taken from [5].

system comprising an anode and two ground electrodes is applied. The magnetic field provides confinement in radial direction, while the electric field provides confinement in longitudinal direction.

1.2.2 Confinement of electrons

Radial confinement

The radial confinement is achieved by a solenoid or Helmholtz coil structure, which provide an almost homogeneous magnetic field in beam direction. In order to deduct the theoretical confinement conditions, we assume a cylindrical uniform distribution of the electrons without any other charge carriers, so that the diamagnetic field caused by the rotation of the electrons can be neglected. Furthermore, it is assumed that the ensemble is cold such that the thermal velocity is small against the drift velocity.

Davidson [6] outlines the theoretical confinement similar to the following calculations. We consider the force equilibrium of an electron at a certain radius from the symmetry axis. The centrifugal force acts because of the circular trajectory of a charged particle in a magnetic field. Furthermore, the electrostatic force of the uniform non-neutral plasma acts outwards. Finally, the Lorentz force of the magnetic field itself has to be considered. The centrifugal and the electrostatic force both act outwards, while the Lorentz force acts inwards, which leads to the force balance equation:

$$0 = eE_r - ev_\theta B_z + \frac{mv_\theta^2}{r} \tag{1.1}$$

We calculate the electric vector field $\mathbf{E}$ of the electrons enclosed by a cylinder with normal vector on the lateral area $\mathbf{a}$ with the Gaussian method:

$$\begin{aligned} \oint \mathbf{E}\mathrm{d}\mathbf{a} &= \frac{q_{\mathrm{enc}}}{\epsilon_0} \\ q_{\mathrm{enc}}(r) &= enl\pi r^2 \\ \mathrm{d}\mathbf{a} &= 2l\pi\mathrm{d}\mathbf{r} \end{aligned}$$

First, both $\mathbf{E}$ and $\mathbf{a}$ are parallel, so the integral simplifies to a one dimensional calculation. Since the magnitude of the electric field E is constant on the cylinder surface, the electric field and the integral commute, thus the integral can be solved and yields the lateral surface of the cylinder. Assuming a homogeneous electron density, the enclosed charge q_{enc} can be expressed in terms of

the radius of the cylinder:

$$2E_r l\pi r = \frac{1}{\epsilon_0} enl\pi r^2$$
$$E_r = \frac{ne}{2\epsilon_0} r$$

Here, n denotes the numerical density of electrons measured in $1/\mathrm{m}^3$. Furthermore, the electric field can be expressed by the plasma frequency:

$$\omega_p^2 = \frac{e^2 n}{\epsilon_0 m} \tag{1.2}$$
$$E_r = \frac{m\omega_p^2}{2e} r \tag{1.3}$$

Using the definition of angular velocity $\omega = \frac{v_\theta}{r}$ of a single particle around the symmetry axis and the cyclotron frequency $\Omega = \frac{eB}{m}$, equation 1.1 can be rewritten in terms of the various angular frequencies:

$$0 = \omega^2 - \omega\Omega + \frac{\omega_p^2}{2}$$

Here, $\omega\Omega$ results from the Lorentz force which points inwards. Therefore, it has a negative sign. This is a quadratic equation and it is solved by:

$$\omega_\pm = \frac{\Omega}{2} \pm \sqrt{\frac{\Omega^2}{4} + \frac{\omega_p^2}{2}} = \frac{\Omega}{2}\left(1 \pm \sqrt{1 - \frac{2\omega_p^2}{\Omega^2}}\right) \tag{1.4}$$

The result shows two possible angular frequencies of rotation around the symmetry axis. ω_- corresponds to a slow rotation, while the rotation mode with ω_+ is faster. Note that neither of these frequencies depend on the radius. Therefore, they both correspond to a rigid rotation. Nevertheless, although both frequencies are valid roots of equation (1.4), for a system with given electron initial velocities, either ω_+ **or** ω_- is present depending on the initial conditions and therefore the whole plasma column rotates uniformly.

Considering a single electron that is not part of the ensemble discussed up to this point inserted into the system. Assuming a rigidly rotating electron background, the electric field created by the electrons is given by 1.3. Then, the equation of motion for the inserted electron can be solved as shown in [7], leading to spiral-shaped trajectories for various starting conditions as shown in figure 1.3. If the angular velocity of the electron is chosen to be ω_+ or ω_-, a circular trajectory is obtained, so the single electron is performing rigid rotation with the other electrons responsible for the electric field. Arguably, such a state is supposed to be stable in time. If electrons are inserted that perform other spiral rotations, feedback effects of these electrons onto the rigid ensemble might lead to instabilities - in particular, a rotation state with the angular frequency $\omega \neq \omega_\pm$ is probably unstable.

In order to simplify equation (1.4), we define:

$$\boxed{\kappa_r = \frac{2\omega_p^2}{\Omega^2} \leq 1} \tag{1.5}$$

As we are interested in real solutions of equation (1.4), the fraction in the root needs to be smaller or equal to one. Furthermore, the value of κ_r in equation 1.5 can be written in terms of the enclosed electron density, by inserting the definitions of ω_p and Ω:

$$\kappa_r = \frac{2\omega_p^2}{\Omega^2} = \frac{2e^2 n}{\epsilon_0 m} \frac{m}{eB} = \frac{2e}{\epsilon_0 B} n \tag{1.6}$$

So κ_r depends only on the density, if the magnetic field is kept constant. κ_r therefore cannot be negative, as none[1] of the constants and parameters can be negative. Hence, equation (1.6) can be

[1] Nevertheless, the magnitude B will always be positive, regardless of the direction of the magnetic field.

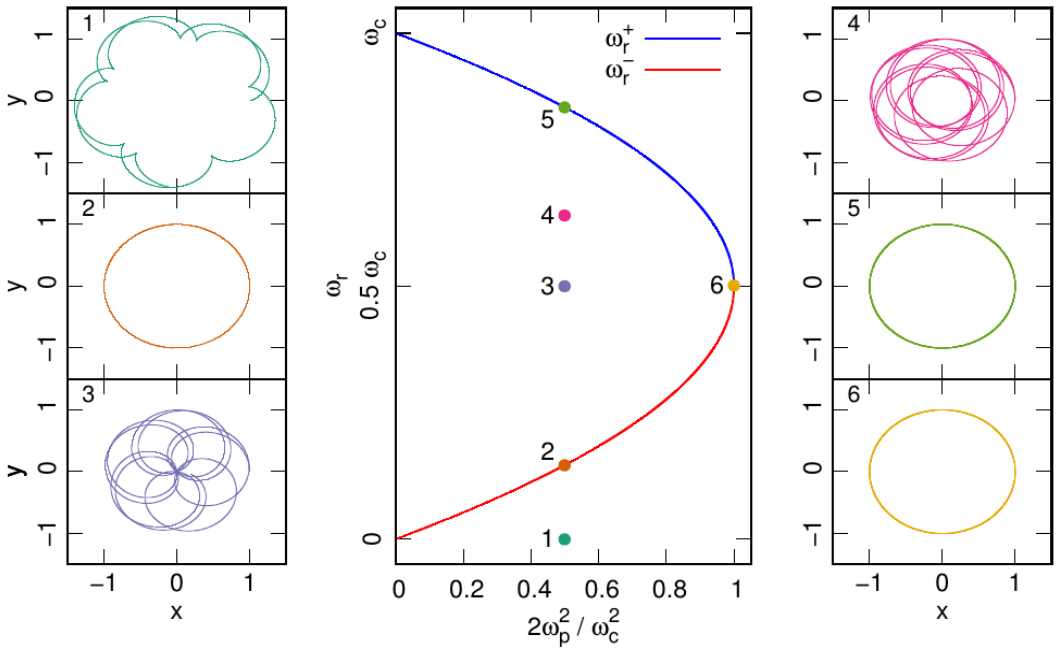

Figure 1.3: Centre: Frequencies with respect to trapping efficiency. Note that with respect to κ_r either two, one or no valid solutions are allowed for the rotation frequencies. Left and right: Illustration of the oscillations depending on the plasma parameters and the initial condition of the angular velocity of the test electron. Depending on the value of ω_p and $\omega_c = \Omega$, various rotation modes are possible. If ω is chosen as $\omega_\pm$, rigid rotation is observed as in the states 2, 5 and 6 and circular trajectories are obtained. Otherwise, the trajectories are shaped like cycloids. Taken from [7].

interpreted as a mapping of the possibly achievable density values under the assumptions in this derivation on an interval between 0 and 1. Therefore, κ_r is called **trapping efficiency** in radial direction corresponding to [5]. This parameter has been chosen in exactly this way because the condition of $\kappa_r = 1$ represents the Brilouin flow limit of the system. We solve equation (1.4) for κ_r and obtain the vertex form of a quadratic equation:

$$\omega_\pm = \frac{\Omega}{2}\left(1 \pm \sqrt{1-\kappa_r}\right)$$
$$\frac{2\omega_\pm}{\Omega} - 1 = \pm\sqrt{1-\kappa_r}$$
$$\kappa_r = 1 - \left(\frac{2\omega_\pm}{\Omega} - 1\right)^2 \tag{1.7}$$

This function is illustrated in figure 1.3. The state of the system is given by the trapping efficiency. With respect to the trapping efficiency, equation (1.7) has either two, or exactly one solution, as $\kappa_r > 1$ is forbidden by the Brilouin flow limit. If κ_r is varied between 0 and 1, the system undergoes a bifurcation, as the number of solutions changes with κ_r. These solutions all correspond to rigid rotations of the plasma column, i.e. the electrons are confined on circular orbits. Nevertheless, a plasma may perform a non-rigid rotation, so the state of the plasma is not described by equation (1.7), depending on the starting conditions of the electrons. Figure 1.3 furthermore illustrates the trajectories of a sample electron in a symmetric electric and homogeneous magnetic field in the form of:

$$E_r \propto r \qquad B_z = \text{const.}$$

Hence, only the starting conditions that correspond to 2, 5 and 6 are solutions that are true for **all** electrons in an ensemble that forms the plasma and the resulting radial electric field. In this case, the derivation of the trajectories is in analogy to the derivation presented here. In order to

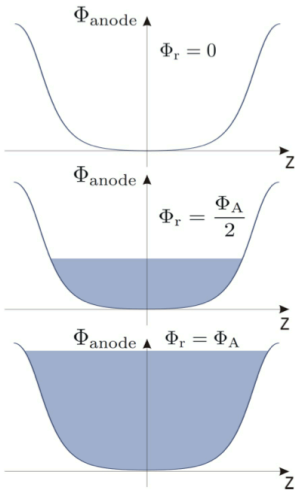

Figure 1.4: The axial potential. The captured electrons fill the potential until fast electrons are able to escape the potential well. The potential of the electrons is denoted by Φ_r. Image taken from [4].

observe solutions 1, 3, and 4, an electron background that is rotating homogeneously (comparable to solution 2, 5 or 6) has to be **assumed**. In this case, the observed electron is the only one with a different starting condition, while all other electrons have to perform a rigid rotation. Optimal electron confinement is achieved, if the lens operates at the parameters corresponding to the apex of the parabola from figure 1.3, as the apex corresponds to $\kappa_r = 1$ which represents the theoretical maximal density that can be enclosed by a homogeneous magnetic field. So, the apex is given by:

$$\begin{aligned} \kappa = \frac{2\omega_p^2}{\Omega^2} &= 1 \\ 2\omega_p^2 &= \Omega^2 \\ 2\frac{e^2 n}{\epsilon_0 m} &= \frac{e^2 B^2}{m_e^2} \end{aligned}$$

This leads to an expression of the highest electron density that can be confined radially by a Gabor lens.

$$\boxed{n = \frac{B^2 \epsilon_0}{2m}} \tag{1.8}$$

Longitudinal Confinement

The longitudinal confinement of electrons in a Gabor lens is achieved using an electrode system, creating an electric potential that applies an inward force on the electrons that are about to escape the Gabor lens in longitudinal direction. In most applications, three cylindrical electrodes are used. Two electrodes on ground potential are located on either side of the lens. A third electrode in the centre of the lens is put on positive potential [5].

In order to calculate the maximal density of electrons that can be captured in this potential, it is necessary to estimate the potential of the electrons. As the number of confined electrons increases, their space charge reduces the positive potential, compare figure 1.4. If the anode potential is decreased fully, the enclosed electrons are no longer confined.

In these calculations, we assume that the longitudinal boundary condition is independent of the electron temperature [5]. The potential of the enclosed electron cloud can be derived by solving the Poisson equation in cylindrical coordinates. Here we assume a cylindrical homogeneous

electron cloud with constant density.

$$\Delta\Phi = -\frac{\varrho(r)}{\epsilon_0}$$

$$\frac{1}{\rho}\frac{\partial}{\partial\rho}\left(\rho\frac{\partial\Phi}{\partial\rho}\right) + \frac{1}{\rho^2}\frac{\partial^2\Phi}{\partial\phi^2}^{0} + \frac{\partial^2\Phi}{\partial z^2}^{0} = -\frac{en}{\epsilon_0}$$

$$\frac{1}{\rho}\left(\frac{\partial\Phi}{\partial\rho}\frac{\partial}{\partial\rho}\rho^{1} + \rho\frac{\partial}{\partial\rho}\frac{\partial\Phi}{\partial\rho}\right) = -\frac{en}{\epsilon_0}$$

$$\frac{1}{\rho}\frac{\partial\Phi_\rho}{\partial\rho} + \frac{\partial^2\Phi_\rho}{\partial\rho^2} = -\frac{en}{\epsilon_0}$$

Considering the fact that this equation can be solved by using the ansatz $\phi(r) = \alpha r^2 + c$.

$$-\frac{1}{\rho}2\alpha\rho - 2\alpha = \frac{en}{\epsilon_0}$$

$$\alpha = -\frac{en}{4\epsilon_0}$$

We find the potential:

$$\rightarrow \Phi_\rho = -\frac{en}{4\epsilon_0}\rho^2 + c \tag{1.9}$$

By solving for the density and assuming a constant radius that is equal to the radius of the anode R_A this resolves to:

$$\boxed{n(\Phi_r) = \frac{4\epsilon_0}{eR_A^2}\Phi_r} \tag{1.10}$$

Alternatively, the electric field can be integrated in radial direction as shown in [4]. The electric field can be found by using the Gaussian theorem.

$$\Phi_r = -\int_0^{R_A} E(r)dr$$

$$\Phi_r = \frac{neR_A^2}{4\epsilon_0} + c$$

As the Maxwell equations have gauge symmetry, the electric field is invariant if the potential is transformed by an arbitrary scalar field $\chi(\mathbf{r}, t)$ in the following way:

$$\Phi \rightarrow \Phi' = \Phi - \frac{\partial}{\partial t}\chi$$

Therefore, the integration constant may be chosen as $c = 0$, which leads to equation (1.10).

The linear dependency between density and potential can be verified by measurements, see [8]. In general, the Gabor lens potential will not be filled completely with electrons, so there is a remaining potential depression. Therefore, the trapping efficiency in longitudinal direction is introduced in conjunction to the trapping efficiency in radial direction [5]:

$$\boxed{\kappa_l = \frac{\Phi_r}{\Phi_A}} \tag{1.11}$$

From measurements and observation it is known that the volume the plasma is trapped in is limited not by the radius of the anode, but the radius of the ground electrode. Therefore, equation (1.10) needs to be modified.

Improved calculation of the longitudinal confinement

Previously, it was assumed that the anode potential is completely filled with electrons, such that $\Phi_A = \Phi_r$. Due to loss mechanisms, this is not necessarily fulfilled [4], [5]. So the previous calculation is repeated, assuming a plasma radius R_p that is smaller than the radius of the anode. Then, the potential inside the electron cloud in the case of $r < R_p$ is obtained using the Gaussian theorem and assuming that $\Phi_r < \Phi_A$:

$$\Phi_{\text{in}} = \frac{ne}{4\epsilon_0} r^2 + C_1$$

The potential outside the electron cloud can be calculated analogously:

$$\Phi_{\text{out}} = \frac{neR_p^2}{2\epsilon_0} \ln(r) + C_2$$

In order to determine the resulting constants, we use the condition that $\Phi(R_A) = \Phi_A$. Using this condition we find C_2:

$$\Phi(R_A)_{\text{out}} = \Phi_A = \frac{neR_p^2}{2\epsilon_0} \ln(R_A) + C2$$

Solving for C_2:

$$\underline{C_2 = \Phi_A - \frac{neR_p^2}{2\epsilon_0} \ln(R_A)}$$

From here, C_1 can be calculated by inserting C_2 and using the continuity condition $\Phi_{\text{in}}(R_p) = \Phi_{\text{out}}(R_p)$:

$$\begin{aligned}
\Phi_{\text{in}}(R_p) &= \Phi_{\text{out}}(R_p) \\
\frac{ne}{4\epsilon_0} R_p^2 + C_1 &= \frac{neR_p^2}{2\epsilon_0} \ln(R_p) + C_2 \\
\frac{ne}{4\epsilon_0} R_p^2 + C_1 &= \frac{neR_p^2}{2\epsilon_0} \ln(R_p) + \Phi_A - \frac{neR_p^2}{2\epsilon_0} \ln(R_A) \\
\frac{ne}{4\epsilon_0} R_p^2 + C_1 &= \Phi_A - \frac{neR_p^2}{2\epsilon_0} \ln\left(\frac{R_A}{R_p}\right)
\end{aligned}$$

So we find C_1:

$$\underline{C_1 = \Phi_A - \frac{neR_p^2}{2\epsilon_0} \ln\left(\frac{R_A}{R_p}\right) - \frac{ne}{4\epsilon_0} R_p^2}$$

As a result, we find the equations for the potential in their final form:

$$\begin{aligned}
\Phi_{\text{in}}(r) &= \frac{ne}{4\epsilon_0} r^2 + \Phi_A - \frac{neR_p^2}{2\epsilon_0} \ln\left(\frac{R_A}{R_p}\right) - \frac{ne}{4\epsilon_0} R_p^2 \\
\Phi_{\text{out}}(r) &= \frac{neR_p^2}{2\epsilon_0} \ln(r) + \Phi_A - \frac{neR_p^2}{2\epsilon_0} \ln(R_A)
\end{aligned}$$

After simplification the set of equations describes the potential distribution, which is visualized in figure 1.5.

$$\Phi_{\text{in}}(r) = \Phi_A - \frac{neR_p^2}{2\epsilon_0} \ln\left(\frac{R_A}{R_p}\right) - \frac{ne}{4\epsilon_0}(R_p^2 - r^2) \tag{1.12}$$

$$\Phi_{\text{out}}(r) = \Phi_A - \frac{neR_p^2}{2\epsilon_0} \ln\left(\frac{R_A}{r}\right) \tag{1.13}$$

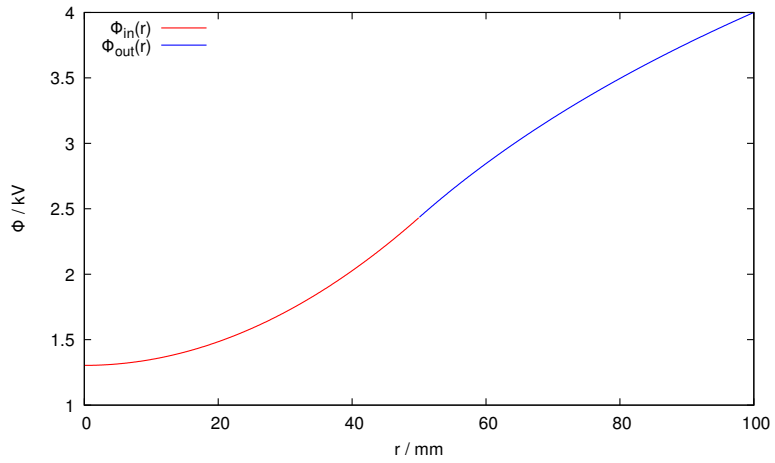

Figure 1.5: Theoretical potential distribution in the Gabor lens. Here, the plasma streches only to R_p, while there are no charge carriers between R_p and R_A. In order to see the effect of the smaller electron column, $R_p = {}^1/_2 R_A$ has been chosen.

Considering Φ_{in} at the edge of the plasma cloud at R_p, we can derive an equation for the charge carrier density:

$$\Phi_{\text{in}}(R_p) = \Phi_A - \frac{neR_p^2}{2\epsilon_0} \ln\left(\frac{R_A}{R_p}\right)$$

Under the assumption that $\Phi_{\text{in}}(R_p) = \Phi_\rho = \frac{neR_p^2}{4\epsilon_0}$, which is the result obtained in equation (1.9), we find:

$$\frac{neR_p^2}{4\epsilon_0} = \Phi_A - \frac{neR_p^2}{2\epsilon_0} \ln\left(\frac{R_A}{R_p}\right)$$

$$\Phi_A = \frac{neR_p^2}{4\epsilon_0}\left(1 + 2\ln\left(\frac{R_A}{R_p}\right)\right)$$

$$\boxed{n = \frac{2\epsilon_0 \Phi_A}{eR_p^2\left(1 + 2\ln\left(\frac{R_A}{R_p}\right)\right)}}$$

1.2.3 Operation function of a space charge lens

As observed in the previous sections, the confinement and therefore the confined electron density is dependent on the spatial direction. Confinement in axial direction depends on the electric potential only, while the magnetic field is used to prevent electrons from escaping transversally.

As the maximum densities that can be confined with respect to the magnetic field and the potential, we can equal both densities and find a relation between the potential and the magnetic field. If potential and magnetic field satisfy this relation, the densities confined are equal. As this state is believed to be stable, the aforementioned relation is called operation function, compare [4]:

$$\Phi_A = \frac{eR_p^2}{8m_e}\left(1 + 2\ln\left(\frac{R_A}{R_p}\right)\right) B_z^2 \tag{1.14}$$

Here, R_A is the radius of the anode, R_p the maximal radius of the plasma cloud. Experiments show that the maximal radius is generally the radius of the ground electrode. The operation function can be simplified by assuming that $R_p = R_A$:

$$\Phi_A = \frac{eR_A^2}{8m_e} B_z^2 \tag{1.15}$$

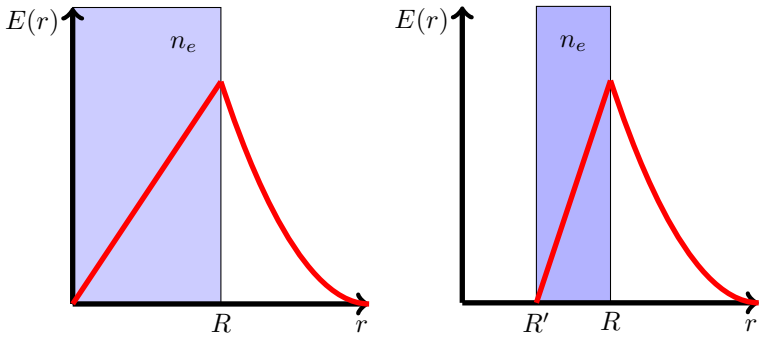

Figure 1.6: Sketch of the radial electric field of two electron distributions. Left: Homogeneous and focussing distribution. Right: Torus distribution. A torus dustribution focusses only at radii between R' and R, leading to disturbances in the phase space distribution of an ion beam.

The operation function provides the user of a Gabor lens with guidance in choosing the experimental parameters. Using a Gabor lens requires the choice of two primary parameters in terms of electron confinement: the potential of the anode and the current in the coils, effectively the magnetic field. By using the operation function, these two parameters are linked and the choice of parameters becomes one-dimensional. It has been shown that plasma instabilities can arise if the operation function is not applied [9]. In addition, the occurrence of instabilities depends on the pressure [10]. In addition, plasma instabilities result in increased emittance growth if an ion beam is supposed to be focussed by the Gabor lens [4].

1.2.4 Electron production and losses

Electrons in the Gabor lens are produced mostly by residual gas ionization [11]. With finite probability, there is a free electron inside the lens volume that is accelerated by the fields and ionizes residual gas molecules. The resulting electrons will cause further ionization of the residual gas, as they are accelerated by the potential of the anode as well, while the ions are emitted by the Gabor lens. As mentioned in [11], there has to be a second process generating electrons next to the residual gas ionization. For instance, secondary electrons can be created by ion or electron impact on surfaces. Hereby, a few free electrons are created per lost electron that posses a relatively small energy of several eV, compare [12]. If the secondary electrons are created on grounded surfaces, they are accelerated away from the surface by the anode potential and can support electron generation by residual gas ionization in a Gabor lens.

Electrons gyrate around magnetic field lines. Therefore, they follow the field lines until they are repelled or until the electrons impact on the lens chamber walls. In the latter case, secondary electrons are generated. These electrons have a very low kinetic energy with respect to the electron that got lost on the wall previously, compare [12]. So in most cases, the secondary electrons are not able to leave the surface they emerged from.

Measurements show that the losses are independent of the magnetic field. Furthermore, the emitted x-rays indicate that most losses are on the anode [11].

1.2.5 Electron density

While performing theoretical calculations with a Gabor lens, a homogeneous electron density in cylindrical form is often assumed, as the geometry of the experiment often resembles a cylindrical symmetry as well. Simulations show that the electrons are distributed via the Boltzmann distribution, compare [4], figure 4.5 and [6], if a finite temperature is allowed.

$$n_e(r) = n_0 e^{-\frac{e\Phi(r,n_e(r))}{kT}} \tag{1.16}$$

This distribution strongly depends on the temperature T. In the limit of $T \to 0$, a homogeneous density distribution that drops to zero at the plasma edge is obtained. At finite temperatures there is a sigmoidal transition in the density at the plasma edge, compare figure 2.27 in [4]. It is highly non-trivial to find the density distribution function, as the potential $\Phi(r)$ depends on

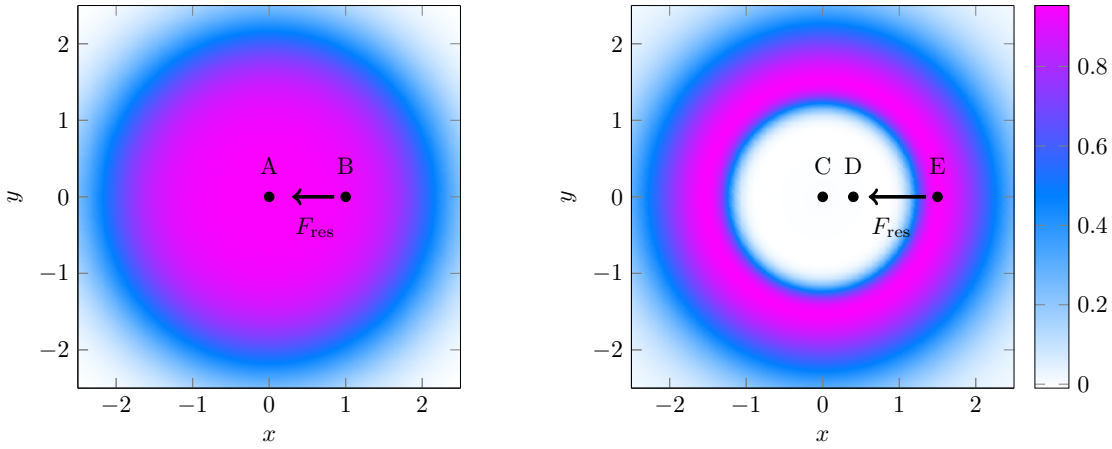

(a) Nearly homogeneous electron density distribution.

(b) Hollow electron density distribution.

Figure 1.7: Sketch of two possible electron density distributions. The density is encoded in colour shading. An ion at A will not be affected by a force by the space charge of the electron in this plane due to symmetry. An ion at B will be affected by a resulting force pointing inwards. (b): A hollow distribution may lead to a Diochrotron instability. Here, an ion at C or D will not encounter a force by the space charge of the electron in this plane due to symmetry. Nevertheless, an ion at E will be affected by a resulting force pointing inwards.

the local density as well, see [6], so equation (1.16) is recursive. In the theoretical description of the Gabor lens, the density at small radii is almost constant and forms a plateau. So for small radii, the approximation of a cylindrical homogeneous electron cloud is feasible.

1.2.6 Focusing of an ion beam by a space charge lens

The focussing principles of a space charge lens can be discussed assuming a homogeneous and constant electron density distribution, compare figure 1.7a and 1.6. Note that only positive ions can be focussed using a Gabor lens that confines electrons, compare [13]. Let a single ion be positioned perfectly on the symmetry axis at position A. In this case, the ion will see the same amount of space charge in all directions. Therefore, it's trajectory will not be influenced by the space charge of the Gabor lens. If an ion is off-axis, for instance at position B, this symmetry is broken. It will see more charge in the direction of the symmetry axis than in any other direction. The resulting force will guide the ion towards the centre. Therefore, a Gabor lens with a homogeneous or nearly homogeneous electron density distribution focusses an ion beam in radial symmetry.

If the shape of the density distribution is similar to a torus, the Gabor lens will not focus an ion beam linearly. Consider figure 1.7b. Again, an ion at position C or D will not be influenced by the space charge due to symmetry. Nevertheless, an ion at position E will encounter an attractive force from the electrons in the torus at smaller radii. Therefore, the ion at E will be accelerated inwards. Here, the Gabor lens is focussing only the outer parts of an ion beam. This leads to aberrations in phase space and an increase in the emittance of the ion beam. Therefore, this configuration is not useful for focussing. This effect has been measured and is discussed in [4].

1.2.7 Electron drifts

Lorentz force

The electrons confined in a Gabor lens are subjected to several drifts that can be derived in plasma physics. A simple effect involving a magnetic field on charged particles is described by the Lorentz force. In a homogeneous magnetic field, charged particles that have a velocity component perpendicular to the magnetic field are forced on to circular orbits by the Lorentz

force. If the particles have a non-vanishing velocity component parallel to the magnetic field, the resulting trajectory is a spiral. The radius of the circular orbit is called Lamor radius or gyroradius, compare [14], and can be calculated in the following way:

$$r_l = \frac{m}{q}\frac{v}{B} = \frac{\sqrt{2m}}{qB}\sqrt{E} \tag{1.17}$$

If we intend to leave B constant and under the assumption of a non-relativistic regime, we can only adjust the electron energy in order to increase or decrease the Lamor radius. In general, the Lamor radius should be smaller than the radius of the inner structure of the Gabor lens. This condition imposes a theoretical limit on the energy of the electrons inserted by the electron source. Nevertheless, the effect of the other drifts and the electric field is neglected. Furthermore, the magnetic field in the experiment will not be perfectly homogeneous. Therefore, this limit may not relevant in a future experiment.

ExB-Drift

As an electric field is present along with the magnetic field, the $E \times B$ drift, compare [14], has to be considered:

$$\mathbf{v}_{\mathrm{ExB}} = \frac{\mathbf{E} \times \mathbf{B}}{B^2}$$

Here, the drift velocity is perpendicular to the electric and magnetic field and furthermore, it is independent of charge or energy. The only parameters that influence this velocity directly are the fields themselves. In the field configuration of a Gabor lens, the $E \times B$ drift corresponds to a rotation in the xy-plane which can be interpreted as an azimuthal drift in cylinder coordinates. Hence, the $E \times B$ drift velocity does not influence the confinement efficiency directly. Note that a standard right handed Cartesian coordinate system is used. The $E \times B$ drift will be a mathematically positive rotation around the z-axis, as the electric field points radially outwards.

Gradient B drift

The coils that are used to generate the magnetic field of the Gabor lens available at IAP are not in Helmholtz configuration. They have been moved apart, causing a gradient in the magnetic field illustrated in figure 2.10. The gradient in the magnetic field causes a drift corresponding to:

$$v_d = \frac{m v_\perp^2}{2qB^3}\mathbf{B} \times \nabla\mathbf{B} \tag{1.18}$$

A proper derivation of this expression can be found in [14]. Checking the geometry, both $E \times B$ and gradient B drift point in the same direction for electrons.

Diffusion

Diffusion across magnetic field lines is another possibility for electrons to move in a confining magnetic field. Details on the diffusion processes can be found in [5]. The total transversal loss current is modelled as a sum of currents. First, the loss current that arises when the transversal confinement capacity is exceeded has to be considered. Furthermore, a charge density gradient due to losses at the surface of the electron plasma can lead to a radial drift movement as the remaining electrons try to reduce the gradient. In addition, coulomb interactions between electrons performing $E \times B$ drift and the background electron field create an energy exchange with the remaining electrons, resulting in an increase in mean orbit of the $E \times B$ drifting electron. This drift is proportional to ω_- and κ_r.

1.2.8 Density measurement

The density of the electrons captured in a Gabor lens cannot be measured directly, but it is possible to estimate a mean density and get an impression of the density distribution. In order to find the mean density, it is necessary to measure the energy of the ions that are emitted by the Gabor

lens longitudinally by an impulse spectrometer. Ions are supplied via residual gas ionization. While the electrons are confined, the ions are accelerated by the potential longitudinally out of the lens volume. By measuring the maximal energy, the potential depression due to the space charge of the electrons is measured. The space charge of the electrons can easily be connected to a mean electron density, see [8], [10] and the derivation of the longitudinal confinement in section 1.2.2. Therefore, the potential in equation (1.10) can be substituted by the potential depression due to the electron cloud, which yields the mean density in the Gabor lens:

$$n_e = \frac{4\epsilon_0 \Delta\Phi}{eR_A^2}$$

Here, $\Delta\Phi$ is the potential depression, corresponding to the difference between the maximum energy of the emitted ions and the anode potential. Furthermore, we can observe the light emitted by the residual gas.

The residual gas atoms are excited by collisions with the electrons or ions and emit a characteristic light spectrum. The intensity of the light can be measured spatially using a CCD camera that is observing the lens volume longitudinally, compare figure 3.12. Unfortunately, the light intensity depends on electron density and electron energy, because the cross-section for a residual gas excitation depends strongly on the energy. Therefore, a bright spot on the CCD image corresponds to an area with large electron density **or** it indicates an area of certain electron energy, so that the cross-section for residual gas excitation is very large **or** we observe a mixture of both effects. Using both the CCD image and the mean density measurement, it is possible to obtain a qualitatively good idea of the density distribution in a Gabor lens.

The electrons can only gain energy via the electric field. If the electrons are inserted by an electron source, the initial energy is known as well. Therefore, regions in the Gabor lens with energies that correspond to the high cross-sections could be identified and the CCD image could be rescaled according to this effect, so that the real density distribution can be measured via the CCD camera and the impulse spectrometer. This should be subject to further investigations, which are not in the scope of this thesis.

1.2.9 Residual gas pressure

The previous calculations assumed a situation with perfect vacuum. However, experiments have shown that it is possible to find an optimal pressure for all settings of magnetic field and potential that maximises the confined electron density while other pressure values lead to small densities or instabilities [8] and that the properties in general depend on the residual gas pressure [4]. So it is possible to see a very good electron distribution that is changing into a Diocotron instability only by increasing the pressure.

1.2.10 Ignition

The process that leads to a filling of the Gabor lens is called ignition, although it is not comparable to the situation is gas discharges. Here, it is assumed that a free electron exists in the plasma volume. Due to the electric field, it is accelerated until it most likely will ionize a residual gas atom, thereby supplying a further electron. This leads to a cascade which is balanced by electron losses due to the confinement limit. In an experiment, ignition can be detected by measuring the emitted light by the plasma or by observing the current of the anode power supply. The anode current is very low if the plasma is not yet ignited. Upon ignition, the resistance between the anode and ground decreases, as the plasma causes loss electrons to travel towards the anode and positively charged ions to travel longitudinally towards grounded surfaces. Both effects contribute to the anode current. If the anode current shows a step-like increase as a result of a variation of potential, magnetic field or pressure, ignition is achieved.

1.3 Concepts of electron emitters

There are several concepts of electron emitters in existence. One proven concept is to use a hot filament. In this case, due to thermionic emission, free electrons are able to leave the solid and are available for further use. The disadvantage of these so called hot emitters is that the hot

filament is prone to ageing and thus the electron emitter has to complete rather short service cycles.

Electrons that are emitted by a cathode are typically accelerated using an electric field between cathode and an anode. If the cathode and anode are both plates, the emission can be described by the Child Langmuir law, compare [15]:

$$I = PV^{\frac{3}{2}}$$

Here, I is the current extracted from the electron source, V the potential used for extraction and P is called perveance, a constant that depends on the geometry of an electron source only.

Electrons emitted by the cathode of an electron source reduce the potential at the cathode. If the potential depression is not large enough to reduce the potential to zero, the current emitted by the cathode is limited by the rate electrons are supplied by the heating of the cathode. Here, we speak of *thermionic emission*. Increasing the heating will also increase the electrons available for extraction, thus increasing the potential depression. If the potential at the cathode reaches zero, electrons are no longer accelerated towards the anode, so the current that can be extracted is limited. This is the *space charge limited operation*, compare [15]. In thermal electron sources, the electrons are supplied by a heated filament.

Electrons are able to leave conductors at any temperature below 0 K. Increasing the temperature of the conductor also leads to an increased amount of electrons available for extraction. The velocities of the electrons in the conduction band are distributed stochastically, therefore, few electrons have a very large velocity and thus a large energy compared to the other electrons. Few electrons are therefore able to leave the solid. Increasing the energy by heating the filament leads to a larger amount of electrons that are able to leave the solid.

Alternatively, electrons can be provided by field emission. High electric fields at surfaces are able to extract electrons, because they supply the energy necessary to leave the lattice in the solid. As electric fields are much stronger at small tips, such a configuration can be used to create sources for free electrons. Conventionally, small tips are created by etching and can be produced with a thickness of several atom layers. A different approach that emerged with increasing expertise in nanotechnology is to use carbon nano tubes (CNT) grown on a substrate in channels of alumina, offering a very small tip and a very long shaft. As the multiplier for the electric field depends on the length of the shaft and the size of the tip itself, CNT-based electron emitters promise a very good performance [16].

Chapter 2

Simulations

2.1 Configurations

In order to organise the results of the simulations and the different geometries, four configurations are defined. Some share similarities, such as the cusp and Gabor cusp, but all configurations represent a different approach of introducing an electron source to the Gabor lens system. The configurations to study the electron injection are:

Auxiliary coil
The first attempt to insert electrons into a Gabor lens is using a small auxiliary coil to create a depression in the magnetic field in the central section of the lens. Electrons could then be inserted transversally into the lens. The auxiliary coil has been investigated with and without an additional μ-metal shield. μ-metal is a general term for an alloy of iron and nickel that can, depending on the composition, show varying permeability. Therefore a vast amount of materials can serve as magnetic shielding for the electron emitters.

Cusp structure
Here, the magnetic confinement is abrogated in the centre by reversing the polarity of one of the Helmholtz coils. This leads to a cusp shaped magnetic field. In the central section of the lens, the magnetic field lines will point in radial direction, effectively breaking the confinement. Here, electrons will be able to be inserted radially but they are not magnetically confined. Therefore, large currents are necessary to achieve a decent electron density (see figure 2.20) and thus a sufficient focusing performance. On the other hand, the electron distribution in the lens is mostly on the symmetry axis which is the desired distribution.

Gabor cusp structure
Gabor himself proposed in [1] a cusp configuration by placing an electron emitting ring in a cusp-shaped magnetic field. The electrons are supposed to travel to another area where the actual plasma is confined by a second solenoid. The setup can be realized with almost any given Gabor lens by adding the electron sources and a coil creating the cusp with respect to the magnetic confinement already in place.

Internal source
Another concept to insert electrons in the Gabor lens is placing the electron source inside the lens. Therefore the electrons do not have to travel past the anode which led to many losses in the auxiliary coil setup. In order to shield the source from the magnetic field, a μ-metal shield is applied around the electron emitter. This shield attenuates the magnetic field locally without breaking the symmetry like the auxiliary coil does.

In figure 2.1, we see an attenuation of the magnetic field by the μ-metal of about 97.27 %. The attenuation factor is calculated in the following way:

$$a = \frac{B_{\text{out}} - B_{\text{min}}}{B_{\text{out}}}$$

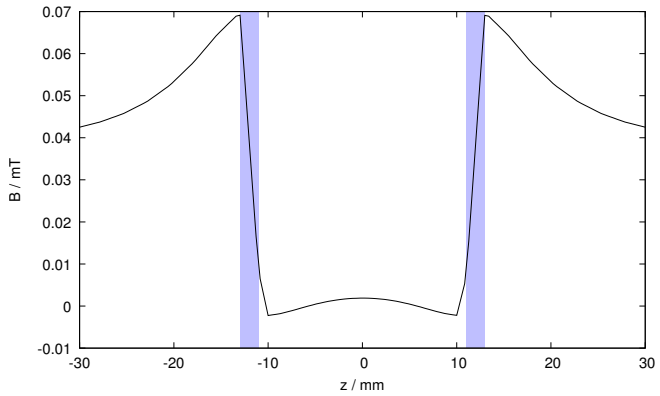

Figure 2.1: Depression effect of the μ-metal shielding. The outer radius of the cylinder is 13 mm, the inner radius is 11 mm. The dimensions of the cylinder are indicated by the blue area. The centre of the cylinder is at $z = 0$.

Here, B_{out} is the magnetic field outside of the shield, B_{in} is the maximal field on the inside.

2.2 Preliminary simulations using an arbitrary structure

As a first step, simulations will investigate the possibilities of injecting electrons transversally into a Gabor lens. The first simulations will be conducted using CST Studio Suite, a commercial simulation software used for particle tracking, EM-wave simulations and other applications.

In order to understand space charge effects, a second in-house simulation software, bender [17], is used in a second stage. Bender is a particle-in-cell code with advanced features, such as residual gas ionization, space charge effects, various solvers and mover algorithms and many possibilities to configure the output of the simulation.

An arbitrary structure was used for the first simulations in order to find a general configuration that may allow a filling of the Gabor lens. Comparing figure 2.3b, the larger radius of the ground electrode compared to that of the anode is visible. This is not a typical design of the electrode system, but it was simulated in order to check for positive effects. In a first step, several configurations of electron emitters have been tested and are evaluated.

2.2.1 Electric and magnetic properties

The potential and the electric and magnetic fields are shown in figures 2.2a, 2.2b and 2.3a. If the electron source is grounded, the electrons will not be confined by the anode potential, since their energy is larger than the confining potential. Therefore, the source should be put on a positive potential with respect to ground. This is supposed to reduce the potential difference between anode and electron source. Other than that, it might be a possible alternative to put the anode and the source on ground potential and provide the longitudinal confinement by applying a negative voltage on the former ground electrodes. Considering the composition of the Gabor lens test stand, it is troublesome to reverse the polarity of the high-voltage confinement in a way described above, as at least one ground electrode is flange-mounted to the vacuum vessel. Furthermore, this potential distribution prevents the emission of residual gas ions out of the Gabor lens. Since the ions are used for diagnostics, choosing the potential distribution in the aforementioned way is not useful. Therefore, it was decided to put the electron source and the adjacent power supplies on a high-voltage terminal that may be connected directly to the anode power supply.

2.2.2 Comparison of μ-metal shield and auxiliary coil

When utilizing a μ-metal shield in order to attenuate the magnetic field close to the electron source, some electrons that are repelled by the magnetic field can be observed moving backwards to the source. They are absorbed by either the shield or the emitting surface, compare figure 2.4,

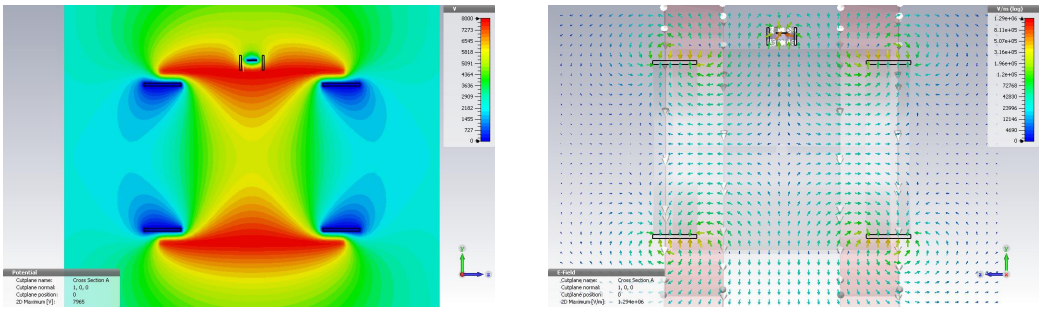

(a) Potential (b) Electric field

Figure 2.2: Electric potential and electric field of the electrodes in the yz-plane. Here we see the electron source inside the auxiliary coil on ground potential, disturbing the local potential distribution.

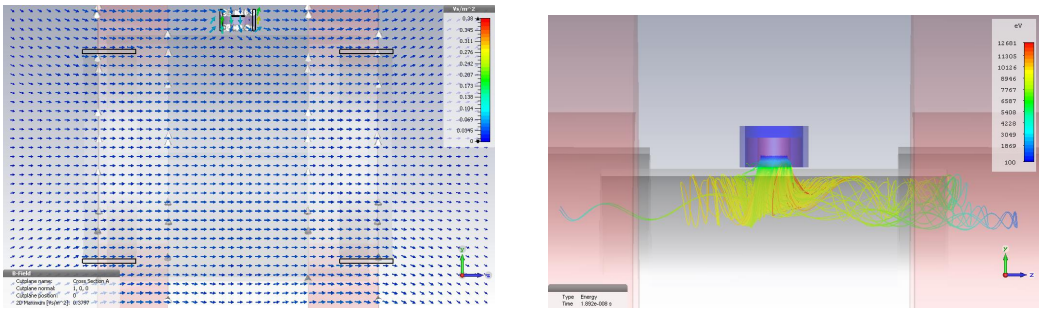

(a) Magentic field (b) Electron trajectories

Figure 2.3: Particle flow using a shielded auxiliary coil. Here, most of the electrons get lost on the anode. Secondary electrons will probably be absorbed by the anode rapidly, as their energy is not large enough to escape several kV potential, compare [12]. No electron escaped through the Helmholtz coils. $I_{\mathrm{HC}} = 20\,\mathrm{A}$, 300 windings each, $B_{\max} = 17.37\,\mathrm{mT}$; $I_{\mathrm{aux}} = 100\,\mathrm{A}$ at 20 windings, $B_{\mathrm{aux}} = 70.87\,\mathrm{mT}$. The potential is $\Phi = 10\,\mathrm{kV}$ and the initial electron energy is $100\,\mathrm{eV}$.

top. Furthermore, an auxiliary coil could be used to perturb the magnetic field locally, compare figure 2.3a. As a result, the electrons may be able to enter the inner region of the Gabor lens. The simulations reveal that the electrons move only in one direction, e.g towards the positive or negative z-axis, because the magnetic field lines are turbulent in the opposite direction. This may lead to an asymmetric electron column in the Gabor lens. Comparing these simulations, the μ-metal shield seems to be the superior method, but the coil could nevertheless be an important asset in the experiments. Introducing the anode and electrode system we observe a problem: due to the large potential on the anode, the electrons are attracted by and lost on the inner anode surface, compare figure 2.3b.

2.2.3 Multiple tests with the correct anode setup and nearly homogeneous magnetic field

In the following simulations, the anode system has been changed in order to fit the system already installed in an experiment test stand at the IAP. Afterwards, different geometries have been tested simultaneously in order to optimize the extraction of electrons out of the electron source. First and foremost, an electron source with μ-metal shield has been placed outside the anode. An auxiliary coil is used to match the electron beam through the gap in the anode. Additionally, two sources have been placed inside the anode volume: one is located at the radius of the ground electrode, the other one is located at a slightly smaller radius, both are not shielded. All sources are on ground potential. Trajectories of the electrons emitted by these sources are shown in figure 2.5a. To check for the effect of a homogeneous field on the electron source performance, the Helmholtz coils have been chosen with a larger radius.

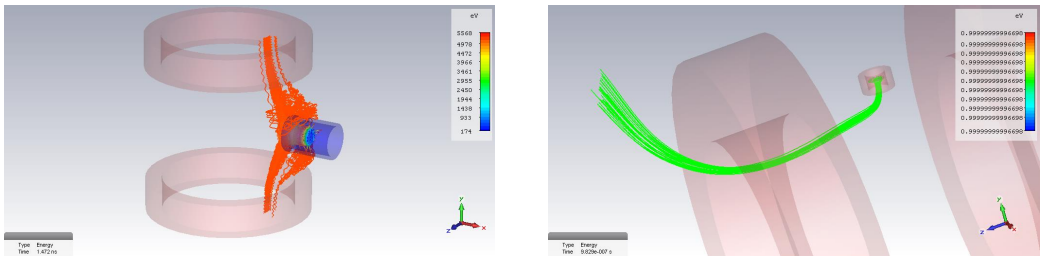

(a) Shielded electron source (b) Auxiliary coil

Figure 2.4: Using a shielded source, the electrons that are able to exit the source structure move through both solenoids. Due to turbulences in the magnetic field created by the auxiliary coil, the electrons can only escape in one direction of the lens. By changing the current direction in the auxiliary coil, the electrons will escape through the solenoid in negative z-direction.

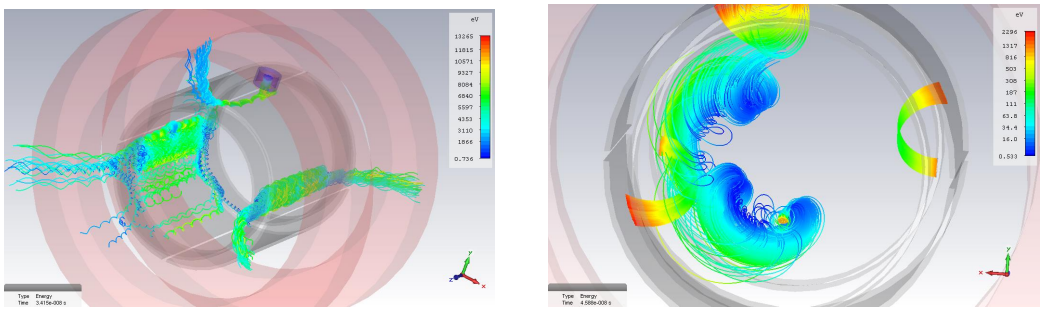

(a) Three different source configurations, $\Phi_{\text{in,source}} = 0\,\text{V}$ (b) Low energy electron beam, $\Phi_{\text{in,source}} = 7.9\,\text{kV}$.

Figure 2.5: Impact of the electron energy on the electron trajectories. $I_{\text{HC}} = 3\,\text{A}$, 300 windings each, $B_{\text{max}} = 2.7\,\text{mT}$; $I_{\text{aux}} = 20\,\text{A}$ at 100 windings, $B_{\text{aux}} = 70.87\,\text{mT}$. The potential is $\Phi = 8\,\text{kV}$ and the initial electron energy is 2 keV.

A basic problem during the simulations is that the anode potential accelerates the electrons to high energies. It is desired that enclosed electrons have a kinetic energy around 100 eV, so that the cross-section for ionization of the residual gas is maximal, compare figure 2.21. Hence, the electron sources should be put on a positive potential. The source potential should be in the same order of magnitude as the anode potential, because of the local disturbing effect on the potential close to the electron source, shown in figure 2.2a. Furthermore, the extraction energy of the electron sources should be far smaller than the anode potential, as longitudinal confinement is not given for electrons with sufficiently high energy.

2.2.4 Applying a potential on the electron sources

As mentioned before, it is not convenient to put the electron source on ground potential. In case of a source outside of the anode, the anode potential will accelerate the electrons tremendously. If the electron source is put on potential as well, the electron energy inside the Gabor lens can be controlled and smaller acceleration voltages than the anode potential can be achieved. Furthermore, it might be useful to set the electron source on a slightly smaller potential Φ_S than the anode, especially if the source is located inside the Gabor lens.

$$\Phi_S = \Phi_A - \Delta\Phi \tag{2.1}$$

As a result, the electron energy inside the lens can be reduced to several hundred eV or less. $\Delta\Phi$ corresponds to the energy which the electrons gain in addition to the extraction energy. It is now possible to observe an electron confinement with much larger gyration radii in figure 2.5b. Because the trajectories lead to the anode walls fairly quickly, a fourth source is introduced at a smaller radius in the simulations. As a result, it is more suitable, in this regime, to place the source at a small radius.

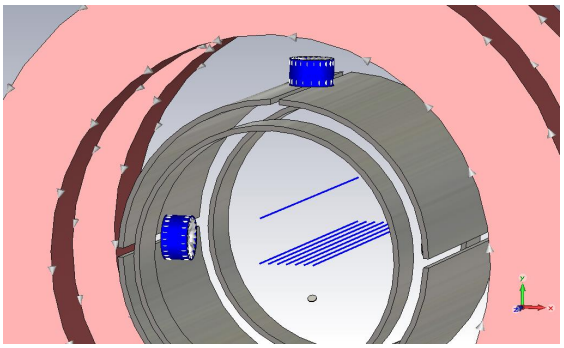

Figure 2.6: Top: Position of the internal and external auxiliary coil assisted source.

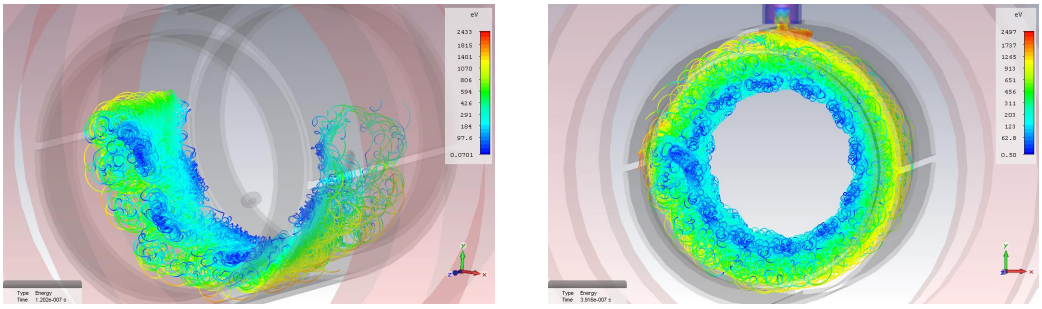

(a) Trajectories emitted by the **internal source**. (b) **Internal source** and **external source** trajectories.

Figure 2.7: Most of the electrons emitted by the external source are lost on the anode, while the internal source provides confined electrons. All sources in these figures are constructed with a μ-metal shield and an auxiliary coil. $I_{\mathrm{HC}} = 40\,\mathrm{A}$, 300 windings each, $B_{\mathrm{max}} = 34.73\,\mathrm{mT}$; $I_{\mathrm{aux}} = 20\,\mathrm{A}$ at 100 windings, $B_{\mathrm{aux}} = 70.87\,\mathrm{mT}$. The potential is $\Phi = 8\,\mathrm{kV}$ and the initial electron energy is $2\,\mathrm{keV}$.

2.2.5 Internal and external auxiliary coil assisted source

In order to increase the performance of the electron source, an auxiliary coil is implemented along with a shielding cylinder composed of μ-metal. No drift of electrons in radial direction has been observed yet, so the electron source needs to be located at the smallest radius possible. On the other hand, putting an electron source at a small radius will influence the confined plasma. Therefore, the performance of the external auxiliary coil setup is compared to an identical setup inside the anode. Simulations show that the extraction from the external source is difficult since losses occur at the anode gap. Furthermore, the internal source inserts electrons at a smaller radius.

Trajectories for the internal source are shown in figure 2.7a. An azimuthal $E \times B$ drift over 180° is observed, which is promising already. Nevertheless, there is no radial movement. Removing the other internal sources and extending the simulation runtime leads to a full 360° drift as seen in figure 2.7b.

In order to find the optimal source potential, a parameter sweep on the potential difference between the electron sources and the anode potential has been performed. As mentioned before, the sum of the potential difference and the initial energy of the electrons yields the kinetic energy that is relevant for propagation in the Gabor lens. The anode potential is $8\,\mathrm{kV}$. Very small differences in the potentials lead to relatively small penetration depths of the electrons, so they remain at large radii. If the electron energy is very large, for instance in the magnitude of the anode potential, the electrons get lost at the anode or escape the lens longitudinally and perform a very slow $E \times B$ drift. The optimal potential difference between anode and electron source is $3.2\,\mathrm{kV}$, as it is a good trade-off between increasing losses and smaller radii of electrons. Here, "optimal" denotes electrons closest to the centre. The results of the simulations are shown

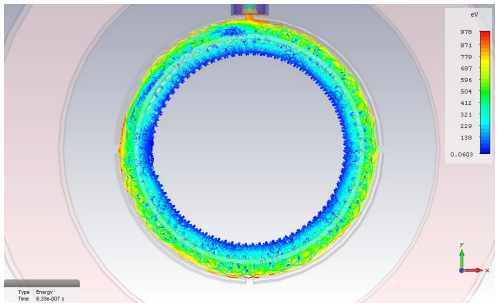

(a) $\Phi_{\text{source}} = 0.8\,\text{kV}$

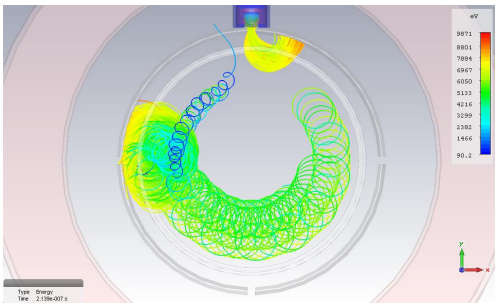

(b) $\Phi_{\text{source}} = 8\,\text{kV}$

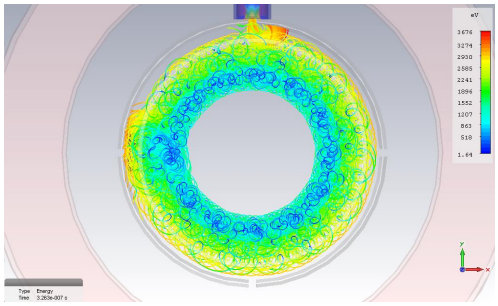

(c) $\Phi_{\text{source}} = 3.2\,\text{kV}$

Figure 2.8: Sweep of the potential difference between electron source and anode using the **internal** and **external source** with auxiliary coil and μ-metal shield. Neither a small potential nor the anode potential deliver an optimal penetration depth of the electrons, which is obtained at $\Phi_{\text{source}} = 3.2\,\text{kV}$. Parameters: $\Phi = 8\,\text{kV}$, $I_{\text{HC}} = 40\,\text{A}$ and $B_{\text{max}} = 34.73\,\text{mT}$.

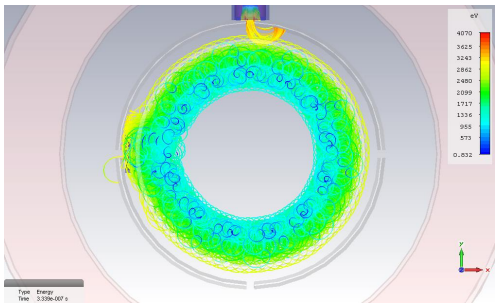

(a) $I_{\text{aux}} = 0\,\text{A}$, $B_{\text{aux}} = 0\,\text{mT}$

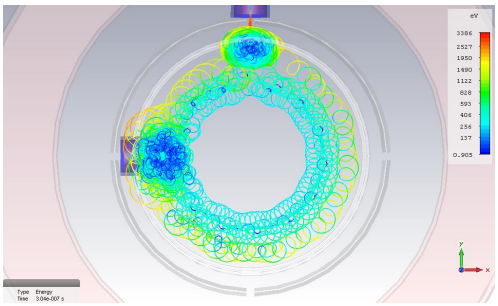

(b) $I_{\text{aux}} = 200\,\text{A}$, $B_{\text{aux}} = 717.72\,\text{mT}$

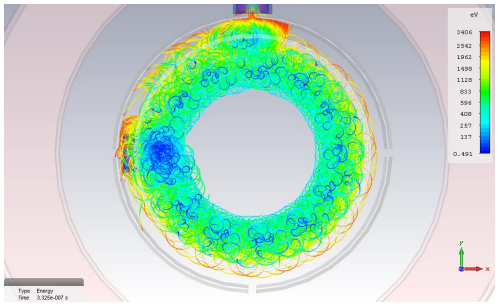

(c) $I_{\text{aux}} = 100\,\text{A}$, $B_{\text{aux}} = 353.86\,\text{mT}$

Figure 2.9: Sweep of the current in the auxiliary coil. Trajectories from **internal** and **external source** with auxiliary coil are plotted in this figure. If the current in the auxiliary coil is increased, more electrons are trapped near the sources. $\Phi_A = 8\,\text{kV}$, $I_{\text{HC}} = 40\,\text{A}$, $B_{\text{max}} = 34.73\,\text{mT}$.

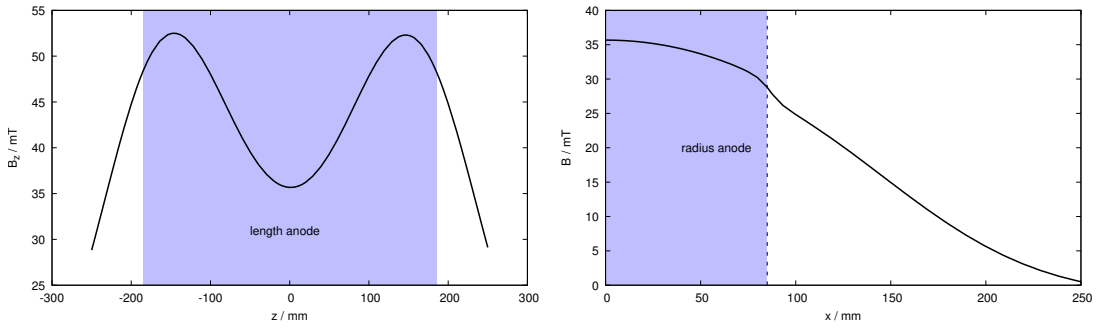

Figure 2.10: Left: Simulation of the magnetic field intensity in z direction along the z-axis. The depression in the centre is almost 50 % of the maximum magnetic field. Right: Simulation of the magnetic field along the positive x-axis.

in figures 2.8a, 2.8b and 2.8c.

Note that the trajectories predominantly belong to electrons from the inner source. The outer source generates losses on the anode, compare 2.8b. In a next step, the current through the auxiliary coil has been varied in order to make a transition of the electrons to the inner area possible. Unfortunately, the magnetic field used up to this point was already relatively large. The possibility of constructing a coil capable of providing even higher fields is questionable. The current in the auxiliary coil was increased from 0 A to 200 A. Some of the simulation results are shown in figures 2.9a, 2.9b and 2.9c. Varying the auxiliary coil current produced no more than a marginal effect on the penetration depth of the electrons. On the other hand, increasing the current led to accumulation of electrons near the sources. The higher the current, the fewer electrons were inserted into the lens volume. Decreasing the current to zero led to an electron distribution comparable to the optimal penetration depth achieved at 40 A in figure 2.8c, compare 2.9a. Therefore, using the auxiliary coil does not seem to provide a significant advantage for the system, so the coil might be removed in the final experiment.

2.3 Simulations of the Gabor plasma lens available at IAP

The lens available at the IAP is composed of two narrow coils that create the magnetic field. They were moved out of the Helmholtz configuration, because the Gabor lens used for these experiments was specifically designed in terms of the ratio between the anode radius, R_A, and the radius of the ground electrodes, R_p, as well as the ratio between R_A and the length of the anode [4]. Therefore, the coils had to fit the anode and thus had to be positioned with a larger distance between the centre of the coils as usual. As a result, the magnetic field in the lens is not homogeneous. Instead, the magnetic field strength along the z-axis has a depression in the centre, compare figure 2.10. A visual representation of the structure is displayed in figure 2.11. For convenience, the coils will be referred to as Helmholtz coils below. Both coils have 300 windings and an aperture of 300 mm.

2.3.1 Potential, electric and magnetic field

As the radius of the anode and electrodes is smaller than in the preliminary simulations, the potential is different, compare figures 2.2a and 2.12. Especially if the electron source is put on a different potential than the anode potential, the potential difference will cause local perturbations. This can be observed in figure 2.13. Here, the potential drops significantly close to the source. Furthermore, the potential of the source can be chosen with respect to the source position in order to minimize the disturbance of the potential distribution, compare the potential distribution for a source potential of 7.5 kV (red).

The electric field of the Gabor lens is generated by the potential difference between the anode, typically several kV positive, and the two ground electrodes. The structure is similar to the field of an einzel lens. The electric vector field is displayed in figure 2.14.

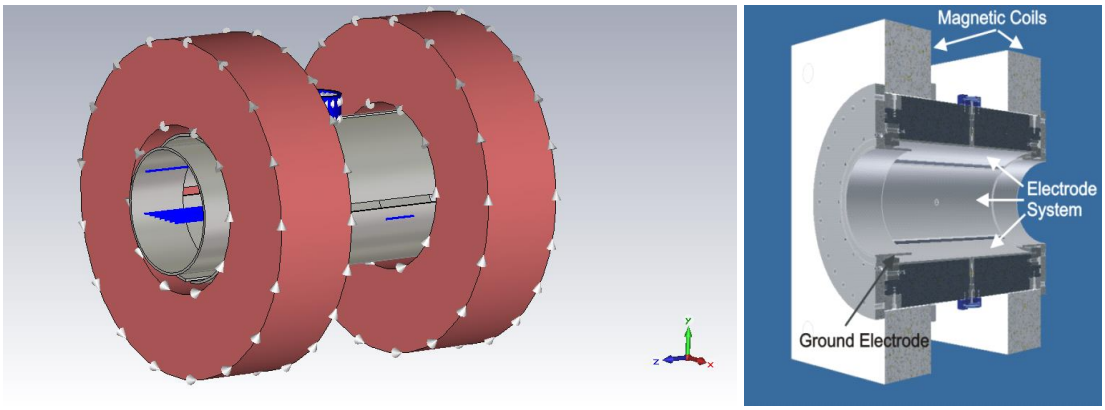

Figure 2.11: Design of the Gabor lens available at the IAP.

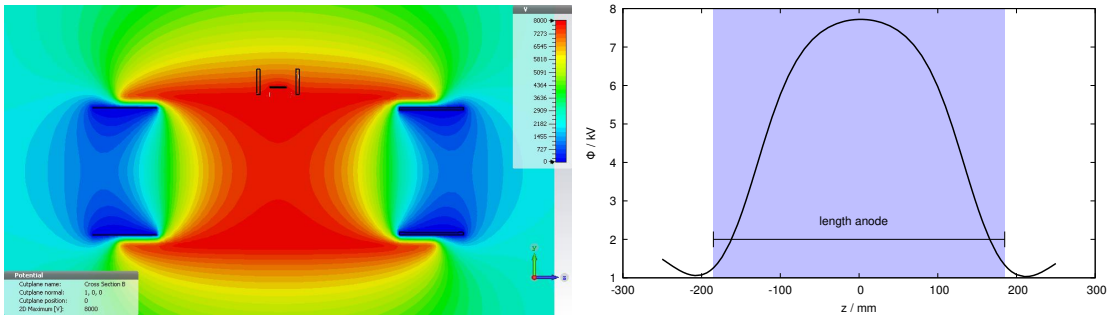

Figure 2.12: Left: The potential distribution in the Gabor lens that is available for experiments at the IAP. The potential in the centre of the lens is just slightly lower than the anode potential. This increases the longitudinal trapping efficiency corresponding to the previous setup. Due to its gaps, the anode is not visible in this image as two gaps are at the position of the cut in the yz-plane. Right: Potential distribution along the z-axis.

Comparing figure 2.3a and 2.15, the magnetic field changed a lot due to moving the Helmholtz coils out of ideal configuration, as discussed previously. Now, there is a more significant drop in the central magnetic field that was not visible in the previous configuration. Figure 2.16a contains the plots for the tangential magnetic field along the x-axis. Here, the position of the inner source can be observed at $x = 75\,\text{mm}$. Note that the tangential field created by the auxiliary coil is larger than the Helmholtz coil field by one order of magnitude. The tangential magnetic field along the y-Axis is shown in figure 2.16b. Here, the external source is located at $y = 90\,\text{mm}$.

Figure 2.16c shows the tangential magnetic field in z-direction. The effect of the auxiliary coil with 5 A current is insignificant. In order to demonstrate the effect of the auxiliary coil, a current of 100 A has been simulated. As shown in figure 2.15 the symmetry of the magnetic field is broken, which explains the shift in the magnetic field distribution to the right.

2.3.2 Auxiliary coil

Using an external source with an auxiliary coil in order to inject electrons into a the Gabor lens is troublesome, since the losses at the anode gap and the area where the auxiliary coil field merges with the Helmholtz field are significant. Furthermore, electrons that are injected into the inner anode volume are located at very large radii close to the anode surface. Most of these electrons are lost on the anode afterwards. The trajectories in figure 2.17 represent the best injection possible in these simulations.

2.3.3 Cusp and Gabor cusp structure

The basic idea of using a cusp configuration is to enable the electrons to penetrate to the inner region of the lens. Once the electrons are inside, the polarity of one Helmholtz coil could be

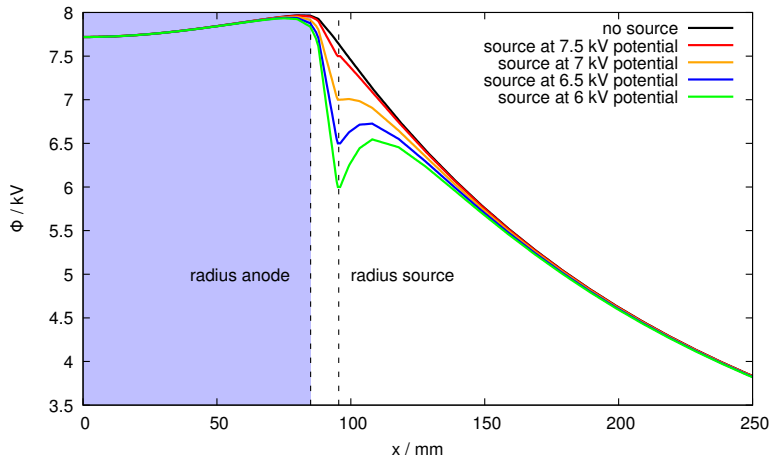

Figure 2.13: Influence of the electron source potential on the potential distribution along the y-axis in the auxiliary coil configuration. As the source is introduced(red), the potential is disturbed. If the source is put on a smaller potential with respect to ground (orange, blue, green) this effect increases.

reversed, creating a confining magnetic configuration. Unfortunately, this approach is restricted by a very short time that electrons stay in the lens and a relatively long time that is required to reverse the polarity of a coil.

It is possible that the original design by Gabor [1] offers a well-behaving electron cloud. Therefore, this design is used as a basis for the following simulations. A third coil has been added to create a cusp like magnetic field in the area of the electron sources, while the other coils create the magnetic confinement as usual. The electrons are expected to enter the internal region of the lens via the cusp and then propagate towards the region where magnetic confinement is provided.

The anode is therefore extended towards the cusp, as is seen in figure 1.1a, and the ground electrode is extended further away. The changes to the design can be observed in figure 2.19. Furthermore, a ring-shaped electron source consisting of two half rings is added to the setup at a slightly smaller radius than the anode radius in order to simulate the heated ring that was used in Gabor's experiments.

Necessary electron current in a cusp structure

Concerning the cusp-shaped magnetic field it has been observed that all simulated electrons injected orthogonally to the lens axis will propagate towards the ground electrodes on both sides and finally they will drift the same way back they came in. It is expected that most electrons are lost at the position of the cusp, unless they are lost in other loss channels, for instance the anode or ground electrodes. Comparing the trajectories shown in figure 2.19, the losses occur at the cusp position only. The current of electrons injected multiplied with the average time an electron stays in the cloud yields the number of electrons inside the lens. This fact can be used to find the electron density. The average time that electrons remain inside the lens is approximately $\tau = 9.44 \times 10^{-8}\,\mathrm{s}$, which is estimated from the simulation results shown in 2.18.

$$\begin{aligned} \tau I &= Q \\ \frac{Q}{V_p e} &= n_e \\ n_e &= \frac{\tau I}{V_p e} \end{aligned}$$

t is the time that electrons remain in the volume V_p, I is the current of the electron emitters, Q is the total charge of the electrons in the volume. In this way, n_e yields the density of electrons per volume. It is important to note that V_p is the volume of the plasma cloud, which is smaller

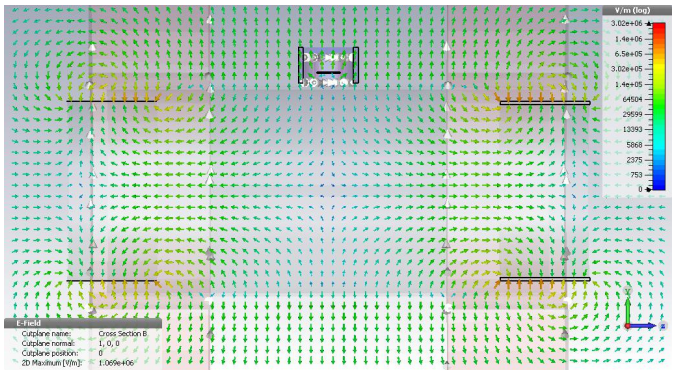

Figure 2.14: The electric field in non-Helmholtz configuration.

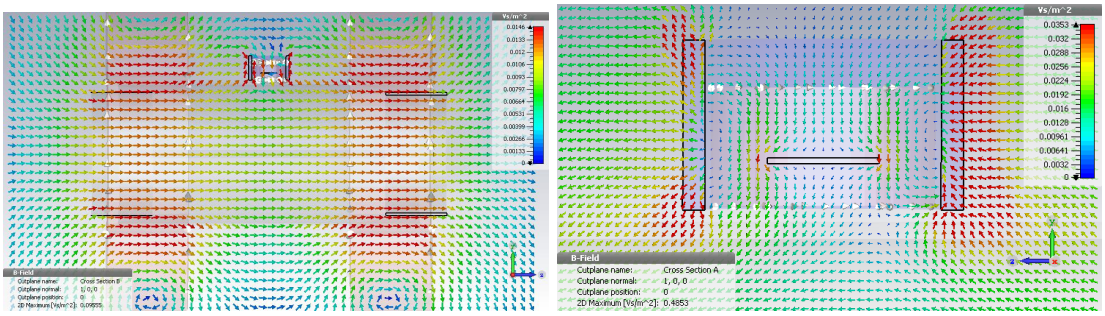

Figure 2.15: Top: The magnetic field in non-Helmholtz configuration. The intensity in the centre of the lens is smaller than in the area of the coils. Bottom: Close to the auxiliary coil, the field is perturbated and the symmetry is broken.

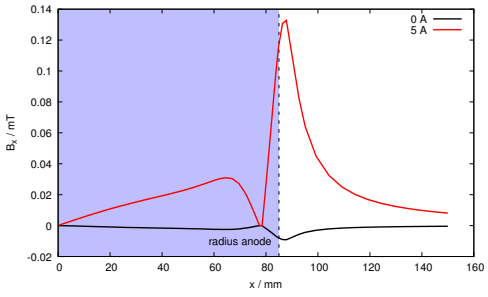

(a) Tangential magnetic field on the x-axis.

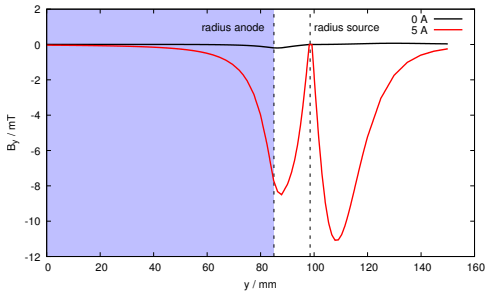

(b) Tangential magnetic field on the y-axis.

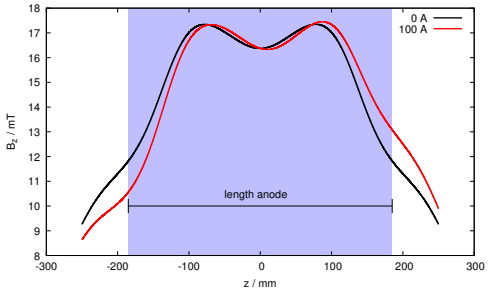

(c) Tangential magnetic field on the z-axis.

Figure 2.16: Tangential magnetic field along the cooordinate system axes. Compare figure 2.11 for the position of the electron source and the coordinate axes with respect to the Gabor lens. The origin is in the centre of the lens. Black: no current, red: 5 or 100 A in auxiliary coil.

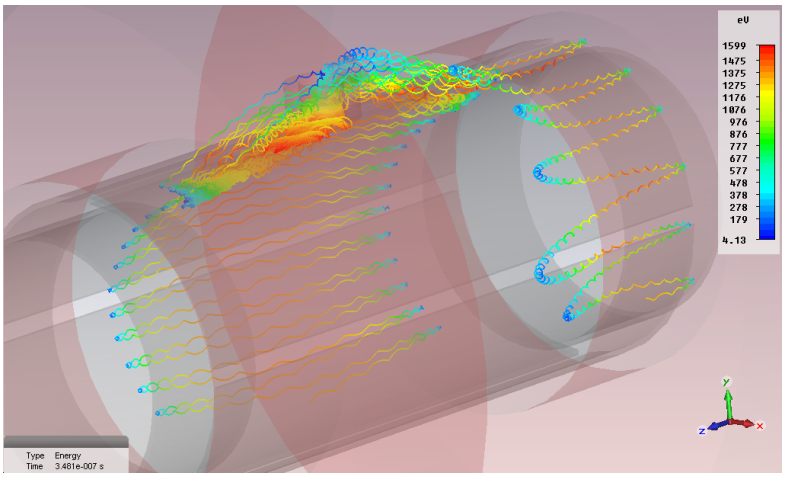

Figure 2.17: Trajectories using an external electron source with an auxiliary coil. Two electrons show an $E \times B$ drift movement, but only the electron on the left is inside the anode. The trajectory on the right is located outside the anode. Parameters: $\Phi_A = 8\,\mathrm{kV}$, $\Delta\Phi = 500\,\mathrm{V}$, $E_{el} = 1000\,\mathrm{eV}$, $I_{HC} = 40\,\mathrm{A}$ at 300 windings, $B_{\max} = 34.67\,\mathrm{mT}$; $I_{aux} = 12\,\mathrm{A}$ at 100 windings, $B_{\mathrm{aux}} = 42.53\,\mathrm{mT}$.

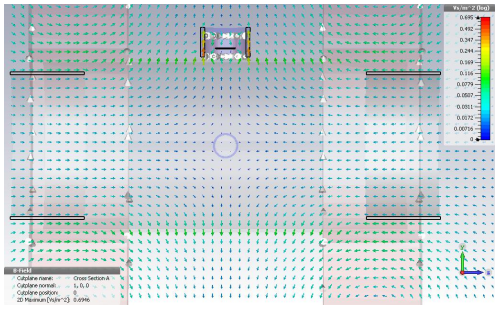

(a) Magnetic field

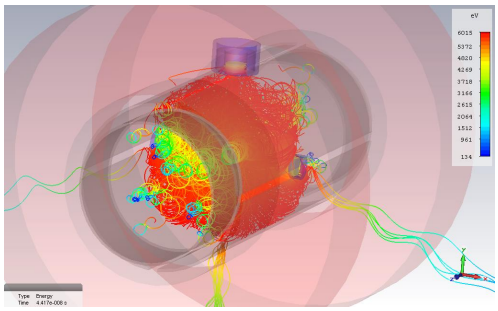

(b) Trajectories

Figure 2.18: On one hand, the filling of the lens seems to be quite good, on the other hand, losses are dramatically large. Parameters: $\Phi = 8\,\mathrm{kV}$, $E_e = 100\,\mathrm{eV}$, Helmholtz-Current: $I_{\mathrm{HC}} = 40\,\mathrm{A}$ at 300 windings, $I_{aux} = 20\,\mathrm{A}$ at 100 windings, $B_{\mathrm{aux}} = 70.87\,\mathrm{mT}$. The electron sources are on a 6 kV potential.

than the lens volume. Hence, the current that is needed to produce a desired density can be calculated:

$$I = \frac{V_p e}{\tau} n_e \tag{2.2}$$

This dependency is shown in figure 2.20. It is assumed that the volume of the plasma is slightly smaller than the lens volume. Therefore, we assume a radius of 70 mm instead of 75 mm and a cylinder length of 280 mm instead of 370 mm. Assuming a plasma volume of about $(0.07\,\mathrm{m})^2\pi \cdot 0.28\,\mathrm{m} = 0.0043\,\mathrm{m}^3$ and a desired density of approximately $1 \times 10^{14}\,1/\mathrm{m}^3$, compare [8], we get:

$$I = 0.73\,\mathrm{A}$$

Effects of the residual gas on the necessary current in a cusp configuration

The residual gas in a Gabor lens is ionized by free electrons and acts as the main electron supplier in the lens. Therefore, the residual gas may provide many electrons even under good vacuum conditions when the electron emitters are in operation. Therefore, the effect of the residual gas as

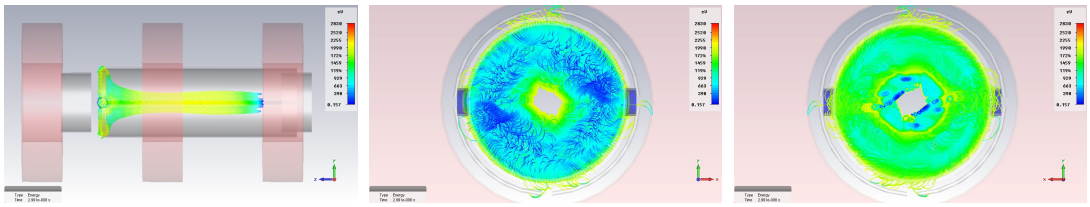

(a) Side view (b) Front view (c) Back view

Figure 2.19: Trajectories of the Gabor cusp setup used in [1]. The electrons propagate towards the region where magnetic confinement is given, but they are able to return to the electron sources, probably getting lost on walls. The parameters in this simulation are: $\Phi = 8\,\mathrm{kV}$, $E_e = 2000\,\mathrm{eV}$, Helmholtz current: $I_h = 40\,\mathrm{A}$ with 300 windings, $B_{\max} = 34.67\,\mathrm{mT}$. The electron sources are kept at $\Phi_s = 7.9\,\mathrm{kV}$.

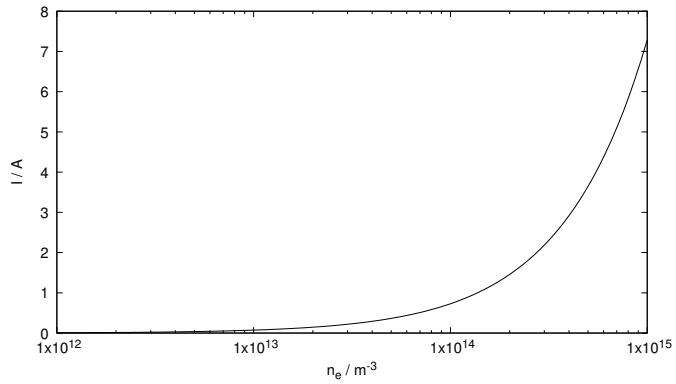

Figure 2.20: Theoretical current of the electron emitters with respect to the desired density. The current is restricted by the energy deposition of the loss currents, which rise with the elecron source current. The losses at the walls in the cusp zone would be devastating for the materials. Equation (2.2) is linear, nevertheless the magnitude of the density is important.

supplier for electrons is estimated. The mean free path of the electrons depends on the ionisation cross-section σ and the density n_g of the residual gas.

$$\lambda = \frac{1}{n_g \sigma}$$

As we are interested in ionizing the nitrogen gas, we use the cross-section for ionization of nitrogen with electrons. This cross-section depends on the electron energy and is plotted in figure 2.21. As the cross-section is at it's maximum at 100 eV, the electron source should be operated close to 100 eV energy in order to increase the amount of electrons introduced by residual gas ionization. If the electron source is not put on the anode potential, the electron energy has to be chosen according to the expected energy inside the Gabor lens. Nevertheless, as the emission from an electron source depends on the extraction voltage, the extraction voltage has to be balanced with the energy in the lens in order to observe many ionizing events. The electrons injected from the side into the Gabor lens in cusp configuration travel to the centre of the lens, then continue to the ground electrodes. Afterwards, they return to the area of the electron emitters using almost the same path. We approximate the length of this path by the following calculation. Assume that the length of travel without gyrations in the cusp structure is given by the distance between electron source and centre of the cylinder and the distance an electron is able to move longitudinally. The distance between electron source and centre of the cylinder is 75 mm and the distance from the centre to the position of the electron that travelled furthest is 150 mm. These values have been obtained from the simulation results shown in figure 2.18. As the electrons first travel from the electron source to the centre, secondly continue along the symmetry axis until they are repelled by the potential and move back to the centre and afterwards to the electron

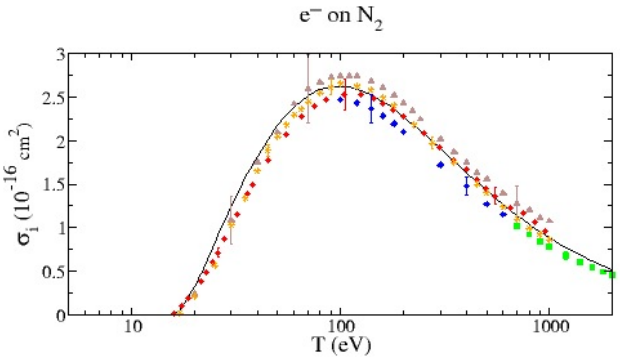

Figure 2.21: N_2 ionization cross-section, taken from [18].

source, the total distance covered can be estimated:

$$l_r = (2 \cdot 75\,\text{mm} + 2 \cdot 150\,\text{mm}) = 450\,\text{mm} = 0.45\,\text{m}$$

In the following, it is assumed that this path is travelled in a homogeneous magnetic field parallel to the magnetic field lines without measuring the effect of the gyration. In this case, the velocity is split into components parallel (v_z) and perpendicular (v_ϕ) to the magnetic field. Both are connected via the initial kinetic energy of the electrons, which allow us to find the azimuthal velocity in terms of the velocity in z-direction:

$$v_\phi^2 = \frac{2E}{m} - v_z^2$$

Using the Pythagorean theorem, the total distance travelled by the electron can be estimated, assuming that the radius of the gyration is constant. Here, l_ϕ can be expressed as the circumference of a circle with the Lamor radius:

$$\begin{aligned} L^2 &= l_z^2 + l_\phi^2 \\ &= v_z^2 \Delta t^2 + \frac{4\pi^2 v_\phi^2}{e^2 B^2} \\ &= v_z^2 \left(\Delta t^2 - \frac{4\pi^2 m^2}{e^2 B^2} \right) + \frac{8\pi^2 m}{e^2 B^2} E \end{aligned}$$

This can be simplified by expressing v_z with the measured length l_z and solving for L.

$$\boxed{L = \sqrt{\frac{8\pi^2 m E}{e^2 B^2} + \left(1 - \frac{4\pi^2 m^2}{e^2 B^2 \Delta t^2}\right) l_z^2}}$$

Inserting the variables, especially $l_z = 0.45\,\text{m}$, $\Delta t = 9.44 \times 10^{-8}\,\text{s}$ and $B = 22.4\,\text{mT}$, the total distance travelled in such a system resolves to $L = 0.58\,\text{m}$. Now, the number of ionizing collisions during the path of one electron N_i, assuming that N_2 is the only residual gas, can be estimated using the mean free path λ:

$$N_i = \frac{L}{\lambda}$$

As we know the average number of ionization processes for one electron, we can calculate the total number of ionizations by multiplying with the number of electrons N:

$$N_{i,tot} = N N_i = n_e V_p \frac{L}{\lambda} = n_e V_p L n_g \sigma$$

Or written in dependency of the current of the electron sources:

$$N_{i,tot} = \frac{\tau I}{e} L n_g \sigma$$

Now, it is possible to calculate the total number of ionization processes:

$$
\begin{aligned}
n_e &= 1 \times 10^{15}\,1/\mathrm{m}^3 \\
p &= 1 \times 10^{-6}\,\mathrm{mbar} = 10 \times 10^{-4}\,\mathrm{Pa} \\
pV &= Nk_bT \\
\rightarrow n_g &= \frac{N}{V} = \frac{p}{k_bT} = \frac{10 \times 10^{-4}\,\mathrm{Pa}}{1.38 \times 10^{-23}\,\mathrm{J\,K^{-1}} \cdot 293\,\mathrm{K}} = 2.47 \times 10^{16}\,1/\mathrm{m}^3 \\
\sigma &= 1 \times 10^{-16}(0.01\,\mathrm{m})^2 = 1 \times 10^{-20}\,\mathrm{m}^2 \\
\rightarrow \lambda &= \frac{1}{n_g\sigma} = \frac{1}{2.47 \times 10^{16}\,1/\mathrm{m}^3 \cdot 1 \times 10^{-20}\,\mathrm{m}^2} = 4048.58\,\mathrm{m} \\
L &= 0.58\,\mathrm{m} \\
\rightarrow N_i &= \frac{L}{\lambda} = 0.000143 \\
V_p &= 0.004\,308\,\mathrm{m}^3 \\
\rightarrow N_{i,tot} &= n_eV_pLn_g\sigma \\
&= 1 \times 10^{15}\,1/\mathrm{m}^3 \cdot 0.004\,308\,\mathrm{m}^3 \cdot 0.58\,\mathrm{m} \cdot 2.47 \times 10^{16}\,1/\mathrm{m}^3 \cdot 1 \times 10^{-20}\,\mathrm{m}^2 \\
&= 61716408 \approx 6.17 \times 10^7
\end{aligned}
$$

Both, electrons introduced by an electron source and electrons from residual gas ionization (RGI), can provide further electrons via RGI. Therefore, each electron could be described in terms of the amount of RGIs that were necessary in order to supply the respective electron. Therefore, electrons that are supplied by RGI with an electron directly from the electon source are referred to as first-order electrons. Hence, second-order electrons are supplied by RGI with a first order electron.

The number of electrons created by ionization of the residual gas in first order is several magnitudes smaller than the number of electrons injected. Nevertheless, with these results, we can calculate the required current of electrons producing a desired electron density in the lens again. Therefore, we start by solving equation 2.2 for the electron density:

$$n_e = \frac{\tau I}{V_p e}$$

The electrons that are produced by first-degree RGI can be calculated by comparing the total number of expected ionization processes $N_{\mathrm{i,tot}}$ to the volume of the plasma cloud:

$$n_{e,i} = \frac{N_{\mathrm{i,tot}}}{V_p} = \frac{\tau I}{V_p e} L n_g \sigma$$

N_e is the number of electrons. $n_{e,i}$ is the electron density that is added to the inserted electron density through ionization of N_2 gas. Therefore, we find:

$$n_e^* = n_e + n_{e,i} = \frac{\tau I}{V_p e}(1 + Ln_g\sigma) \tag{2.3}$$

Here, the correction factor $Ln\sigma$ is of magnitude 10^{-4}. Therefore, the effect of the correction is supposed to be small. This leads to the corrected current:

$$I^* = \frac{V_p e}{\tau(1 + Ln_g\sigma)} n_e^* \tag{2.4}$$

Although the correction of the current is small, the secondary electrons created through ionization are prone to be accelerated and create tertiary electrons and so forth. As the cross-sections are small, the number of the tertiary electrons is expected to be much smaller than the number of secondary electrons. This can be understood by writing the added density in k^{th} order of residual gas ionization as a geometric series. The k^{th} grade density can be written iteratively, compare equation 2.3:

$$
\begin{aligned}
n_{k+1} &= n_k L n_g \sigma \\
n_0 &= n_e
\end{aligned}
$$

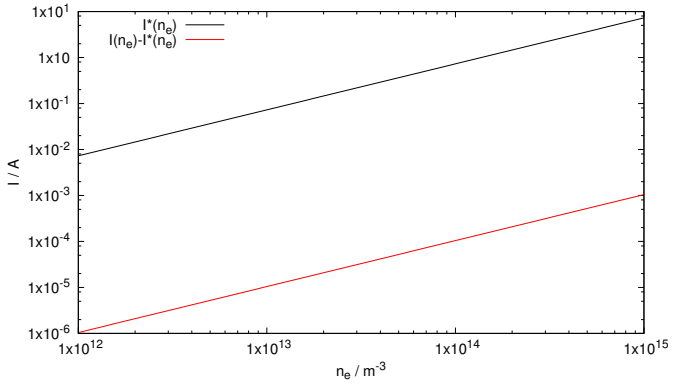

Figure 2.22: The corrected theoretical current $I^*(n_e)$. As the correction to the previously calculated current $I(n_e)$ shown in figure 2.20 is insignificant, the difference between both currents is plotted in red.

Here, n_e is the density of electrons introduced by the electron beam. The total amount of electron density accumulated in the Gabor lens, $n_{\mathrm{i,tot}}$, can be expressed as the limit of the series:

$$\begin{aligned} n_{\mathrm{i,tot}} &= \lim_{j\to\infty} \sum_{k=0}^{j} n_k \\ &= n_e \lim_{j\to\infty} \sum_{k=0}^{j} (L n_g \sigma)^k \end{aligned}$$

This is a geometric series that converges, since $L n_g \sigma < 1$:

$$n_{\mathrm{i,tot}} = \frac{1}{1 - L n_g \sigma} n_e = 1.00014 \cdot n_e$$

The impact of this correction is shown in figure 2.22. Since the correction is small, further iterations can be neglected with small error and equation 2.4 yields a good approximate of the necessary electron current, taking residual gas ionization into account.

On the other hand, these simulations have been carried out with a rather short simulation time. The time that is simulated is much shorter than a second. In a real application, times in the magnitude of several minutes matter. Therefore, the effect of secondary electrons due to residual gas ionization may be significantly larger in a real experiment.

2.3.4 Internal shielded source

Also for this setup, a set of parameters can be found that allows for an $E \times B$ drift so that the electrons are able to be confined. Sample trajectories are shown in figure 2.23. The second picture does not show the trajectories of electrons that were lost during the simulation. Most of the electron trajectories from the first image are also present in the second one, therefore, most electrons are inserted into the Gabor lens and are confined with minor losses. Further effects, such as space charge, that are not simulated by CST, could provide a radial drift or diffusion, allowing the electrons to distribute in the entire volume. Most of the other sources do not show promising trajectories at these parameters, which are: $\Phi = 8\,\mathrm{kV}$, $E_e = 100\,\mathrm{eV}$, Helmholtz-Current: $I_h = 40\,\mathrm{A}$ with 300 windings, $I_{aux} = 20\,\mathrm{A}$ with 100 windings. The electron sources are on a 7.5 kV potential, so $\Delta\Phi = 500\,\mathrm{V}$.

Because of the promising results, the simulation was repeated with 4 kV anode potential and 8.97 A current in the Helmholtz coils, as these parameters are possible to be achieved in the experiment and the magnetic field corresponds to the given potential according to the work function, compare equation (1.15). Therefore, the simulation results may be compared to subsequent measurements. Figure 2.24 displays the resulting trajectories. First, all trajectories are plotted

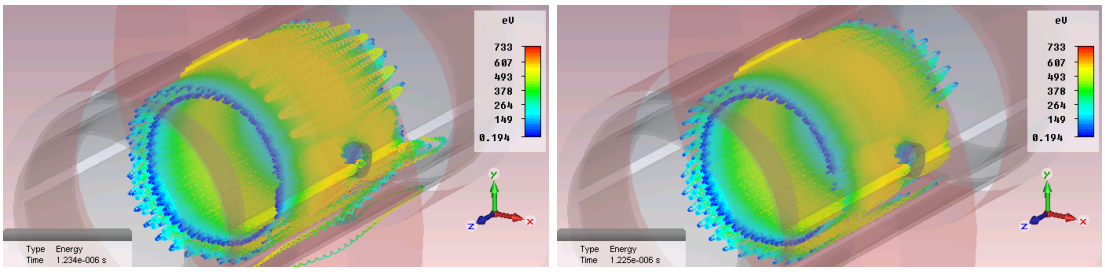

Figure 2.23: $E \times B$ drift of the electrons in the Gabor lens. This state forms a basis for further simulations, as electrons are confined. Top: all trajectories, bottom: no crashed particles are drawn. Parameters: $\Phi_A = 8\,\mathrm{kV}$, $\Delta\Phi = 500\,\mathrm{V}$,$E_{el} = 100\,\mathrm{eV}$, $I_{HC} = 40\,\mathrm{A}$ at 300 windings, $B_{\max} = 34.67\,\mathrm{mT}$.

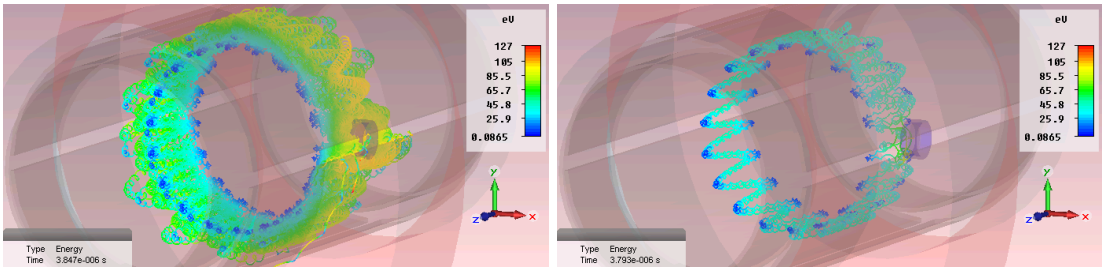

Figure 2.24: Left: Simulation with all trajectories. Right: Only trajectories that did not collide with a wall or boundary are drawn. Parameters $\Phi_A = 4\,\mathrm{kV}$, $\Delta\Phi = 0\,\mathrm{V}$, $E_{el} = 100\,\mathrm{eV}$, $I_{HC} = 8.97\,\mathrm{A}$, 300 windings, $B_{\max} = 7.77\,\mathrm{mT}$.

(left) and second, only the trajectories that did not lead to electron loss are shown (right). In this case, far more electron losses occur than in the simulation with 8 kV anode voltage and 40 A Helmholtz current. An important difference between the two simulations is the value of $\Delta\Phi$ between anode and electron source. In the present simulation, $\Delta\Phi = 0$ was chosen since many measurements were conducted with the electron source being on the anode potential.

2.4 Simulations using bender

Bender is a particle-in-cell (PIC) simulation code written at IAP by Daniel Noll [17]. This non-relativistic code is designed for the investigation of low-energy beam transport in various configurations, taking account of space charge effects.

Written in C++, bender has many comfortable features for operation including input files defining the details of the simulation, supporting SI units for physical magnitudes, and the ability to import field configurations from other simulation codes such as CST studio suite. Several algorithms for integrating the equation of motion for the charged particles that may be defined to the user's desire are implemented in the code. The bender code is furthermore able to simulate the interaction between charged particles due to their space charge and implement residual gas ionization via the electrons that are in the system. Both effects are analysed in the upcoming sections.

If space charge effects are simulated, three solvers are available in order to solve Poisson's equation, each showing different assets and drawbacks, specializing in a defined discipline. For instance, a Cartesian solver using the Shortley-Weller finite difference method can be utilized if the problem contains a complex geometry with no symmetry that can be exploited. Here, the drawback is the increase in computation time. If a radial symmetry is available, the rz finite difference solver can be used, being much more efficient due to the symmetry. Finally, the 3D xyz Fourier solver can be implemented, if a equidistant grid suffices to describe the problem. Although the simulation of inserting electrons into a Gabor plasma lens contains geometries on a very small scale, such as the electron source, and geometries that are on a larger scale, such as the plasma volume, the Fourier solver has been chosen to calculate the space charge simulations

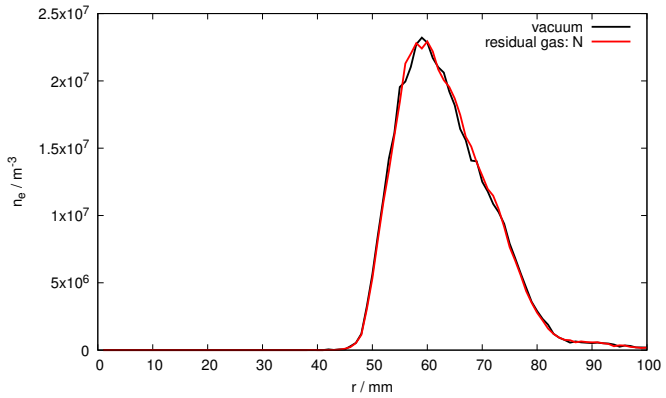

Figure 2.25: Here, a torus-shaped electron cloud is observed for the internal source configuration.

due to its simple use and increased efficiency with respect to the 3D finite difference solver.

In the following simulations, the bender code calculates a certain influx of electrons at a given current by inserting a user-desired number of macro particles into the Gabor lens each time step. This number of macro particles does not necessarily equal the number of electrons that are supposed to be inserted in order to achieve the given current. Instead, the macro particles represent a collection of electrons. The number of electrons represented by a single macro particle can be calculated in the following fashion, starting with the current out of the electron source that is divided into macro particles and electrons:

$$n = \frac{It}{em}$$

Here, m is the number of macro particles inserted in each time step, ne is the charge of a single macro particle. m is specified by the user while n is calculated.

2.4.1 Electron density

A short Java code is used to evaluate the radial electron density in the simulated Gabor lens. Hereby, the number of particles on concentric rings with a given width in radial direction around the centre of the Gabor lens is calculated. Finally, the particles are multiplied by a factor as discussed above to find the number of electrons and plotted versus the radius. In this visualization, the electrons are integrated in z-direction. The electron density was simulated in vacuum and with a residual nitrogen gas at 10^{-5} mbar and 300 K. The density evaluated with simulated residual gas is plotted in black, the results for vacuum are displayed in red, compare figure 2.25. The difference between both density distributions is very small. Probably the simulation with residual gas did not run long enough for ionization effects taking place, as their cross-sections are rather small. These observations match the results obtained by CST, compare figure 2.23, as the electrons are located at a large radius. Both simulations show a torus-shaped electron distribution.

In order to investigate the structure of the electron density further, the density distribution is evaluated two-dimensionally, compare figure 2.26. In the following pictures, the colour scale reflects the density of electrons in units of $1/\mathrm{m}^3$. The density is evaluated inside the lens only; therefore, electrons that were able to escape the confinement in the simulations are ignored.

The two dimensional density evaluation reveals that the electrons form a rather large cloud at the source. The source is located on the x-axis at $y = z = 0$, which can be seen in figure 2.23, compare the μ-metal ring in blue located on the right. The density distribution in figure 2.26 indicates that most of the electrons are confined near the electron source, which has been been observed in CST before, as many losses are located near the electron source.

2.4.2 Time-dependent density distribution

With the help of these simulations, we are able to observe the evolution of a fixed amount of electrons that are inserted into the Gabor lens at a certain place. In this case, the electron

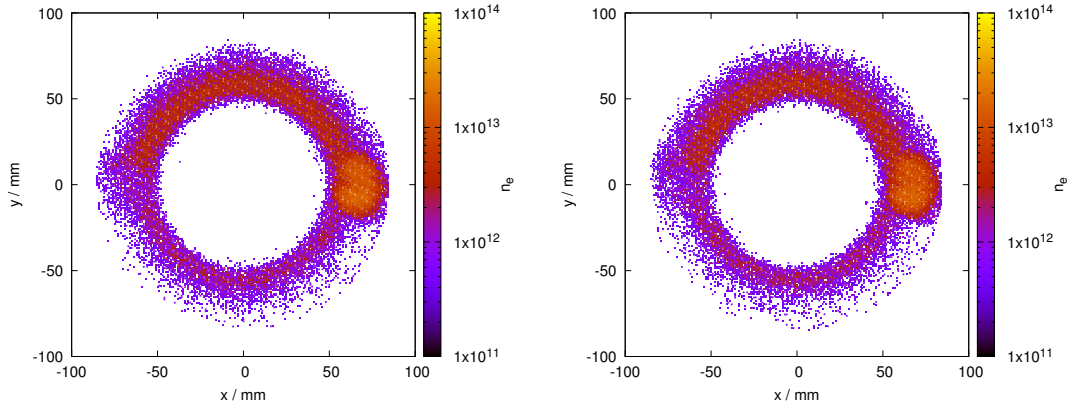

Figure 2.26: Two-dimensional density distribution of the electrons in the Gabor lens using the internal source configuration with a residual N_2 gas (left) and in vacuum (right). The density is encoded in colour and is measured in $1/m^3$. This has been calculated with 4 mA electron current. Again, simulating the residual gas ionization has a very small effect on the outcome of the simulation, as both images are very similar.

source is only active in the first time step and is shut down afterwards. Therefore, we observe the development of an initial electron distribution in the shape of a thin circular plate. The images 2.27 and 2.28 show snapshots of the density distribution of the electrons, whereby the time that has passed in the simulation is noted at the top of each image. The initial electron energy is 100 eV We can observe the xy- and the zy-planes. The view on the xy-plane corresponds with the CCD images we are able to take in an experiment. If we place the camera transversally with respect to the symmetry axis of the Gabor lens, we could observe the density distribution in the yz-plane. Because of the hardware necessary to operate a Gabor lens, especially the anode system and the coils, taking images transversally is very difficult in an experiment and requires a special anode and Helmholtz coil system.

2.4.3 Energy

The energy of the electrons emitted by an electron source is easily adjustable and has a major effect on the experiment. The shape of the density distribution may depend on the initial energy of the electrons, as figure 2.8 suggests. Furthermore, other parameters, such as loss distribution on the anode, will probably depend on the energy. Therefore, simulations with various energies will unveil optima in terms of losses and electron distribution.

It is desirable that a homogeneous electron distribution is achieved in order to use the lens as a focussing optic. Therefore, it is necessary for the inserted electrons to be able to reach the centre part of the lens. As the structure is similar to a teltron tube experiment, it can be assumed that the radius the electrons show during their propagation through a magnetic field is:

$$r = \sqrt{\frac{2Um}{eB^2}}$$

Here, U is the potential accelerating the electrons. Increasing the energy should yield a larger radius of the electron beam; therefore, the beam should be able to penetrate closer to the centre of the Gabor lens as it is injected transversally into a magnetic field. Furthermore, the electron beam has to overcome a potential difference between the anode and the central part of the lens, compare figure 2.12. Again, increasing the energy should enable the electrons to reach the central part of the lens; probably, some hundred eV should suffice.

Multiple bender simulations in the internal source configuration in vacuum with varying energies from 0 eV up to 2000 eV in steps of 10 eV have been analysed in terms of the radial position of the density maximum (black) and the smallest radial position of any electron in the simulation (red). The results are shown in figure 2.29a. Increasing the energy shows only a marginal effect on the position of the mean radius. Comparing figure 2.26, this may be explained by the aggregation of electrons close to the electron source. Nevertheless, modifying the energy

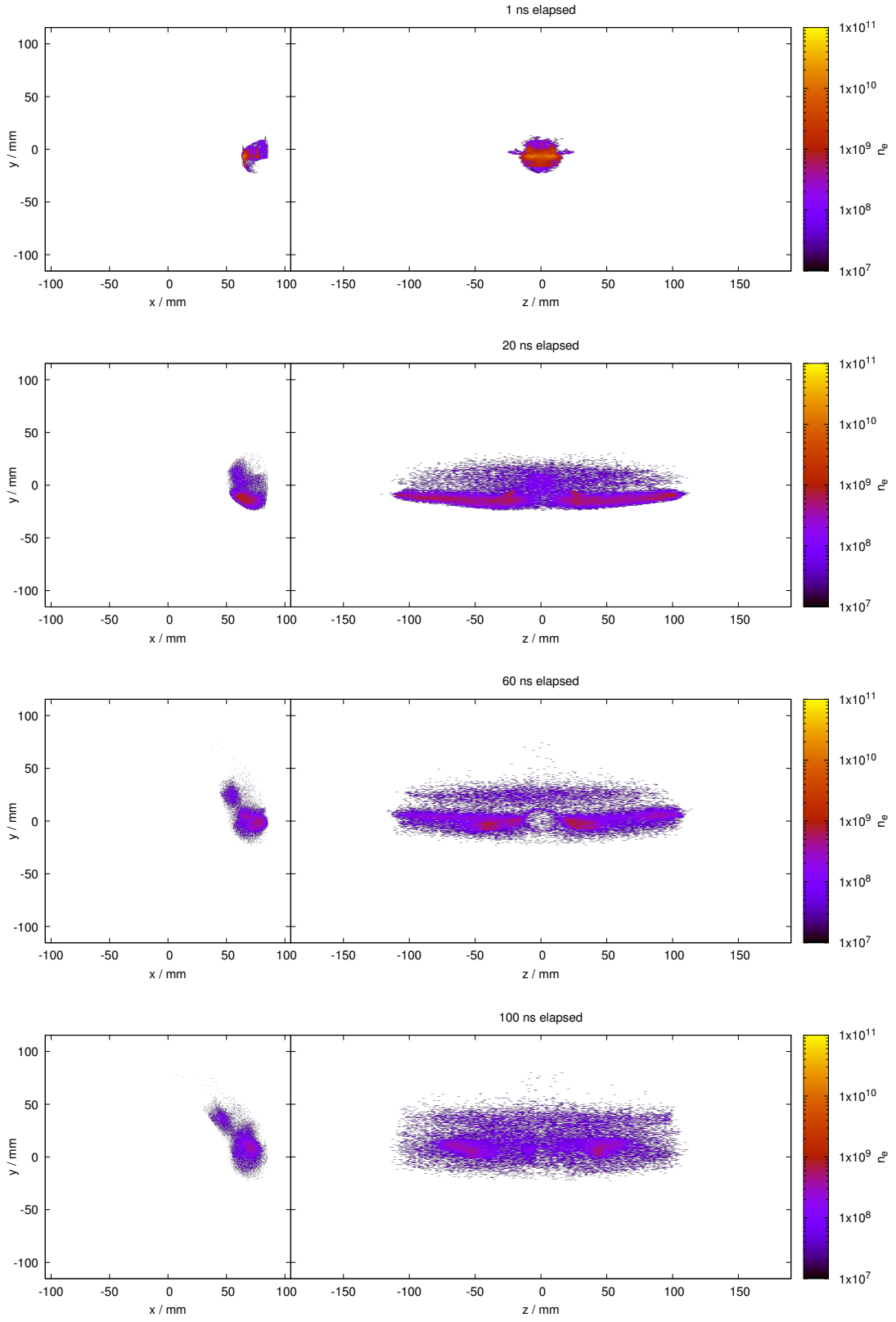

Figure 2.27: Two-dimensional density distribution after 1 ns, 20 ns, 60 ns, 100 ns. After a short time, the electrons split into two symmetric clouds in z-direction. After 60 ns, we can observe a small cloud of electrons that starts to perform an $E \times B$ drift.

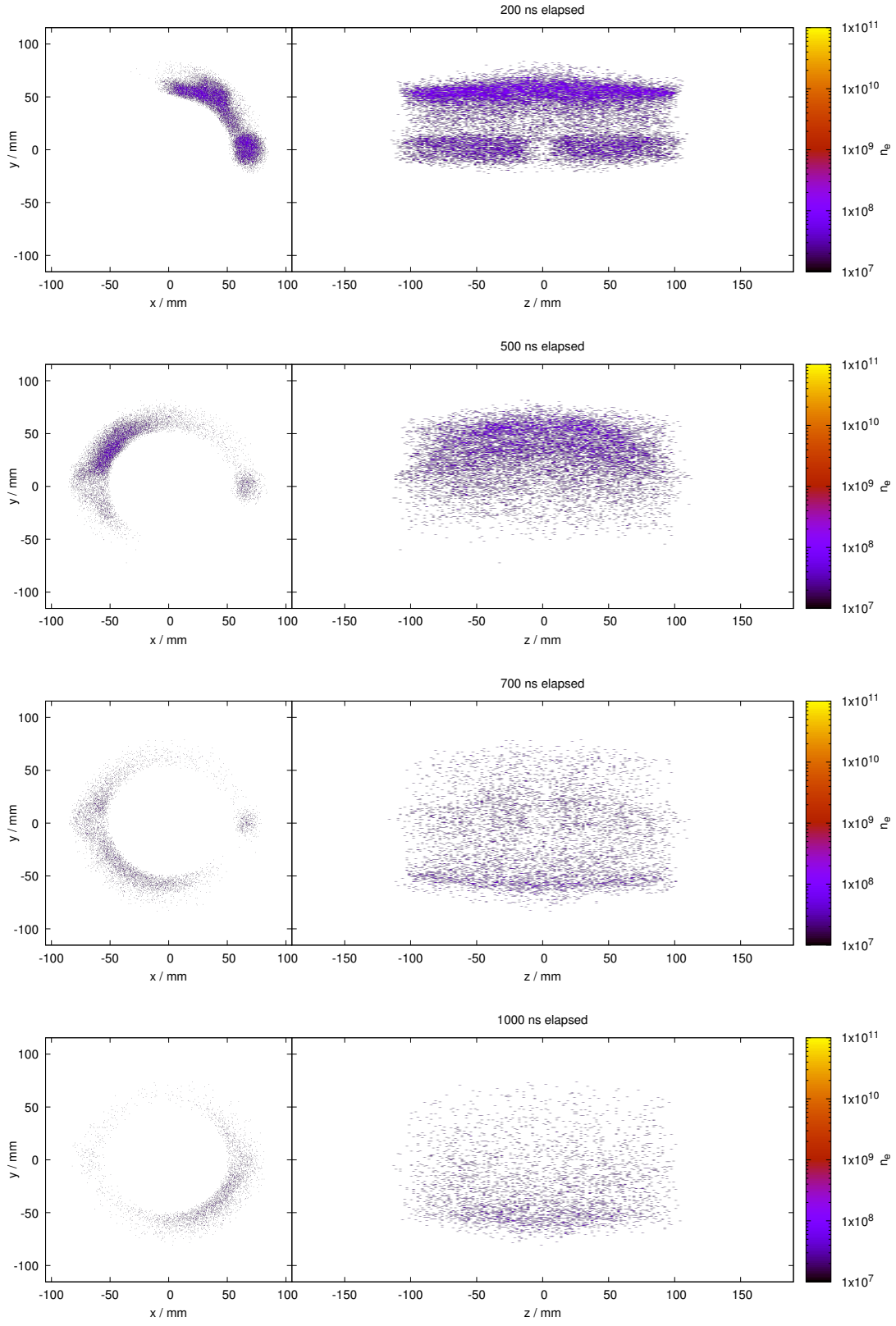

Figure 2.28: Two-dimensional density distribution after 200 ns, 500 ns, 700 ns, 1000 ns. After some time, more electrons aggregate in the cloud, which performs an azimuthal drift. The electrons that remain close to the position of the source get lost. Furthermore, the electron distribution continues to form a torus cloud. As there are losses in the system, the mean density decreases over time.

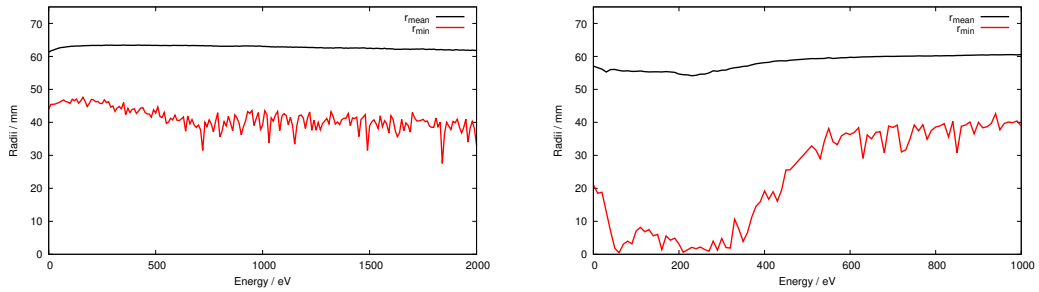

(a) Without space charge (b) With space charge

Figure 2.29: Plot of the mean radius of all electrons at a given energy and the position of the electron that is located at the smallest radius. $\Phi = 8\,\mathrm{kV}$, $\Delta\Phi = 0.5\,\mathrm{kV}$ and $I_{\mathrm{HC}} = 40\,\mathrm{A}$.

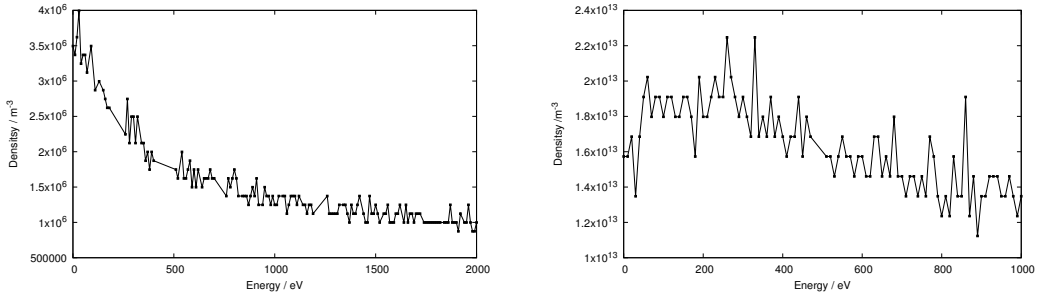

(a) Without space charge (b) With space charge

Figure 2.30: Plots of the maximum achievable density during the energy sweep simulations with respect to the given energy. Left: Without space charge, right: with space charge. $\Phi = 8\,\mathrm{kV}$, $\Delta\Phi = 0.5\,\mathrm{kV}$ and $I_{\mathrm{HC}} = 40\,\mathrm{A}$.

has some effect on the radius of the electron closest to the centre of the Gabor lens, r_{min}. A maximum can be observed at approximately 200 eV. Between 750 eV and 2000 eV, r_{min} does not show a clear dependency on the electron energy but resembles a noisy signal. In general, it could be useful to choose 750 eV as electron energy.

As the density in the Gabor lens is a very significant quantity, it is important to analyse the maximum density that is achieved with respect to the electron energy, which is performed in figure 2.30. In the case of the simulations without space charge, the density is decreasing with increasing energy after showing a narrow maximum close to a few eV. In general, the maximum density is in the magnitude of $10^6\,1/\mathrm{m}^3$.

2.5 Space charge simulations using bender

Simulation of the space charge - in this case the electric field of the electrons and the interaction between electrons - is rather difficult. As discussed previously, several solvers for Poisson's equation are implemented in bender. The scenario in a Gabor lens is difficult, because none of the advantages of the three solvers can be exploited fully. The space charge simulation is therefore conducted utilizing the Fourier transformation algorithm to find the electric field created by the electrons, because it is the solver most suited for this difficult scenario. If the electron density is low, this algorithm may introduce statistic noise to the electric field with increasing intensity the longer the simulation is running [19]. Furthermore, it has been shown that a very small grid size is needed to resolve the electron beam or any ion beam. In addition, the envelopes of the simulated beams are not perfectly described by a simulation because of the relatively small density compared to the centre of a beam, compare [19]. As the simulation of the Gabor lens is merely a simulation of an electron cloud and not of a laminar ion or electron beam, the problems that arise with the simulation of beam edges can be expected here throughout the entire ensemble of electrons. As the simulation of space charge is complex, a dramatic increase in computing

time can be expected.

2.5.1 Energy

In order to evaluate the previous simulations, the energy sweep simulations are repeated with space charge effects taken into consideration while all other parameters are kept constant. In this configuration, at least single electrons are able to reach a very small radius if their initial energy is in the range of roughly 50 to 300 eV, compare figure 2.29b. As the simulations are using space charge effects, they are supposed to be more realistic than the previous simulations, which is why choosing the electron energy in the range of 50 to 300 eV is preferable over larger energies. In addition, space charge effects introduce a new radial force to the ensemble of electrons; therefore, the electrons are more likely to distribute inside the lens by drifting in radial direction.

2.5.2 Density distribution

As mentioned before, a homogeneous density distribution is often assumed in theoretical work concerning space charge lenses. A homogeneous density distribution offers the best focussing performance. As the density distribution does most probably depend on the method of injecting electrons with an electron source, simulations are used to indicate the resulting density distribution at given parameters. Concerning previous simulated density distributions comparable to figure 2.26, the space charge effects should be taken into account in the simulations, as first, they represent a better approximation of reality than ignoring the electric field created by the electrons and second, space charge effects seem to be key for electron distribution in the Gabor lens and therefore should be taken into account. This can be observed in figure 2.29, showing indicators for a dissolved torus density distribution for energies up to 400 eV.

The chance to observe an equilibrium of the system is only given if the simulation has enough time to reach it. Therefore, the system was prepared and the simulation was set to run for a very large number of simulation steps. The results shown in the scope of this section were achieved by running the simulation for several weeks, covering a simulated time of 5×10^{-5} s at a resolution of 5×10^{-11} s each step.

This simulation can be characterised by three phases. First there is a tuning phase (see figure 2.31) that forms a torus-shaped electron density very similar to the results obtained in figures 2.27 and 2.28. The second phase shows the build-up of an instability. It starts with a thickening of one part of the torus that forms a plasma wave propagating around the torus and finally dissolving the structure, compare figure 2.32. Finally, the electron density distribution converges to an almost homogeneous density distribution with an asymmetric hole that rotates around the symmetry axis. See figure 2.33.

2.6 Conclusions of the simulations

After investigating different geometries in CST and bender, several results have been obtained. First, the geometries have different strengths and weaknesses. Especially all geometries utilizing a cusp shaped magnetic field suffer increased electron losses that can only be balanced by increasing the current out of the electron source by several orders of magnitude.

Furthermore, it is important to put the electron source on a potential, as the potential distribution in the plasma volume is heavily disturbed otherwise. In addition, installing a small coil with a magnetic field in electron beam direction breaks the symmetry of the magnetic field, leading to decreased emission characteristics of the electron source. The transversal magnetic field should be dampened by a μ-metal shield only.

Additionally, the results shown in the long term simulation in figures 2.31, 2.32 and 2.33 show that a state comparable to the desired homogeneous density distribution can be achieved by inserting electrons with an electron source transversally. Nevertheless, only a timespan of 50 µs is covered in the simulations. Although it appears that the final state shown in figure 2.33 is stable, this might not be the case for time scales up to a second.

In conclusion of the simulation results, it was decided to realize the internal source configuration and test the emission properties, as well as the impact of an electron beam in terms of ignition behaviour and density boosting of the enclosed plasma in an experiment.

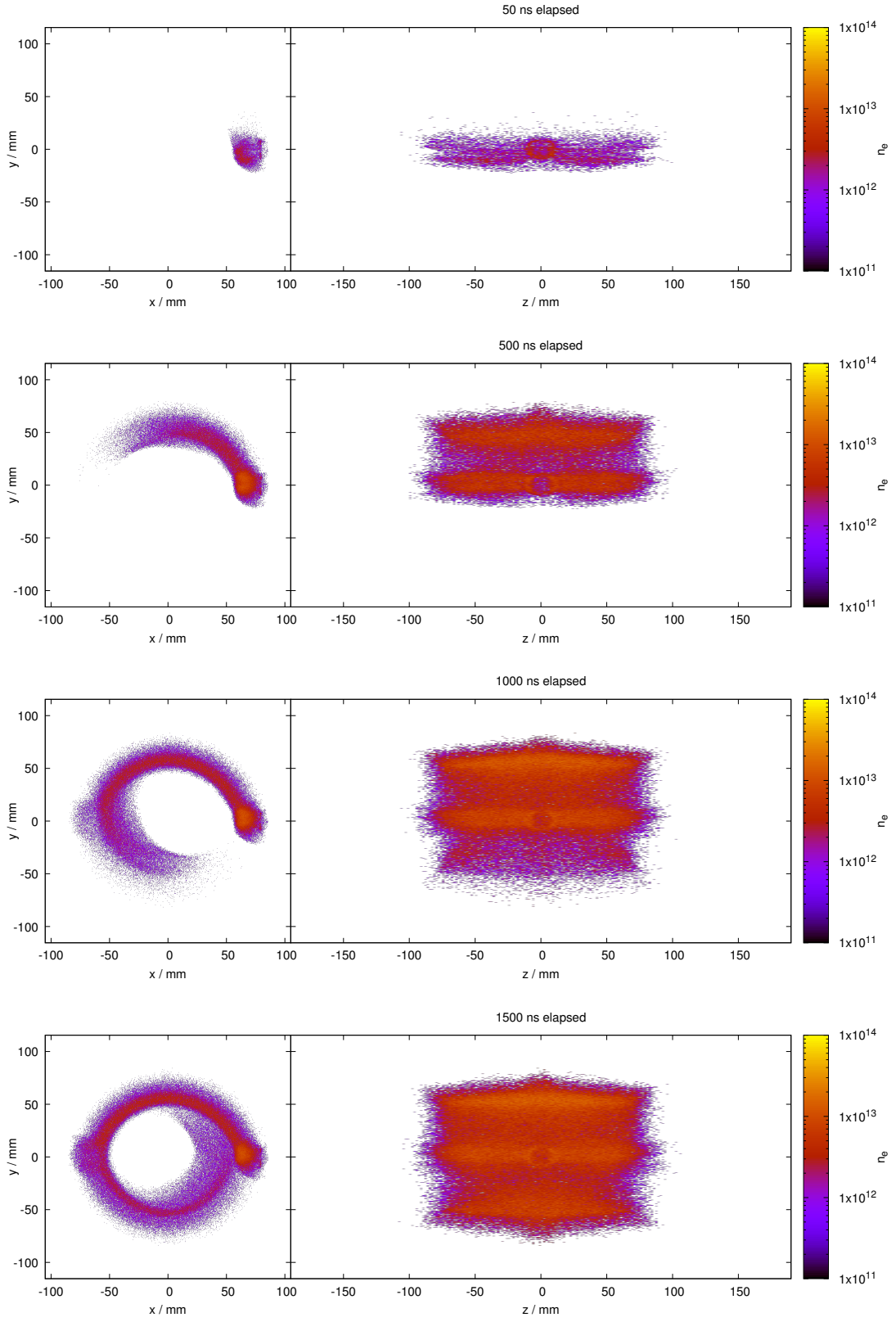

Figure 2.31: First simulation results of a long simulation. These images show the tuning phase of the system, where the toroidal elecron density is being built up. This is very similar to the simulations in figure 2.27 and 2.28. The colours represent the densit in $1/m^3$

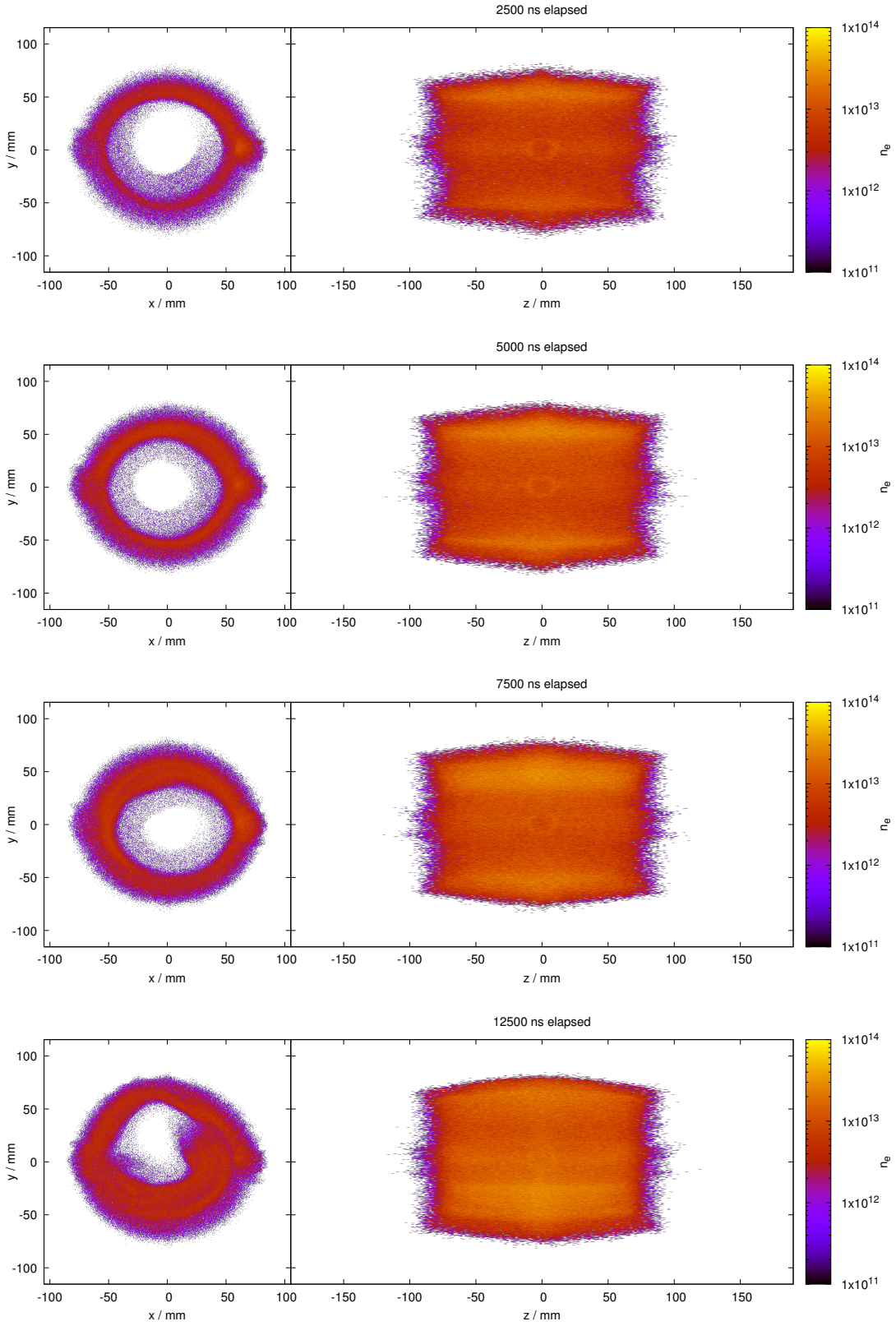

Figure 2.32: Second simulation results. In these images, the buildup of the instability is shown. First the torus becomes thicker in one region. This leads to a density wave that propagates in azimuthal direction.

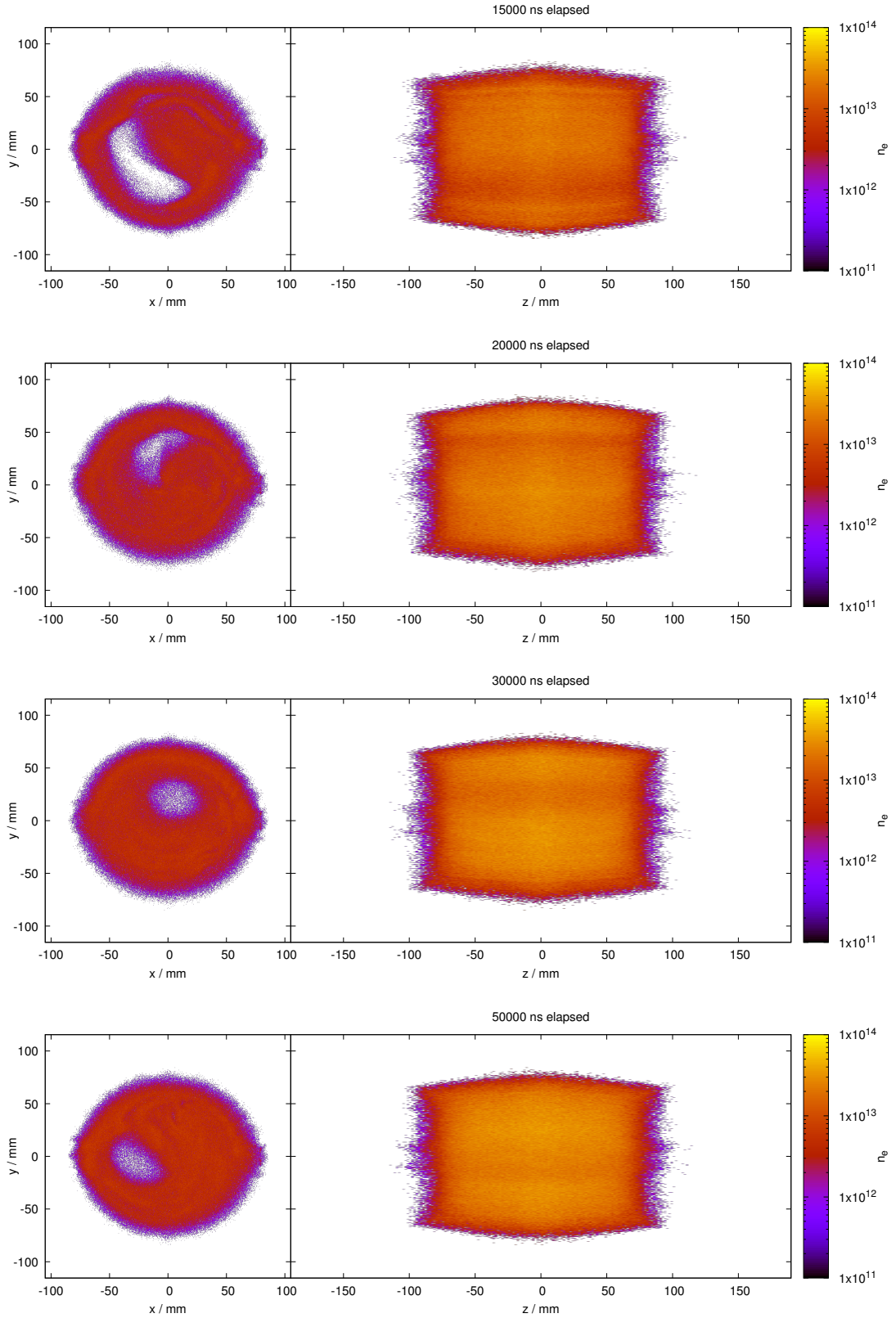

Figure 2.33: Third simulation results. After the torus-shape is dissolved by the instability, a new state is reached that appears to be stable for long times. The final state appears to be a nearly homogeneous density distribution with a hole that rotates around the symmetry axis with a frequency of approximately 1.5 MHz.

Chapter 3

Experiment

3.1 Characterisation of the electron source (at INFN Bologna)

The electron source was provided by the collaboration partners from INFN Bologna. In order to prepare the injection experiments the existing electron source was rebuilt and characterized.

Since it was decided to build the internal source design, the electron source is going to be exposed to a large transversal magnetic field. In the same way the magnetic field of a Gabor lens serves as transversal confinement, the electron beam could be deflected by the Lorentz force and the emitted electrons may get lost at the walls of the electron source.

In order to compensate for the negative effect of the transversal magnetic field, two strategies are discussed. First, a small magnetic coil close to the electron source is supposed to add a longitudinal magnetic field to the transversal one, effectively turning the magnetic field vector towards the electron beam axis. As a small sized coil with few windings of thin wire is not capable of carrying very large currents and therefore the generated magnetic field is limited, this coil is only able to compensate small transversal fields compared to the maximum fields a large Helmholtz coil structure delivers. Hence and second, the transversal field in the auxiliary coil and electron source has to be reduced. This can be achieved by adding a μ-metal shield to the source capsule. This way, the transversal field inside the source is very small. Both methods combined should ensure a working condition for the electron source in a Gabor lens environment.

As discussed before, the simulations revealed that adding an auxiliary coil in this way is not helpful, as the symmetry in the magnetic field is broken in the area of the electron source. Nevertheless, it was decided to conduct measurements with a small coil in order to verify the simulations.

During the measurements, a minimal pressure of 1.3×10^{-5} mbar was achieved. It was necessary to open the vacuum chamber several times to perform optimization in the quality of the contacts, so the maximum pumping period was limited to a few hours. Nevertheless, it was possible to achieve about 2×10^{-5} mbar after every modification. This was very close to the limit of the pumping system.

3.1.1 Auxiliary coil

The auxiliary coil is constructed with a special copper wire that provides a significant heat resistance. The manufacturer specifies the nominal current with 0.45 A. Therefore, all measurements conducted with an auxiliary coil current of 0.45 A or less can be conducted over a long time. Sometimes, 0.60 A have been applied in order to check the effects of a higher auxiliary coil field, but this state may only be used for a limited time of several minutes to prevent the wire from melting, as there is no cooling in any form applied to the coil.

The maximal field in the coil at 0.45 A was measured and yields 14 mT. Simulations of the coil predicted a maximal field of 18.28 mT. From these simulations and this measurement, it was estimated that the field at the tip of the filament is about 5.3 mT, as the filament is not in the centre of the small coil, compare figure 3.3.

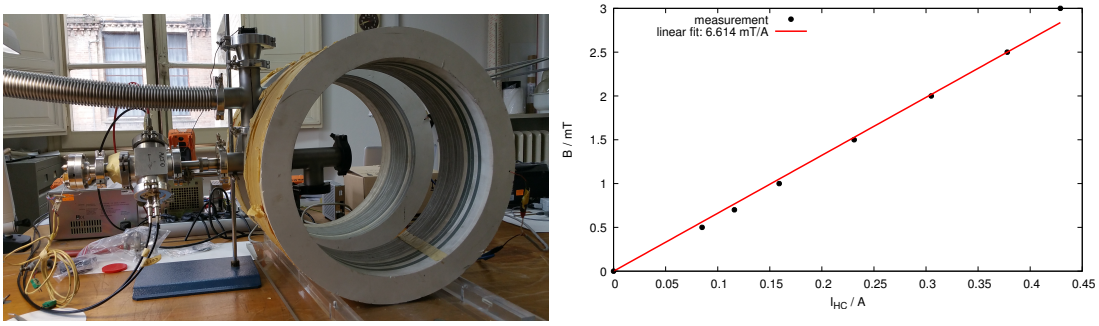

Figure 3.1: Left: Setup of the transversal field measurements in Bologna. The electron source is located inside the vacuum system inside the Helmholtz coils. Right: Calibration diagram of the Helmholtz coils.

Figure 3.2: Left: old aperture of 4 mm diameter. The contamination on the surface is silver paint that was used as adhesive in order to prevent the coil holder from turning during the assembly of the source. Right: the widened aperture of 8 mm. Here, the filament and the grid have already been assembled.

3.1.2 Structure of the source

The electron source consists of a heated filament that is used as an electron supplier. The filament is put on a negative potential, or **bias**, up to 200 V. The electrons are extracted towards a grid that is grounded. Afterwards, they propagate through the internal coil that acts as a focusing solenoid. After a short drift of about 2 mm after the front aperture of the auxiliary coil, the electrons are captured by a pickup that is polarized by approximately 18 V positive potential against ground. The current that is captured by the pickup is measured. Compare figure 3.3 for a circuit schematic and a sketch of the electron source. Note that in the first experiments the filament chamber wall was composed of macor. The electron source can be introduced into a magnetic field created by two Helmholtz coils which can be applied transversal as shown in figure 3.1. The maximal field inside the Helmholtz coils was measured using a Hall probe with respect to the current that is applied to the system. Increasing the current by 1 A, the field increases by 6.614 mT.

Once the electrons leave the aperture of the electron source, they are strongly influenced by the transversal magnetic field. They start moving on circular orbits, defined by the Lamor radius in equation (1.17). If the Lamor radius is larger than 2 mm, electrons that may be directed back on the electron source are captured by the pickup instead. While a transversal magnetic field is present, a higher pickup current than the extracted current is expected.

The current that is emitted by the source can be measured not only by using the pickup, but also by measuring the bias current and estimating the efficiency at the given parameters. If the filament is heated, but the extraction potential is zero, there is a residual bias current, because the filament is emitting electrons and some are leaving the source through the grid or are collected by the chamber walls. The resistance of a new filament is approximately $(0.8 \pm 0.1)\,\Omega$, depending on the individual filament.

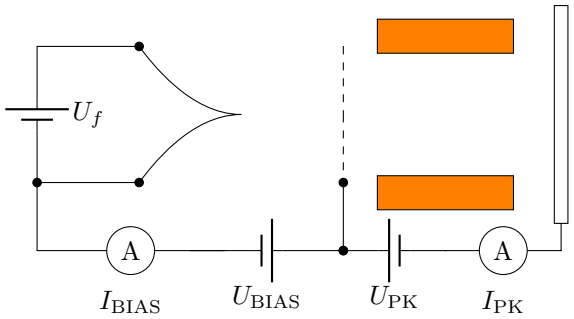

Figure 3.3: Setup of the electron source with the auxiliary coil and the pickup.

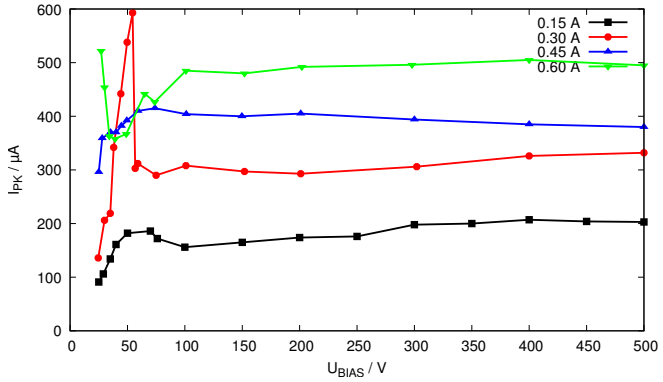

Figure 3.4: Finding optima in the pickup current by varying the bias voltage under different intensities of the internal coil magnetic field. No external magnetic field is applied to the system.

In this context, "bias" describes the fact that a component is on a different potential than the rest of a given structure. Hence, "bias voltage" stands for the potential difference between component and structure and "bias current" is the current necessary to keep the potential difference.

3.1.3 Aperture

First measurements yielded a maximal current of 225 µA at $U_{\mathrm{BIAS}} = 31\,\mathrm{V}$. In this measurement, the auxiliary coil was installed but the magnetic field $B = 9.75\,\mathrm{mT}$ was delivered by a large pair of Helmholtz coils. This field is equivalent to applying 0.45 A to the auxiliary coil. In order to be more flexible in the injection measurements later on, the main priority is to increase the current delivered by the electron source. Therefore it was decided that roughly 1 mA should be achieved.

Hence, it was decided to widen the aperture of the source, compare figure 3.2. Before the alteration, the setup had an aperture of 4 mm in diameter, which was widened to 8 mm. This was supposed to give a factor of four in the total area that can be used for emission. As the current density might not be constant on this surface, we may expect at least a factor of two in pickup current increase. Increasing the aperture only leads to an increase in current if the filament is able to deliver sufficient electrons. If the electron source is operated in thermionic emission, that is when the current is limited by the thermal electron emission from the filament, increasing the aperture of the electron source will lead to a quick depletion of the electrons inside the filament chamber. The filament used with this electron source is operated in the space charge limit if the heating current is 2.5 A or higher, compare figure 3.18, because in this case, increasing the bias voltage leads to a higher current. Hence, the electrons in the filament chamber are not depleted by increasing the aperture and the extracted current is increased.

Comparing the measurement for 0.45 A in the auxiliary coil in figure 3.4, the change in aperture did improve the current extracted from the electron source.

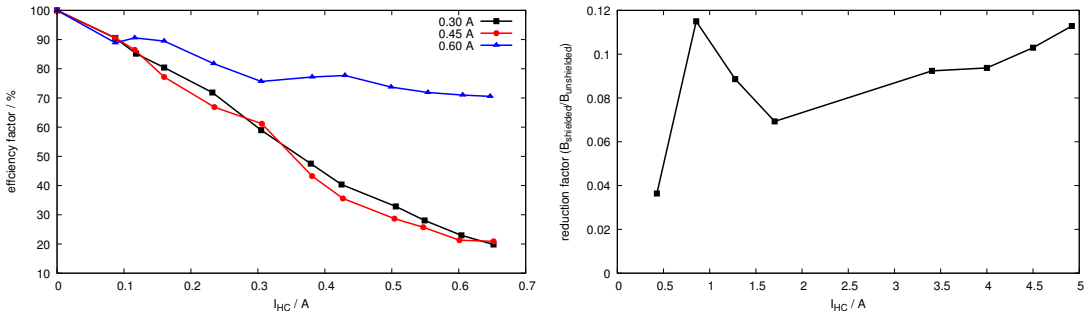

Figure 3.5: Left: Measurement of the transversal magnetic field impact on source performance. During the measurement, the heating of the filament was adjusted so that 115 µA were measured in the pickup without the transversal field. Afterwards, the current was measured with a transversal field. Right: Measurement of the reduction factor of a given piece of μ-metal with respect to the applied magnetic field.

3.1.4 Characterisation measurements

In the first measurements, the bias voltage was varied in order to find maxima in the pickup current. Furthermore, the current in the auxiliary coil was set to four different values. The results are shown in figure 3.4. The heating current was held constant over time by adjusting the voltage of the filament heating in order to compensate for the change in resistance due to heating. As a result, the power changed slightly over time, with different levels for each bias voltage. Furthermore, the current in the pickup was not constant in time, probably because the source was not operated in a thermal equilibrium. This was necessary in order to keep the temperature of the housing and the wires low, so that the soldered connections would not de-solder due to the heat.

The curves show unexpected behaviour at small voltages and a nearly constant current at larger voltages. In theory, all curves should show similar characteristics. Instead, some are increasing, others are decreasing. At low voltages, there is sometimes a maximum or minimum. Therefore, this measurement is probably influenced by effects that are not desired. The first measurement was conducted with 0.15 A current in the internal coil, the last measurement used 0.60 A in the internal coil. This measurement was repeated some time later. For low bias voltages, highly unusual behaviour was observed. For larger bias voltages, saturation was expected. However, the measurement with 0.45 A internal coil current showed a decreasing trend.

It is essential to check if the internal coil is able to compensate for the disadvantageous effect of the transversal magnetic field in a Gabor lens. Therefore, a transversal magnetic field was applied using two Helmholtz coils and observed the current in the pickup with and without transversal field.

The efficiency of the electron source was measured with respect to a transversal magnetic field for different settings of the auxiliary coil. The efficiency was calculated by dividing the current with transversal field by the current without a transversal field multiplied by 100 in order to yield a percentage. In this way, the effect of a temporal variation of the pickup current was compensated by normalizing the measurements. The result are depicted in figure 3.5. If the auxiliary coil is operated at 0.6 A, the efficiency loss due to the transversal magnetic field can be reduced. Since these measurements were taken without the magnetic shield, larger magnetic fields can be tolerated.

In this setup, it is possible to simulate the effect of a μ-metal shielding, as the transversal magnetic field may be decreased. Furthermore, a chassis made of μ-metal was introduced into the magnetic field and the dampening factor η was measured. Hence, the dampening factor of the shield in the final configuration can be estimated. η is defined as the ratio of the magnetic field shielded by the μ-metal shield and the unshielded magnetic field.

$$\eta = \frac{B_{\text{shielded}}}{B_{\text{unshielded}}} \tag{3.1}$$

The results are shown in figure 3.5. A reduction factor of around 0.1 can be achieved almost

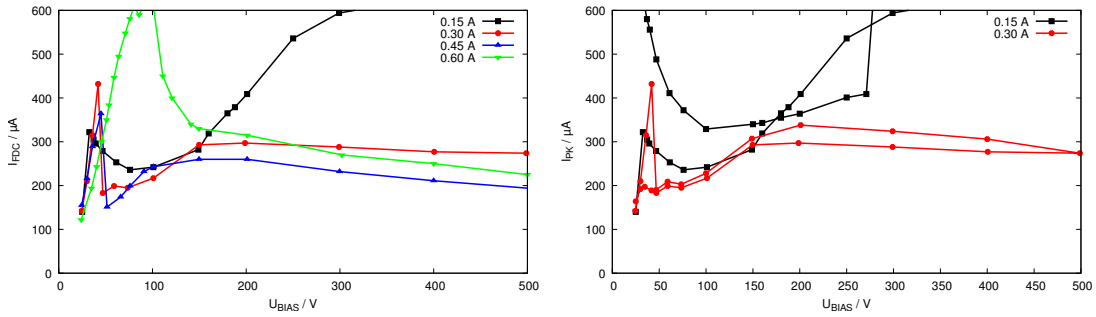

Figure 3.6: Left: Repeat pickup current measurement. Filament: 2.412 V, 2.612 A. Right: Hysteresis effects in the repeated measurement. Aperture of the electron source extraction grid: 8 mm.

independent of the magnetic field. As a result, a transversal field almost 10 times stronger than measured here can be tolerated in a Gabor lens environment. Additionally, the measurements with lower magnetic field can be compared to setups with a high magnetic field and shielding of the electron source, so it can be concluded which magnetic field corresponds to a point in figure 3.5.

Hence, if 0.6 A are applied to the auxiliary coil and a transversal magnetic field of approximately 4 mT is present, the electron source retains 70 % extraction efficiency. Considering the dampening effect of the μ-metal shielding as discussed before, the tolerable transversal magnetic field increases to 40 mT.

As mentioned before, fluctuations in the pickup current in terms of a tendency to increase or decrease over time were observed. Therefore, the measurement of the pickup current with respect to the bias voltage was repeated. Furthermore, the sequence of the measurements was inverted, starting with 0.6 A internal coil current and ending on 0.15 A. The order of these measurements made a difference, as the results of the repeated measurement shown in figure 3.6 differ from the previous results shown in figure 3.4. Both measurements were conducted two days apart.

Comparing the results, unexpected behaviour in the regime smaller than 150 V can be observed. The pickup current now falls with rising bias in almost every measurement, unlike before. The plot for 0.15 A, shows the most differences. Maybe this is due to the fact that the 0.15 A measurement was the first one in the initial measurement sequence shown in figure 3.4 and the last one during the repetition measurement shown in figure 3.6, left. Therefore, the properties of the filament changed between the measurements and the characteristics of the filament also change in the scope of a measurement session during the heating process. These effects can also be observed in figure 3.6. Here, the measurements of 0.15 A and 0.30 A coil current have been conduced by first increasing the bias voltage up to 500 V and decreasing to zero afterwards. In the case of 0.30 A, a very small hysteresis effect can be observed, which may be explained by the change in filament conditions due to continuous heating. A more significant hysteresis effect can be observed for 0.15 A. Concluding the measurements in Bologna several problems have been observed. First, the extracted current is small. In this case, the pickup was located very close to the aperture of the electron source, so the extracted current is measured under optimal conditions. In a different setup, such as the Gabor lens configuration, probably a smaller current is extracted than is measured in this preliminary test. Furthermore, applying a transversal magnetic field decreases the performance of the electron source further. Therefore, some modifications of the electron source system were introduced:

- The material of the filament chamber wall is changed from a ceramic insulator to aluminium and put on a negative potential larger than the bias potential. This was done in order to collect electrons that would hit the chamber wall instead of being emitted by the source. The inner cylinder that forms the filament chamber wall is called gate ring.

- Aluminium melts at 660.2 °C, while the filament is heated to a temperature well above 1000 °C. Therefore, the aluminium gate ring needs to be monitored in terms of temperature, which is provided by a thermocouple that is inserted into a feedthrough of the gate ring.

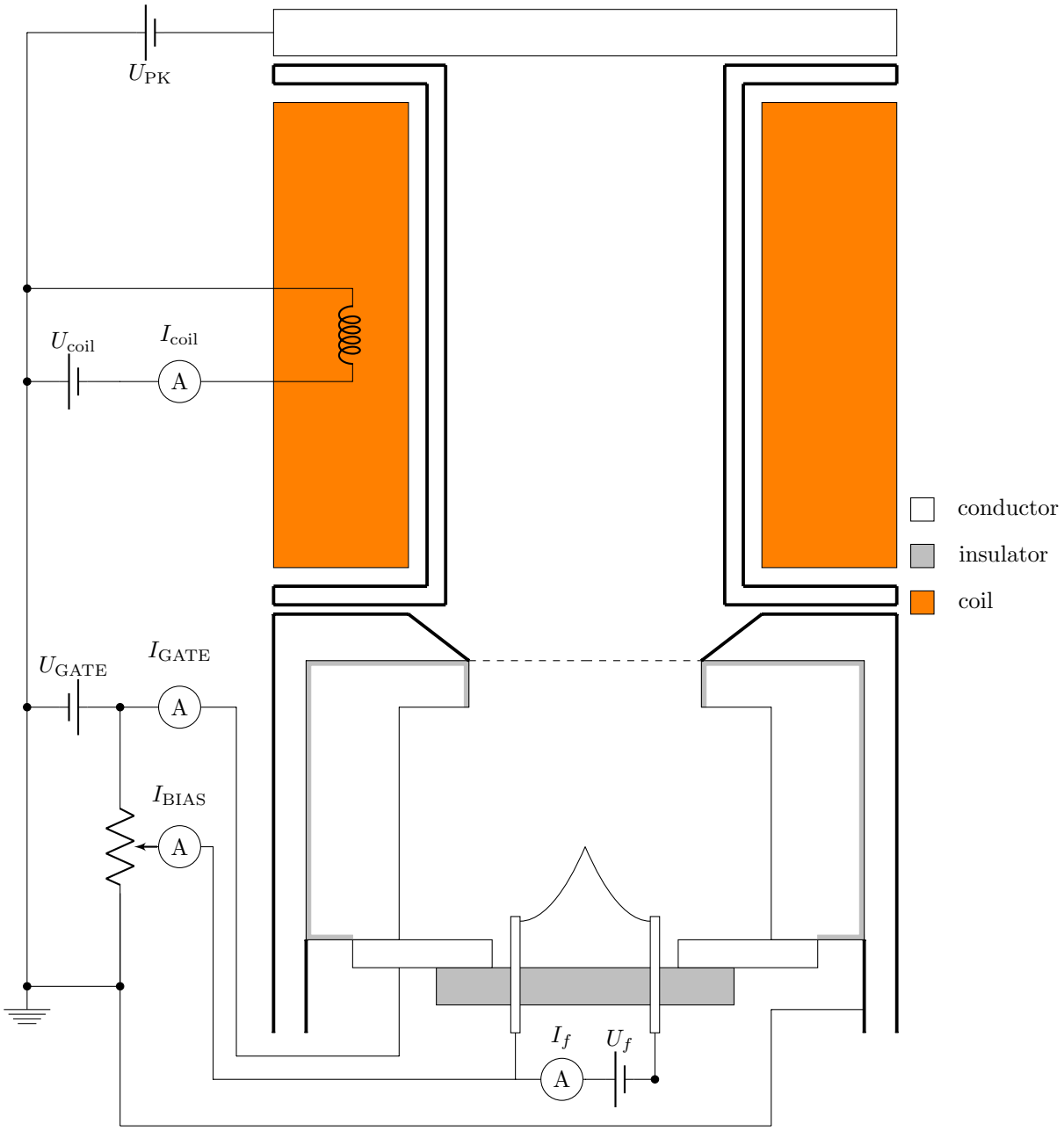

Figure 3.7: Setup of the electron source using the gate ring. A potentiometer is used to fix the ratio between the gate and bias voltages. So one power supply could deliver both voltages at the same time. For convenience, some measurements were taken using a second power supply to adjust bias and gate voltage separately.

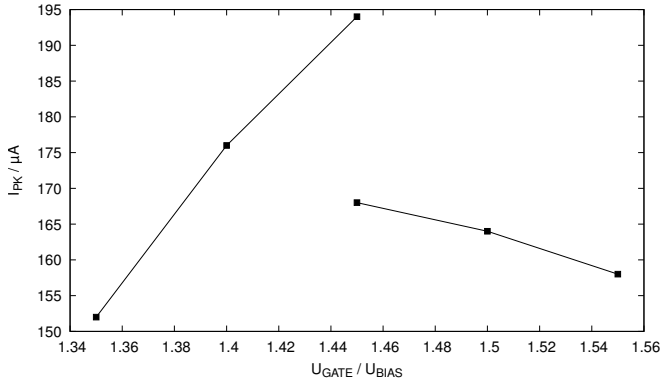

Figure 3.8: Maximizing the pickup current with respect to the ratio of gate and bias voltage. The bias voltage was fixed at 100 V.

- The external μ-metal shield is completed and added to the electron source. In order to attach the shield, the chassis of the source is extended.
- Mounting the small coil onto the electron source used to be very challenging, since it is secured by a cap that is screwed onto the electron source casing. The small coil used to rotate during the mounting process, which led to the connectors being misaligned. Bolts are added to the coil holder and small holes are drilled into the front of the electron source in order to fix the coil in place.

Simulations conducted by INFN researchers [20] have shown that an optimal ratio between gate and bias voltage that optimizes the extracted current can be found. This ratio is independent of the absolute value of the bias voltage. Furthermore, the gate voltage should always be larger than the bias voltage in order to prevent electrons from reaching the filament chamber wall. The available power supply delivered up to 200 V for the gate ring. A potentiometer was used to deliver a lower bias voltage. Hence, only one power supply is needed and the ratio between gate and bias voltage is fixed while manipulating the gate or bias voltage. The circuit schematics of the measurement setup are shown in figure 3.7.

In order to investigate the performance of the electron source, the current in the pickup for several bias voltages was measured and by varying the gate voltage, a maximum for each given bias voltage was found. First, it was investigated whether there is a ratio of gate and bias voltage that maximizes the current in the pickup independent of the bias voltage. The results shown in figure 3.8 suggest that the current is maximal at a ratio of gate and bias voltage between 1.45 and 1.46. In order to prepare the injection measurements, it is necessary to characterise the electron source so that the optimal operation parameters are known. As the source will be installed in a transversal magnetic field, it is required to measure these parameters with a transversal field present. Of particular interest in these measurements are sets of parameters that maximize the current that can be extracted out of the source. In order to get a qualitatively good overview of the performance, the source will be tested at several transversal magnetic fields and the position of the μ-metal shield will be varied. During these measurements, not only the current in the pickup is recorded, but also the efficiency of the source and the ratio that delivers the maximal current.

As a first step, the magnetic field has been varied and the current in the pickup has been recorded for various bias voltages in the range between 30 and 150 V. The results are shown in figure 3.9. Apparently, there is a maximum in the extracted current in the range of 100 V to 130 V for any transversal magnetic field in the range of 100 to 15 mT. This maximum also appears if the efficiency of the electron source is plotted, refer figure 3.9b. Therefore, the electron source should be used in this configuration. No clear maximum can be observed in the ratio that delivers a maximal current. It has to be considered that the grid has a transparency of only 64 %, which is therefore the theoretical maximum of the efficiency. Nevertheless, the ratio spreads on a small range between 1.3 and 1.44 and the optimal ratio does not show a sharp maximum in the pickup current, but a plateau. Therefore, any value between 1.3 and 1.44 should suffice in

order to maximize the pickup current.

Considering the ratio between gate and bias voltage, it was postulated before that there is a given ratio for all voltages and magnetic fields, because the ratio should only depend on the geometry. The results of figure 3.8 suggest that there is indeed one optimal ratio in the range between 1.44 to 1.48. Measurements of the optimal ratio at different bias voltages show that the ratio only varies in a rather small interval, compare figure 3.9c. Therefore, it can be concluded that the ratio is not perfectly constant, but the measurements suggest that a very small range of the ratio will contain the maximum current with respect to bias and the transversal magnetic field.

In order to characterise the electron source with respect to the position of the μ-metal shielding tube, the transversal magnetic field has been fixed to 12.5 mT and three positions of the shield have been compared in terms of absolute current in the pickup, the efficiency of the extraction system and the ratio between gate and bias voltage. The position of the shield is defined by the distance between the front of the electron source and the front of the shielding tube. So at a position of 7 mm, the shield emerges 7 mm from the front of the electron source. The results are shown in figure 3.10.

Looking at the top image, there is still a maximum for any configuration of the shielding tube in the pickup current in the range between 100 and 130 V. Furthermore, using the 12 mm position yields the largest current measured in the pickup. Again, the efficiency in figure 3.10b, is rather high in this range of the bias voltage.

The measurement of the optimal ratio between gate and bias voltage shown in figure 3.10c, yields a rather narrow range of the ratio between 1.3 and 1.4 that will be suitable for bias voltages in the regime of 100 to 130 V. Changing the position of the shield does not impact the optimal ratio in this regime. If lower bias voltages are to be considered, the position of the shield is more important. Nevertheless, the optimal ratio was not unique. Choosing a ratio close to the one plotted yielded again a very similar current in the pickup. As a conclusion, a ratio close to these plotted here should suffice to yield a optimal current of the electron source.

Due to the modifications, the characteristics of the electron source changed. For a bias current between 100 V and 130 V and a ratio between 1.3 and 1.44, both the current extracted from the electron source and the efficiency of current extraction are maximal. This is true for multiple magnetic fields between 10 mT and 15 mT. Therefore, the electron source is ready to be used in an experiment. In a last measurement, the current that could be extracted from the electron source with and without auxiliary coil attached was measured and is compared in figure 3.11. Here, the pickup current is first very similar for both cases, with and without coil. At voltages larger than 130 V bias voltage, both configurations show a major difference. The structure with the auxiliary coil shows a maximum in the extracted current, while the measurement without the coil does not show any maximum in the range of U_{BIAS} up to 200 V.

Solenoids operating at a given magnetic field allow good transmission of charged particles of a given impulse. If the impulse is changed, transmission decreases, because the focal length depends on the impulse of the beam particles, compare [21]. Therefore, it is necessary to adjust the focussing strength of the solenoid if the beam energy is changed. This was not done in this measurement, which is why the pickup current shows a maximum at $U_{\mathrm{BIAS}} = 130\,\mathrm{V}$ while the auxiliary coil is used. Furthermore, the solenoid channel acts as a loss surface for the electron beam. Hence, additional losses could explain the lower transmission while using the auxiliary coil. In addition, the pickup used for measuring the current was not positioned equally for both measurements. Therefore, the current measured after transmission through the auxiliary coil is expected to be much lower than the current measured by placing the pickup directly in front of the electron source. Considering the position of the pickup, it is remarkable that using the auxiliary coil, a current comparable to the measurement without coil can be detected.

It was decided to conduct the measurements in the Gabor lens configuration without the auxiliary coil for a first test, because this eliminates an additional variable in the system, simulations indicate that using the coil generates local disturbances in the magnetic field that may lead to an asymmetric electron distribution and finally, the electrons are expected to distribute in the lens volume. Therefore, a high electron beam intensity was expected to be more important than conducting measurements with a focussed electron beam at the cost of additional losses in the electron source.

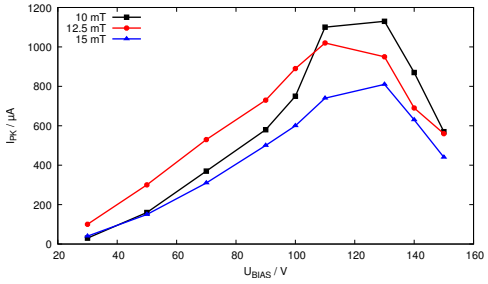

(a) Pickup current

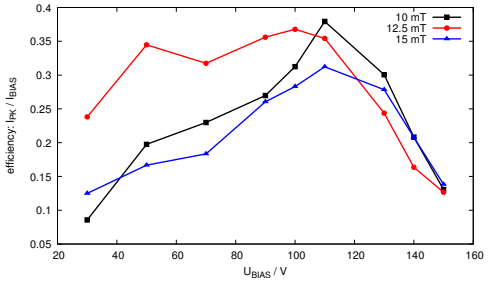

(b) Efficiency

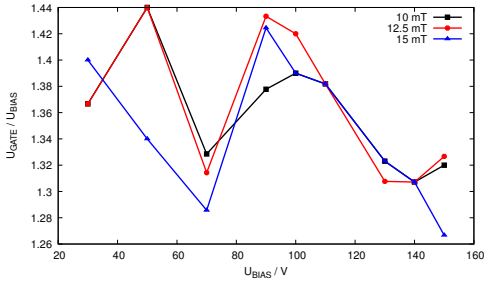

(c) Ratio

Figure 3.9: In these measurements, the shield was spaced 2 mm from the front of the electron source. (a): The gate voltage has been adjusted for each measurement to achieve the maximum current. (b): The efficiency is plotted. We see a maximum between 100 V and 130 V for any magnetic field. (c): The ratio that yields the maximal current at a certain bias voltage is plotted. The ratio oscillates in a very small interval between 1.3 and 1.44, so choosing any value in this regime should suffice in a further experiment.

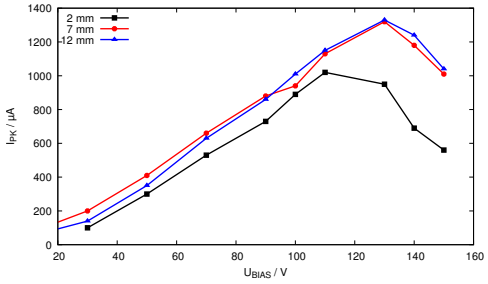

(a) Pickup current

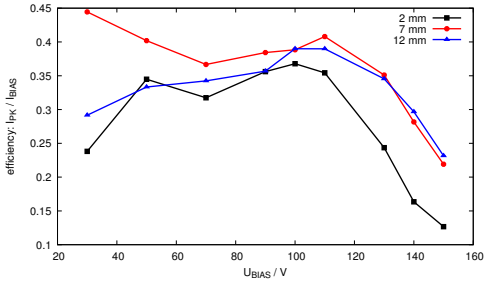

(b) Efficiency

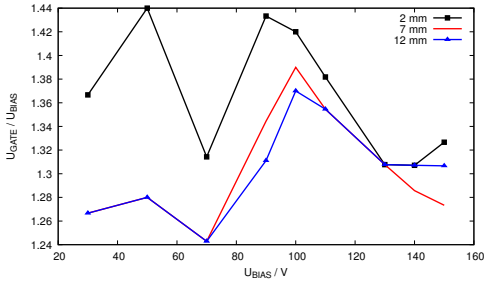

(c) Ratio

Figure 3.10: A similar setup to the measurement shown in figure 3.9, but the magnetic field has been fixed to 12.5 mT and the position of the shielding tube has been varied. (a): The current in the pickup can be maximized at the 12 mm position of the shield. (b): Again, a high efficiency in the range between 100 and 130 V is observed. Furthermore, the efficiency does not depend on the position of the shield in a wide range. (c): The ratio is not constant, but limited to a small range.

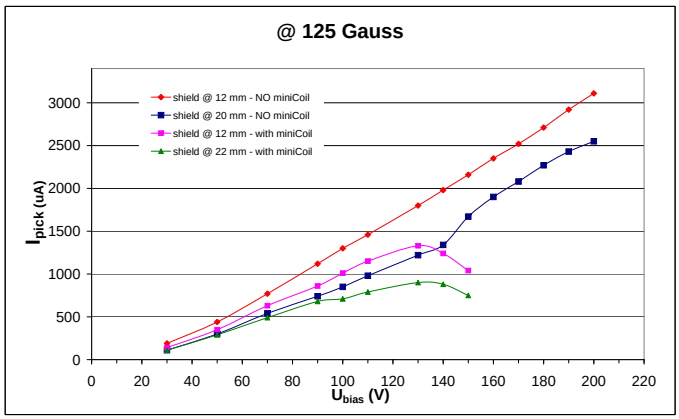

Figure 3.11: Effect of the auxiliary (mini) coil on the characteristics of the electron source. Measured by [20].

3.2 Setup of the injection measurement, characterisation of the electron source and ingition measurements without electron source

3.2.1 Setup of the measurement test stand

In order to install an electron source to the Gabor lens test stand, the anode had to be redesigned. Four ports have been welded into a cylinder of inner radius 88.5 mm. The electron source is mounted to a horizontal port, while a small pickup is mounted to the other horizontal port across from the electron source. The upper port contains a small window, so that the position of the electron source can be observed with respect to the inner anode surface. The bottom port is sealed and used for the high-voltage connection. The setup is depicted in figure 3.12.

In order to characterise the plasma inside the Gabor lens, three diagnostic tools are available at IAP. First, a CCD camera can take images of light emitted by the plasma. In this way, a visual representation of the plasma state can be obtained and can be characterised [4]. Second, a Faraday cup (FDC) is placed longitudinally in front of the Gabor lens plasma. An oscilloscope is used to read the current on the cup over time. Hence, periodical oscillations in the plasma that manipulate the ion current emitted by the Gabor lens can be observed and detected. It has been shown that fast oscillations with a large amplitude correspond to an instability, while a rather constant current usually indicates a stable distribution of electrons [4].

Finally, a momentum spectrometer is measuring the energy of the ions that are extracted from the plasma by the anode potential, compare section 1.2.8. A 90° dipole magnet bends the ion beam into a Faraday cup, allowing for current measures with respect to the magnetic field. As the magnetic field corresponds to the momentum of the ions that are able to pass the curvature, it is possible to find the ion energy that is present with the highest intensity, because the mass of the ions is known. As mentioned before, this energy is generally smaller than the anode potential and can be used to calculate the mean density confined in the Gabor lens.

The power supplies that are not part of the electron source system and the diagnostics with the exception of the CCD camera are connected to a control system running a version of MNDACS [22], a digital control software written in Java. Using MNDACS, the measurement process can be fully automated. During the measurements with the electron source, the control software simplifies the usage of the momentum spectrometer.

Due to a special vacuum flange, the electron source can be moved longitudinally with respect to the electron beam axis. The measurement conducted in figure 3.30 indicates that the position of the electron source influences the potential distribution inside the Gabor lens and therefore

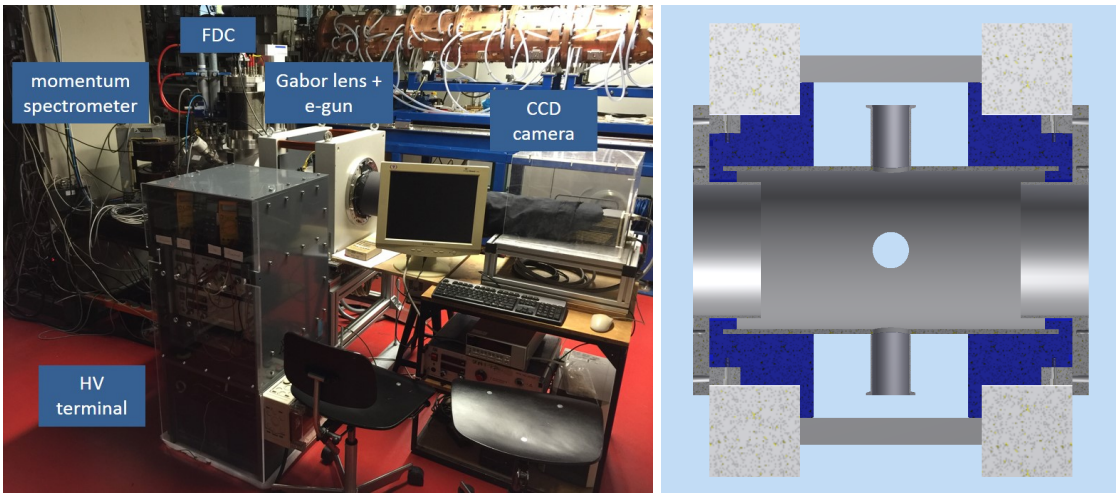

Figure 3.12: Left: Gabor lens test bench at IAP with the diagnostic equipment. Right: Cross section of the new four port design of the Gabor lens. Blue: insulator, gray: Helmholtz coils, dark gray: anode and ground electrodes.

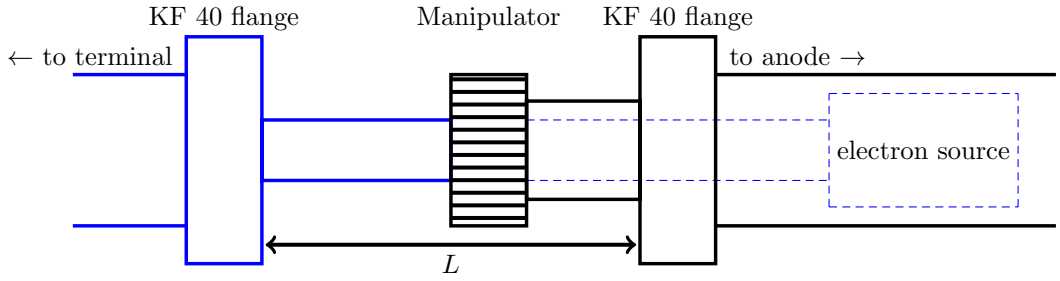

Figure 3.13: Sketch of the position parameter of the electron soruce. The manipulator is used to move the electron source with respect to the anode by moving the vacuum system attached to the left KF 40 flange. The electron source is indicated by the dashed lines. Parts moving with respect to the fixed anode are drawn in blue.

the plasma properties. Hence, a length parameter L is introduced defining the position of the electron source with respect to a flange illustrated in figure 3.13. If $L = 97\,\text{mm}$ is chosen, the electron source is planar to the anode surface. This leads to the following conversion formula from L to the radius of the tip of the electron source r_g in polar coordinates:

$$r_g = L - 8.5\,\text{mm} \tag{3.2}$$

At $L = 40\,\text{mm}$, the electron source is positioned as close to the centre of the anode as possible. The distance from the front of the electron source to the centre of the Gabor lens at this position is approximately 31.5 mm.

The operation of the electron source on a potential of up to 8 kV is enabled by the use of a high-voltage terminal illustrated in figure 3.14. In this setup, an insulating transformer is used in order to transfer power to the power supplies in high-voltage terminal. It offers a three phase electric power connector and a standard 230 V power outlet. If the electron source is on the same potential as the anode of the Gabor lens, the anode power supply can be used to provide high-voltage for the electron source as well by connecting the chassis of the electron source to the anode. In a second operation mode, the electron source is insulated against the anode and a second high-voltage power supply is used to provide a potential to the electron source system. This circuit schematic is independent of the operation modes discussed above. On the high-voltage side of the insulating transformer, there is no difference between reference ground and neutral conductor, as both are connected in the transformer and the power outlet. The potential of this terminal is limited by the dielectric strength of the insulating transformer. As a result, the maximum voltage may not exceed 8 kV.

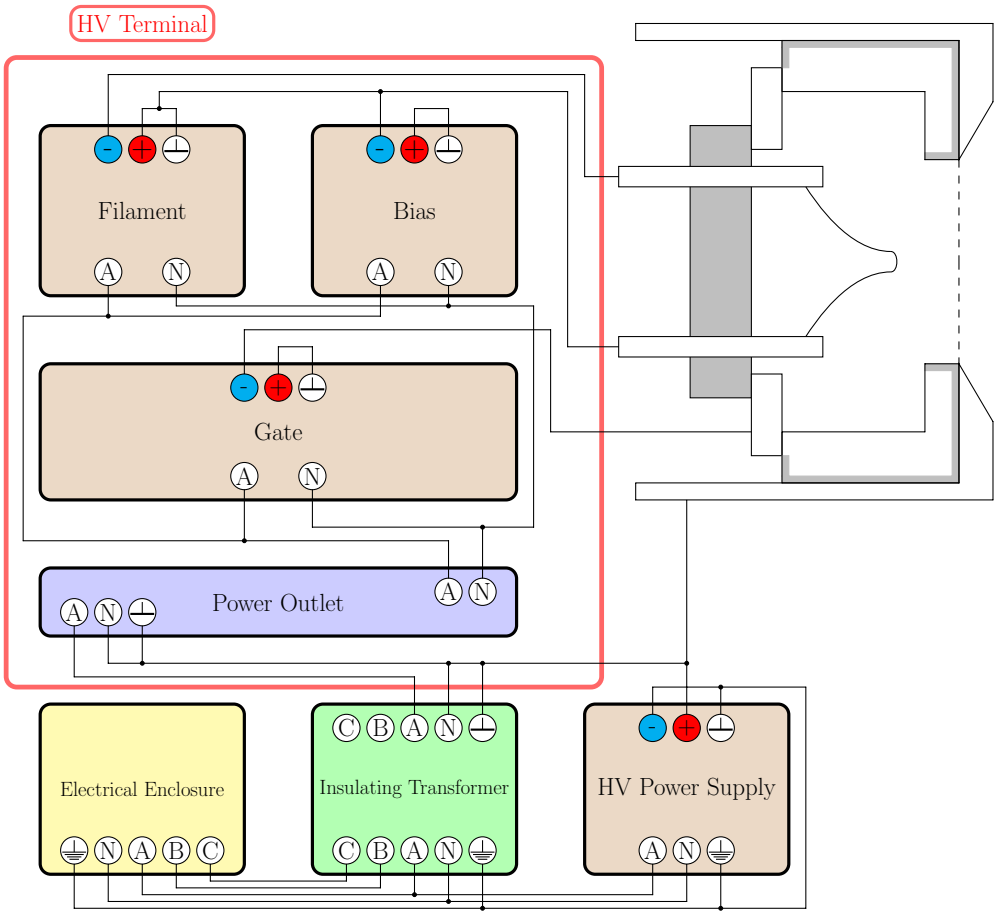

Figure 3.14: Sketch of the high-voltage terminal with the electron source.

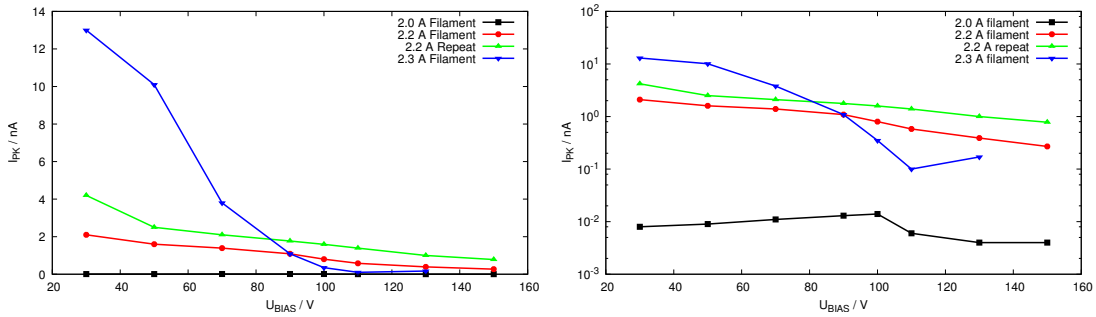

Figure 3.15: Measurement of the current on the pickup vs. the bias voltage. Both images show the same data, but in different scales.

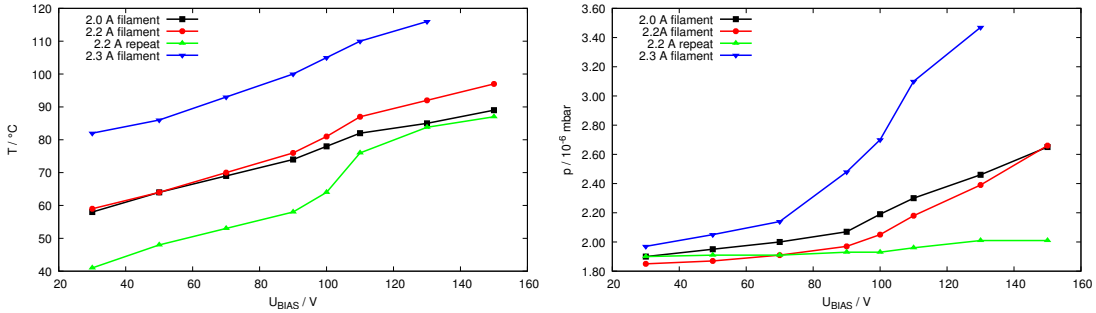

Figure 3.16: Left: Temperature during the measurements. Right: Pressure during the measurements. As the measurement utilizing 2.2 A filament current has been repeated we can compare the red(earlier) and green(later) curve. Here we seen that the pressure increases less during the revision of the 2.2 A measurement than in the original data set shown in red. Therefore we can conclude that degassings significantly decline after several minutes of operation.

3.2.2 Steady state measurements

Preliminary measurements with the electron source system have been conducted. The heating of the filament has been kept constant through each measurement. Furthermore, the ratio between gate and bias had been fixed to 1.4 for the first measurements. Afterwards, the measurements have been repeated with a ratio of 1.28, since measurements in Bologna revealed that a ratio of 1.28 is more appropriate for using the electron source without the auxiliary coil [20]. Furthermore, measurements in Bologna suggested that a higher current is achievable if the coil is not used, compare 3.11. In order to evaluate the effect of changing the ratio, the current on the pickup has been recorded with a ratio of 1.28 at the same heating settings that were used with a ratio of 1.4 and the results are compared to the previous measurements in figure 3.17a. These preliminary measurements were performed at $L = 97\,\mathrm{mm}$.

Apart from these changes, the data in all of these measurements was taken in the same way. The bias voltage has always been increased from 30 V to 150 V with the gate voltage increased respectively. Thus, the U_{BIAS}-axis can be interpreted as a non-linear time axis as well. The currents were not measured with high precision in these preliminary experiments, but for the future the experimental setup may be extended to enable a high precision measurement of bias and gate current. Furthermore, the emitting surface of the electron source was approximately in 12 cm distance to the circular pickup with a diameter of roughly 1 cm, so it is only possible to measure a very small fraction of the divergent electron beam, compare 3.27. As the electron source and the pickup may be slightly misaligned, this effect may be increased further. In order to measure the current in the pickup, a picoamperemeter is used.

Considering figure 3.15, we can see that the current is decreasing with the bias. This is unexpected and my be due to a general decreasing current over time during these measurements. Maybe the current decreased faster than the bias and gate voltages were changed, so the increase in current by increasing bias is too small to be visible. This could be explained by the generally larger temperature (compare figure 3.16) of the electron source during the last two measurements. Comparing figure 3.15 (right), we can see that the first measurement with 2 A shows the expected behaviour.

After these measurements, it was noticed that the anode and pickup were floating and therefore they were charged slowly by the electron beam. As the current from the electron source was measured between pickup and anode, this measurement was influenced by the charge accumulation on the anode and pickup. With increasing accumulated charge, electrons were repelled from anode and pickup, thus decreasing the amount of electrons that were detected by the pickup. Therefore, the measurement with 2.2 A was repeated with the anode grounded. Compare the green measurement in figures 3.15 and 3.16. It is visible that grounding the anode did not change the overall behaviour of the current but increased the measured current on the pickup with respect to bias. Furthermore, the pressure increase shown in figure 3.16 during the measurement was much lower than before. So it could be concluded that these two effects are due to the improving conditioning of the filament over time.

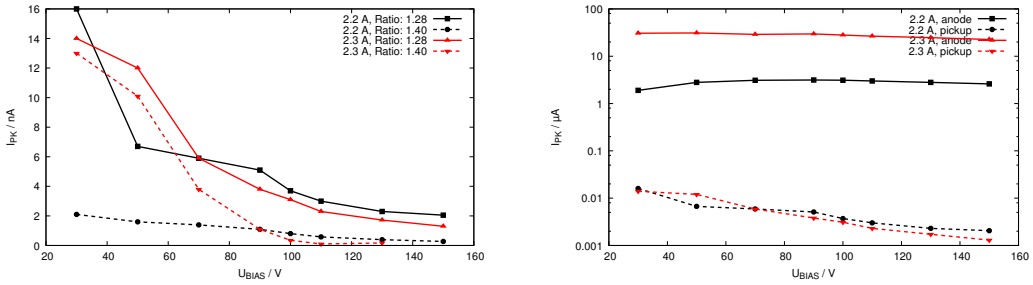

(a) Comparison ratio

(b) Comparison anode pickup

Figure 3.17: Comparison between a ratio of 1.4 and 1.28. The latter is expected to be the optimal case for the source without the auxiliary coil attached. In the case of 2.2 A and 2.3 A heating current, using the ratio of 1.28 outperforms the old setting. The measured currents are comparably low, since a small pickup several cm away from the source was used. Furthermore, the current measured on the anode is compared to the current measured on the designated pickup.

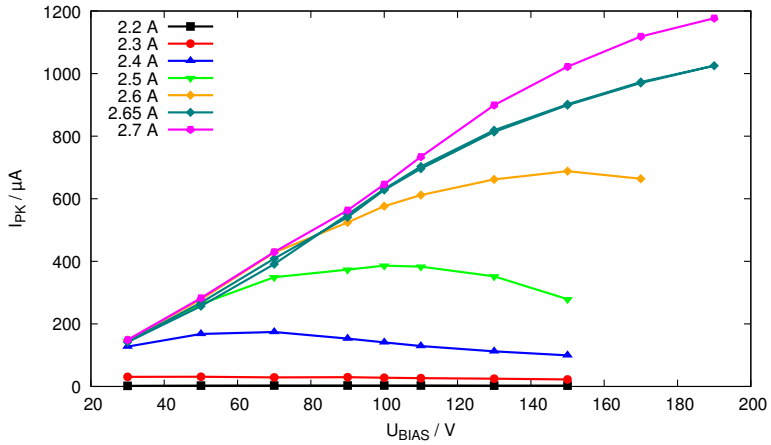

Figure 3.18: Current measured by using the anode as pickup. During these measurements, the heating current of the filament was increased from 2.2 A to 2.7 A. By increasing the heating current, the maximum current measured by the pickup is increasing, while the position of the maximum is shifting towards larger bias values.

As the currents measured by the pickup are very low, the complete anode has been connected to the pickup and thus both can be used as a singe large pickup. In order to implement this modification, the anode power supply has to be disconnected so that a single well-defined connection from anode to ground is used to measure the current. Using this configuration, the current measured by pickup and anode increased dramatically compared to the current measured by the pickup only. The current on the anode coupled with the pickup has been recorded with varying heating currents and the results are shown in figure 3.18. Using the anode as a pickup increases the measured current significantly, compare figure 3.17b.

3.2.3 Time dependent measurements

A drift in the pickup current over time has been observed during previous measurements. One explanation for this feature could be that the electron source was not operated in a thermal equilibrium due to the temperature limit. As the filament reaches temperatures well above 1000 °C [20], it is possible for the aluminium gate ring to melt, destroying the electron source. The melting point of aluminium is at 660.3 °C. Furthermore, the insulating alumina layer might be damaged at temperatures above approximately 200 °C. Therefore, the temperature of the system is limited and has to be monitored. In addition, the electron source has to enter a

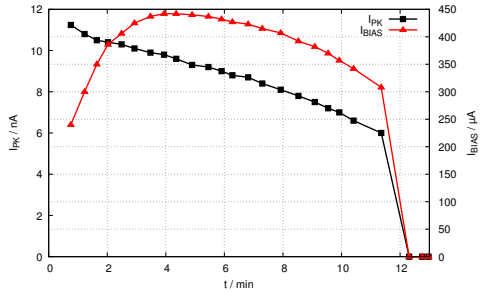

(a) Currents

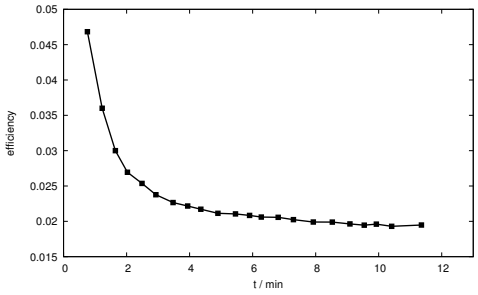

(b) Efficiency

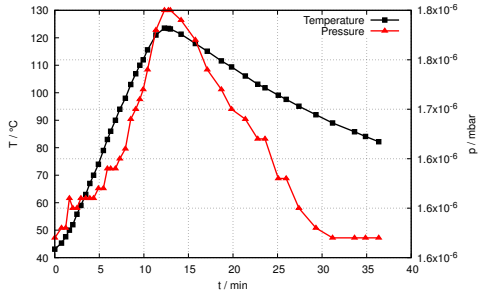

(c) Temperature, pressure

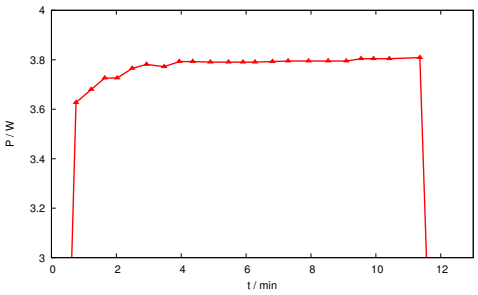

(d) Power

Figure 3.19: Measurement of several electron observables parameters over time. The filament was heated with a constant current of $I_f = 2.3\,\mathrm{A}$. The heating was turned off after roughly 11.5 min.

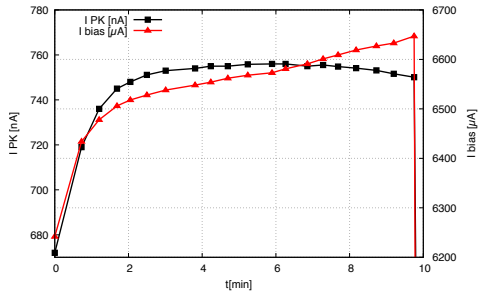

(a) Current

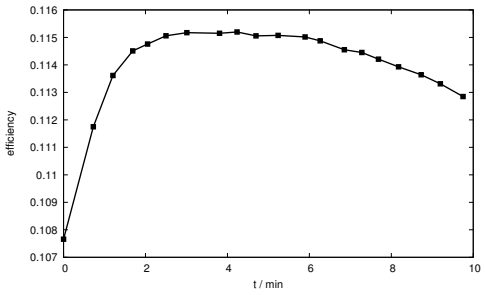

(b) Efficiency

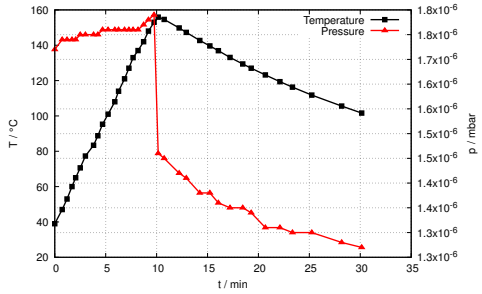

(c) Temperature, pressure

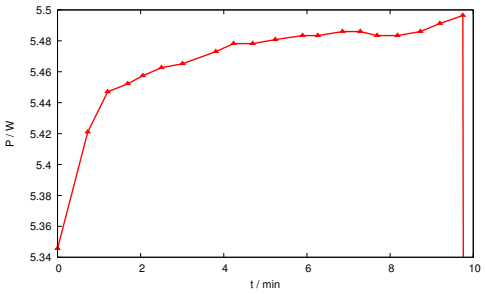

(d) Power

Figure 3.20: Measurement of several electron source observables over time, similar to figure 3.19, but using a heating current of $I_f = 2.65\,\mathrm{A}$, which was deactivated after roughly 10 min.

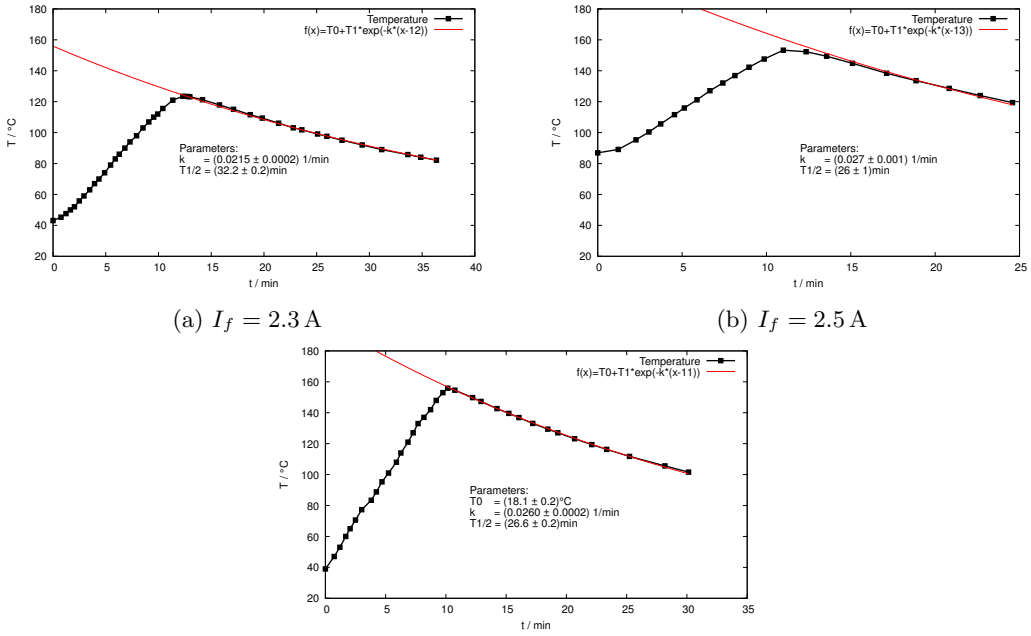

(a) $I_f = 2.3\,\mathrm{A}$ (b) $I_f = 2.5\,\mathrm{A}$

(c) $I_f = 2.65\,\mathrm{A}$

Figure 3.21: Exponential fit of the decreasing temperature over time after the electron source was operated. 2.3 A, 2.5 A and 2.65 A of heating current were applied. The last fit did not converge if the equilibrium temperature T_0 is fixed. Nevertheless, the resulting value is close to 20 °C, which was the temperature of the laboratory due to air conditioning.

cooldown state after a few minutes of operation in order to keep the temperature below 180 °C, compare figure 3.21.

In order to observe the effects of the non-equilibrium state and the changes over time, the source has been operated at fixed settings of $U_{\mathrm{BIAS}} = 100\,\mathrm{V}$, $U_{\mathrm{GATE}} = 128\,\mathrm{V}$, $I_{\mathrm{f}} = 2.3\,\mathrm{A}$, $L = 97\,\mathrm{mm}$. The changes in the measured parameters have been analysed. In figure 3.19a, the pickup current and the bias current can be observed with respect to time. The pickup current is decreasing over time, while the bias current shows a maximum after 4 minutes. Comparing this observation to the power consumption by the filament shown in figure 3.19b, we can see that the emission of the filament reaches a peak shortly after the heat up phase is complete and the power draw of the filament increases only slightly. Afterwards the emission worsens. The emission efficiency shows a similar behaviour, as it is dropping exponentially by about 60 % and saturating at a very low level, compare figure 3.19d. Measurements were taken for more than 15 minutes after the filament heating had been turned off. Therefore, the temperature and the pressure changes can be observed during the heating and the cool-down phase. The measurements have been repeated at a higher heating current of 2.6 A while all other parameters kept constant, compare figure 3.20. Concerning the temperature, pressure and power consumption of the filament, the observations are similar to the previous measurement. In contrast, while the currents showed a decreasing trend using 2.3 A heating current, an increasing trend in the bias current can be observed in figure 3.20a. Furthermore, the efficiency obtains a maximum 2 to 4 min after the heating is deactivated, compare figure 3.20b.

As the whole anode was utilized as pickup, minor differences in the measurements aside from the increase in pickup current result in a change in efficiency. In this case, the drift in the pickup current is not as strongly visible as in figure 3.19a.

The temperature drop measured in the gate ring has been recorded for various heating currents and at several temperature levels, compare figure 3.21. The exponential decay of the temperature was fitted by the Newtonian law of cooling:

$$T(t) = T_0 + T_1 e^{-kt}$$

Here, T_0 is the equilibrium temperature, T_1 the difference between start and equilibrium tem-

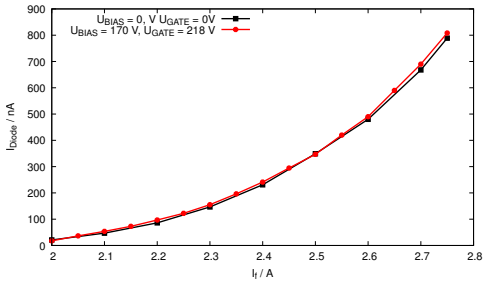

(a) Diode brightness

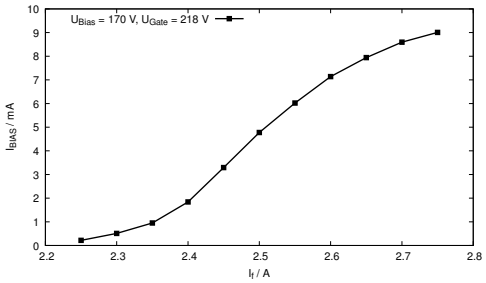

(b) Bias current

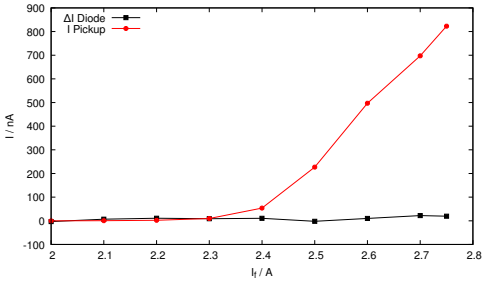

(c) Black: difference between the diode current curves displayed in figure 3.22a. Red: current on the photo diode casing.

Figure 3.22: Since the electron current on the pickup is significantly larger than the difference between the diode current curves, electrons impacting on the diode do not influence the diode current and therefore the brightness measurement.

perature and k describes the decay from the start temperature to the equilibrium temperature. The results of the fit are summarised in table 3.1. The fit of the measurement utilizing 2.3 A filament current uses the most data points, therefore the fit is expected to be the most precise. As $T_0 = 20\,°\mathrm{C}$ for all measurements due to air conditioning in the laboratory and T_1 can be read from the graphs in figure 3.21, these variables are fixed for the fit, leaving only the decay constant k as a variable. It was necessary to leave T_0 variable for the third fit because the algorithm would not converge to the correct solution if $T_0 = 20\,°\mathrm{C}$ was chosen as a constant. As a result, we find the decay parameter $k = (25 \pm 2) \times 10^{-3}\,1/\,\mathrm{min}$ and the half life of the temperature $T_{1/2} = (29 \pm 2)\,\mathrm{min}$.

If we assume a maximal temperature during operation of the electron source of 150 °C, an increase in temperature due to operation from 75 °C lasts between approximately 7 min for 2.3 A to 6 min for 2.65 A After this period, 35 to 40 minutes are necessary to achieve the start temperature of 75 °C. This leads to a duty cycle of maximal 15 % with an operation time of 6 min.

3.2.4 Diode measurements

During the measurement sessions, the small pickup was replaced with a photo diode. In the scope of the NNP group, different arrays of photo diodes are tested as an optical detector for plasma densities due to residual gas light emittance. A photo diode builds a given voltage with respect

I_{filament} [A]	T_0 [°C] est	T_1 [°C] est	T_0 [°C] fit	k [1/min]	$T_{1/2}$ [min]
2.3	20	105	-	0.0215 ± 0.0002	32.2 ± 0.2
2.5	20	133.2	-	0.0270 ± 0.001	26.0 ± 1
2.65	20	135.5	18.1 ± 0.2	0.0260 ± 0.0002	26.6 ± 0.2

Table 3.1: Overview of the temperature fits of figure 3.21.

to the light intensity that impacts on the semiconductor. The voltage is detected as a current that is formed in a closed circuit with a given resistance. It was proposed that exposure of the semiconductor to an electron beam is influencing the diode current. Therefore, the light emitted by the filament has been measured with the photo diode while the emission of the electron source is first inactive and active afterwards. In order to increase the current on the diode, the electron source has been moved all the way in, to the position $L = 40\,\mathrm{mm}$. The results are displayed in figure 3.22a. Activating the extraction and therefore the electron beam has no significant influence on the measurement of the diode current, since the current deployed on the diode is much larger than the difference in current between the measurements with and without electron beam, compare figure 3.22c. It is important to note that the electron current on the diode is not constant for all values of I_f. Note that the area used to record the current on the diode is a metal ring positioned symmetrically in front of the electron source. The ring contains the semiconductor and a circular glass plate covering the semiconductor.

In conclusion, the performance of the tested photo diode does not depend on the influx of sub $10\,\mu\mathrm{A}$ of electrons. Furthermore, the extraction of electrons from the filament matches the theoretical prediction and 2.7 A of heating current is a suitable regime of operation for this type of filament, since the bias current saturates at a higher heating power, compare 3.22b. On the other hand, the current measured on the diode casing shows a different behaviour. This indicates that other effects might contribute to the extraction of electrons and the density profile of the resulting electron beam. Therefore, the extraction out of the electron source should be improved in the future.

3.2.5 Ignition parameters

It is necessary to measure the ignition parameters of the Gabor lens with respect to the new setup, especially with respect to the position of the electron source. Ignition in this context describes a chain reaction of residual gas ionization that increases a large amount of free electrons. When the confinement is saturated and the Gabor lens is filled, more losses are generated due to the potential depression because of the space charge of the electrons and the system reaches an equilibrium. This equilibrium may be the stable operation mode or an instability, depending on potential, magnetic field and pressure.

Two measurements with respect to the position of the electron source were conducted. First, the source was moved out of the system as far as possible at $L = 135\,\mathrm{mm}$. In the second measurement, the front surface of the source has been aligned with the anode surface.

During the measurements, a given magnetic field was applied to the system. In a second step, the potential was increased until ignition was observed. Afterwards, the pressure was recorded. The results of these measurements can be found in figures 3.23 and 3.24.

The operation of the Gabor lens is a three-dimensional problem, as the potential, the magnetic field and the residual gas pressure are significant for the confinement and plasma properties in an experiment. For simplicity, it is possible to observe ignition along the work function, thus coupling the potential and magnetic field, and increasing the pressure to obtain the ignition point. The results of this measurement are illustrated in figure 3.25. The observable ignition region in the present experiment is limited by two factors. If a potential of 6 kV or more is applied with the appropriate magnetic field, the Gabor lens will ignite at base pressure of the system of approximately $1 \times 10^{-7}\,\mathrm{mbar}$. Therefore, the described measurement is impossible for potentials equal or above 6 kV. Below 3 kV, no ignition can be observed for pressures below $1 \times 10^{-4}\,\mathrm{mbar}$. As it is unhealthy for the turbo molecular pumps to operate in regimes above $1 \times 10^{-4}\,\mathrm{mbar}$, this pressure marks the limit for the measurement.

3.3 Effect of a present electron beam on ignition behaviour

3.3.1 Characterization of the electron source

The emission characteristics of the electron source were measured again, since the filament had been changed in the meantime. Since both the anode and the pickup are used to measure the current emitted by the electron source , these measurements were conducted with a potential of 8 V that was applied to the anode in order to prevent corruption of measurements due to

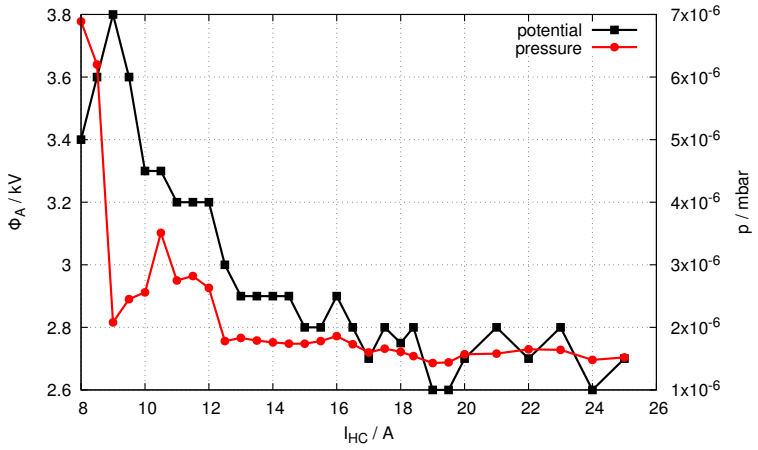

Figure 3.23: Ignition parameters of the Gabor lens without the electron beam. The electron source was positioned as far outwards from the centre as possible. During the measurements, the magnetic field given by the current was set, then the potential was increased until the plasma ignited. The red line shows the pressure recorded after the lens was ignited. No residual gas was added to the system.

secondary electrons. The results are displayed in figure 3.26. Using a bias of 8 V on the anode roughly doubles the current measured on the anode and pickup.

In favour of having a better understanding of the properties of the electron source, CCD images of the interior of the Gabor lens were taken in order to observe residual gas light emittance caused by the electron beam. In order to improve the signal-to-noise ratio, a background image was taken and the intensity subtracted from a second measurement image. As the filament of the electron source emits intense light and the residual gas light is rather dim, the signal-to-noise ratio in these optical measurements is poor, although background images were taken. In order to improve the image quality, the beam intensity was increased to roughly 1 mA, as measured using the anode and pickup. Furthermore, the residual gas pressure was increased to $p = 1 \times 10^{-4}$ mbar using Argon. Figure 3.27, left, shows an image of the electron beam in the Gabor lens without any anode potential or magnetic field. The electron source is located to the left. The intensity pattern resembles a strongly divergent beam. Due to saturation of the CCD chip while taking the background and measurement image, the flange is clearly visible, as the intensity on most of the flange surface is zero after subtracting both images.

To check whether the observed residual gas light emission is caused by the electron beam, a transversal magnetic field of 7 mT (12.5 A in the coils) was applied and a second set of pictures was taken, see figure 3.27, right. With magnetic field active, the electrons are exposed to the Lorentz force and the emitted light concentrates at the left edge of the image. As the image of the beam changed substantially when introducing a magnetic field, it can be concluded that the structure visible in figure 3.27 is the electron beam.

Additionally, it is necessary to evaluate if electrons are confined in the Gabor lens. Therefore, it is useful to detect the loss currents on different surfaces. The measurement setup was expanded by several ampere meters which are measuring the loss currents on different surfaces, compare figure 3.28. Here, $I_{\mathrm{l,\,s}}$ measures the electron losses on the grid, the source casing and the vacuum vessel before the insulating flange. $I_{\mathrm{l,\,a}}$ measures the losses on the anode. $I_{\mathrm{l,\,o}}$ is calculated from the bias current, I_{BIAS}, and the previously mentioned loss currents. The sum of all currents in equilibrium should be zero, therefore we can note the current balance:

$$I_{\mathrm{BIAS}} = I_{\mathrm{l,\,s}} + I_{\mathrm{l,\,a}} + I_{\mathrm{l,\,o}}$$

If electrons are inserted into the Gabor lens, there should not be instantaneous losses in longitudinal direction. Once the maximum electron density is reached, the confining potential will be shielded by the electrons, so that longitudinal losses become possible. In an equilibrium state, $I_{\mathrm{l,\,o}} > 0$ should be fulfilled. As losses on the electron source system and losses on the anode are measured separately, the only possibility for electrons to contribute to $I_{\mathrm{l,\,o}}$ is by escaping the

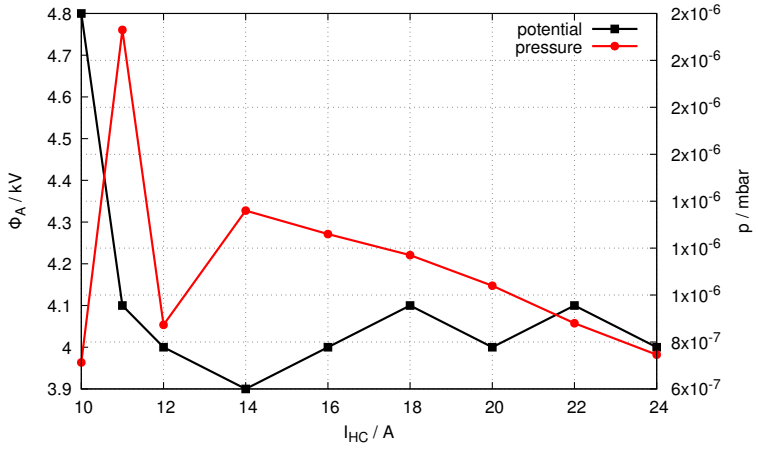

Figure 3.24: Here, the ignition parameters have been recorded again with the electron source located planar to the inner anode surface. The electron beam was not used in this measurement. The potential necessary to ignite the lens at a given magnetic field is higher than during the measurements shown in figure 3.23, since the pressure is lower than during the previous measurement.

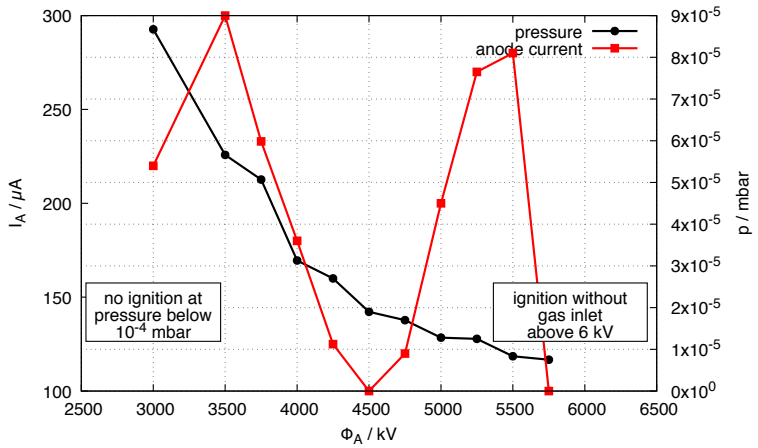

Figure 3.25: Ignition parameters along the work function with He as residual gas. $L = 97\,\mathrm{mm}$. The electron source was not used.

confinement longitudinally. Measuring the currents with different configurations revealed that $I_{\mathrm{l,\,s}}$ is predominantly in the order of magnitude of I_{BIAS}, while $I_{\mathrm{l,\,a}}$ is roughly the difference between I_{BIAS} and $I_{\mathrm{l,\,s}}$. As a result, $I_{\mathrm{l,\,o}}$ is in the range of a few µA and, depending on the experimental parameters, may change signs.

On the independence of electron source loss current and anode current

Calculating $I_{\mathrm{l,\,o}}$ from the other loss currents and the bias current in this way is independent of the condition of the Gabor lens and independent of the plasma. This can be measured for instance by increasing the electron current out of the electron source without confinement at a pressure of $2 \times 10^{-7}\,\mathrm{mbar}$, which does not modify the anode current. Additionally, the loss currents in figure 3.28 form closed circuits on the anode and the electron system. Aside from $I_{\mathrm{l,\,o}}$, they do not interact with ground and therefore have no influence on the anode current. As $I_{\mathrm{l,\,o}}$ was found to be very low compared to the other loss currents, compare table 3.2, the electron beam does not influence the anode current directly in a significant magnitude. Instead, if beam electrons are confined and aid in residual gas ionization, the resulting ions and loss electrons on the anode contribute to the anode current. Both ions and electrons contribute in the same way to the loss

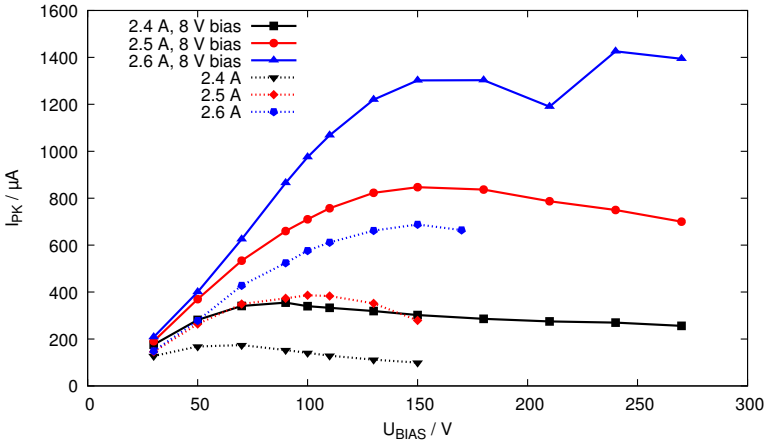

Figure 3.26: Current measured by using the anode as pickup, with 8 V positive potential. The dotted lines represent the corresponding measurements without 8 V bias on the anode and are taken from the dataset in figure 3.18.

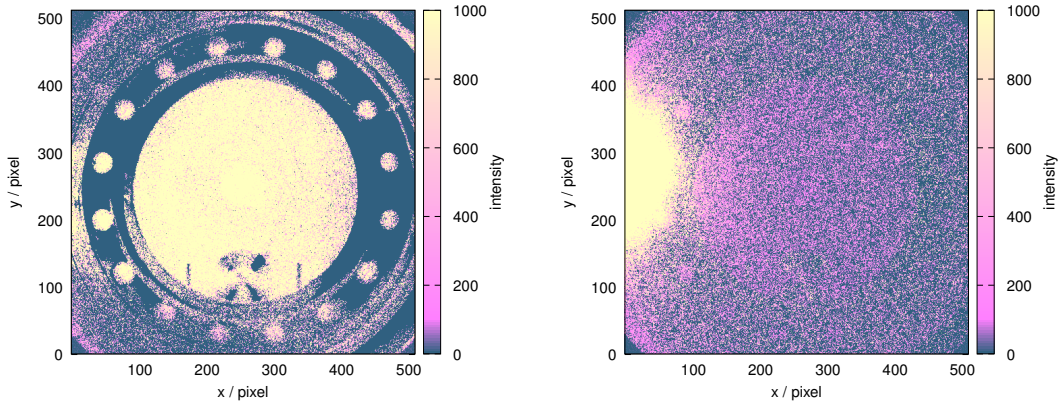

Figure 3.27: CCD image of the electron beam. Left: without magnetic field, right: transversal magnetic field of 7 mT. $p = 1 \times 10^{-4}$ mbar (Argon)

current, since positive ions are extracted by the anode potential out of the Gabor lens towards ground and electrons are drawn towards the anode. Both effects can be understood as a current from anode to ground. Therefore, any response of the anode current due to a modification in the electron beam in this setup corresponds to the confinement of electrons.

Nonetheless, the transient time of the system until an equilibrium is reached might be very short, so that only the equilibrium state is observed. In an equilibrium, the longitudinal loss current may be close to zero, as the electrons have to gain roughly:

$$E_{\text{escape}} \approx e\Phi_A - \frac{e^2 R_A^2}{2\epsilon_0} n - eU_{\text{BIAS}}$$

$$E_{\text{escape}} \approx 4000\,\text{eV} - 705\,\text{eV} - 200\,\text{eV} = 3095\,\text{eV}$$

Here, an enclosed electron density of $1 \times 10^{13}\,/\text{m}^3$ was assumed in compliance with the measurement results in table 3.2 in order to achieve a rough estimate of the escape energy. The second term in the escape energy takes into account that the potential is reduced by a cloud of electrons of density n. Therefore, the losses that balance the electrons inserted by the electron source are probably located on the anode. Furthermore, it has been observed that by increasing the magnetic field, $I_{\text{l, a}}$ decreases and $I_{\text{l, s}}$ increases in such a way that both changes cancel out and the longitudinal loss current is not modified within the limits of resolution.

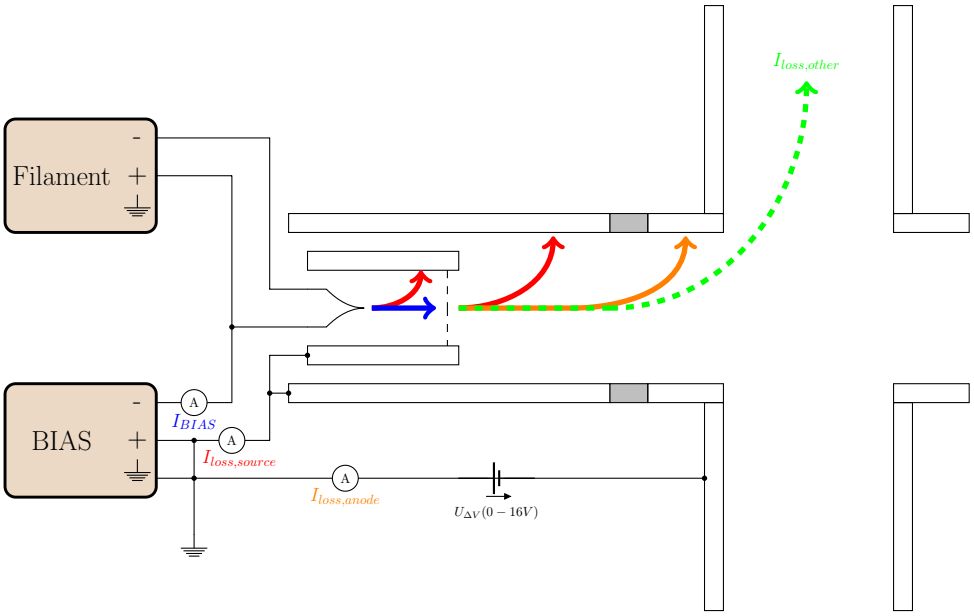

Figure 3.28: Circuit diagram: Measurement of loss currents.

3.3.2 Results

One of the intentions of this thesis is to investigate the effect of an electron source on the ignition behaviour of the Gabor lens. For the following description of the measurement process, compare figure 3.29. First, a fixed point on the work function of the lens is approached in terms of potential $\Phi_A = 4\,\mathrm{kV}$ and magnetic field $B = 5.02\,\mathrm{mT}$, but a very low residual gas pressure around $2 \times 10^{-7}\,\mathrm{mbar}$ prevents natural ignition. Then, the pressure is increased using He gas until ignition is observed as a step in the current of the anode power supply (point 1). Afterwards the electron source is activated and set to a state of high current ($I_f = 2.5\,\mathrm{A}$, $U_{\mathrm{BIAS}} = 100\,\mathrm{V}$, $U_{\mathrm{GATE}} = 128\,\mathrm{V}$, $L = 85\,\mathrm{mm}$). Then the pressure is increased, until a change in the anode current is observed.

Contrary to the previous measurement, no step in the anode current is measured, but a linear increase is observed. The data is taken at the beginning of the linear segment of the current increase (point 2). The pressure is increased further until the pressure of natural ignition is reached (point 3). At a higher pressure than before, a step in the anode current is observed (point 4). Afterwards, the conditions (potential, magnetic field and pressure) at point 3 were implemented with the electron beam and therefore without the ignited plasma in the Gabor lens. Following that, the potential has been increased in steps of 100 V until ignition was observed. The results are collected in table 3.2.

Contrary to previous expectations, the electron source prevented ignition at the parameters of point 3. A halo of electrons similar to 2.8c could shield the inner region of the Gabor lens from the potential of the anode, so that at the given parameters of point 3, not enough energy could be supplied by the anode potential in order to provide ignition conditions. Increasing the anode potential should compensate this shielding effect. Furthermore, $\Delta\Phi = \Phi_{\text{point 5}} - \Phi_{\text{point 2}}$ should be equivalent to the depression of the anode potential due to a confined electron density, so an electron density could be calculated from this potential difference similar to the evaluation of the impulse spectrometry measurement with the use of equation (2.1).

The ignition measurement shows that an electron beam suppresses ignition in the classical interpretation. Instead, a new slow type of ignition is observed. With the electron beam active, the anode current begins to rise at a lower pressure than the pressure at the classical ignition point, so the conductivity between anode and ground is non-zero. In this case, some charge is transported from anode to ground, which is an indicator for free ions and electrons confined in the volume of the Gabor lens. Note that most electrons inserted by the electron source do not contribute directly to the anode current, as they form a closed circuit from electron source to anode, which are again connected via the HV supply for the electron source system in the

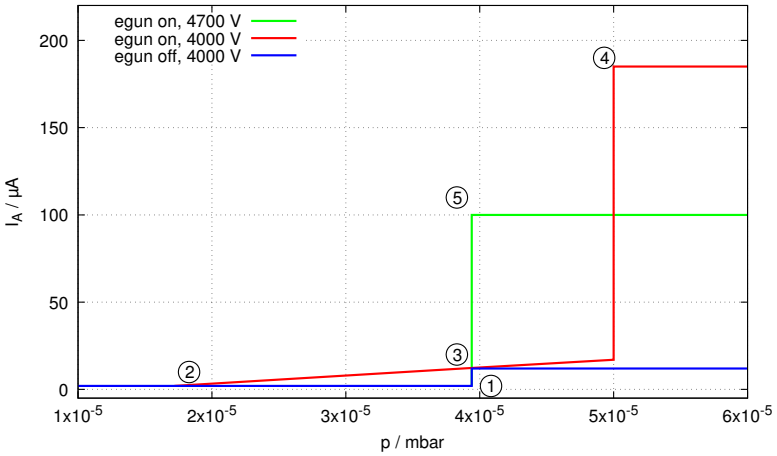

Figure 3.29: Sketch of the measurement events during the ignition measurements. 1: Natural ignition without electron source active. This point is identified by the step in the anode current. 2: If the electron source is active, the anode current begins to rise slowly at a smaller pressure than the natural ignition. 3: The anode current continues to rise until the parameters of the natural ignition are reached. 4: A step in the anode current occurs at a higher pressure than before. Also, the anode current is higher. 5: With the electron source being active, the parameters of 3 are applied and the anode potential is increased, until a step in the anode current is observed.

configuration shown in figure 3.28. Only $I_{\mathrm{l,\,o}}$ contributes to the anode current.

Comparing table 3.2, the resulting longitudinal loss current $I_{\mathrm{l,\,o}}$ is negative. This could be explained by positive ions impacting on the electron source, since they might be attracted by the negative potential of the electron beam. Ions impacting on the electron source increase $I_{\mathrm{l,\,s}}$. The measurement results at point 4 indicate that ions could be the reason, since $I_{\mathrm{l,\,s}}$ is larger than I_{BIAS}. As I_{BIAS} is the current extracted from the filament, it is expected that no loss current can be larger than I_{BIAS}.

In conclusion, the ignition process with a electron beam shows large differences to a conventional ignition process. Due to the electron beam, accumulation of electrons starts at lower pressures than classical ignition. There is no peak in the anode current until the classical ignition pressure is reached. Instead, the anode current is increasing monotonously. At the classical ignition pressure, the confined electron density with and without electron source are equal within the precision of the density measurement.

Since the measurement of the impulse spectrum had to be conducted within a very short time, the density of samples in the spectrum is comparably low, leading to a uncertainty in the density measurement of roughly $1 \times 10^{12}\,1/\mathrm{m}^3$.

Increasing the pressure past the classical ignition point led to a further increase of the anode

#	U_A [V]	p [mbar] (He)	I_A	P_f [W]	I_{BIAS}	$I_{\mathrm{l,\,s}}$	$I_{\mathrm{l,\,a}}$	$I_{\mathrm{l,\,o}}$	n_e [1/m^3]
1	4000	3.95×10^{-5}	12	0	0	0	0	0	7.70×10^{12}
2	4000	1.72×10^{-5}	1-2	6.52	2763	2720	43	0	5.55×10^{12}
3	4000	3.94×10^{-5}	13	6.58	2668	2640	47	-7	7.70×10^{12}
4	4000	5.75×10^{-5}	150	6.54	2849	2970	91	-212	1.39×10^{13}
5	4700	3.94×10^{-5}	103	6.58	2730	2750	10	-30	1.36×10^{13}

Table 3.2: Results of the ignition measurement at 4 kV and 8.91 A/5.02 mT, compare figure 3.29. The electron source is operated at $U_{\mathrm{BIAS}} = 100\,\mathrm{V}$, $U_{\mathrm{GATE}} = 128\,\mathrm{V}$. As I_{BIAS} is the current emitted by the filament, measurement 4 indicates a large error in measuring the other currents, because the loss current in the source is already larger than the bias current. All currents are measured in µA.

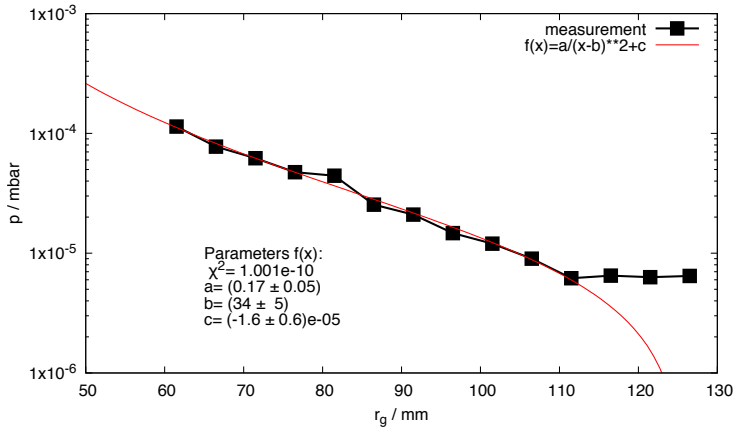

Figure 3.30: Ignition pressure with respect to the position of the electron source.

current until a step in the current was observed. Since the simulations indicated that the electrons would form torus shaped clouds it was postulated that such a formation is shielding the anode potential, so that not enough energy for the ignition process is available in the plasma. Starting with classical ignition pressure and increasing the potential led to ignition at 4700 V. This indicates, that the shielding effect of a torus cloud indeed suppresses ignition at the classical parameters.

Nevertheless, since the anode current is larger than the base current, using the electron source introduces electrons that are confined in the Gabor lens. Furthermore, the ions used tor the density measurement indicate residual gas ionization processes in such a configuration.

3.4 Influence of the position of the electron source on the ignition behaviour

During the diode measurements, it was observed that the Gabor lens is unable to ignite at potentials below 8 kV with a magnetic field of $B = 7.1\,\mathrm{mT}$ and pressures below 10^{-4} mbar if the electron source is penetrating deep into the plasma chamber, for instance at $L = 40\,\mathrm{mm}$. In order to examine the effect of the position of the electron source on the ignition properties, the potential was fixed to 4 kV and the magnetic field to 5.02 mT on the work function. Then the pressure was increased using He until ignition was observed. This was repeated for various positions of the electron source. The results are displayed in figure 3.30 with respect to the position of the electron source r_g. The position parameter L is proportional to the radial position of the front of the electron source r_g, compare equation (3.2). As the source is inserted into the plasma volume, the volume available for confinement is truncated.

In order to understand the effect of the electron source, the ideal gas law for the inner volume that is not yet truncated by the electron source has to be considered.

$$pV = Nk_BT$$

Assuming that in order to perform ignition, the number of residual gas particles in this volume has to be kept constant, and further assuming that there is no change in temperature, the ideal gas law can be written as:

$$p = \frac{\text{const.}}{V} = \frac{\text{const.}}{l\pi r_g^2}$$

Here, r_g is the radius of the electron source. This function is fitted to the data and the result is shown in figure 3.30. Following this theory, the decrease in volume available for plasma ignition can be compensated by increasing the residual gas pressure. Therefore, a given absolute amount of residual gas particles has to be present so that the system can be ignited. It has been shown at IAP by conducting measurements on several Gabor lens systems that decreasing the volume of a Gabor lens leads to an increase in ignition pressure [23].

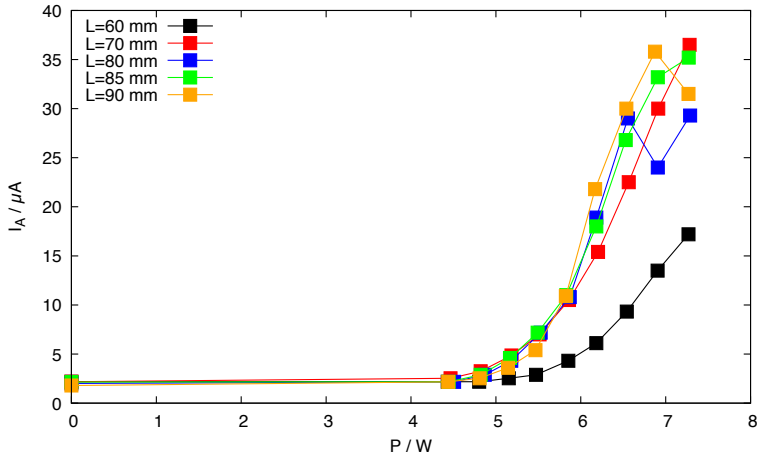

Figure 3.31: Response of the anode current on the electron beam. For each value of L, the pressure has been adjusted to a value slightly before ignition, compare figure 3.30. It was not possible to adjust the pressure accordingly for $L = 60\,\mathrm{mm}$, since the pressure would have exceeded the upper limit of the pumping system.

3.5 Electron beam induced ignition

As mentioned before, the positive effects of electrons inserted into a Gabor lens in terms of ignition behaviour and increase of the electron density enclosed in the plasma trap are subject to investigation in this thesis. Before, the classical ignition behaviour has been investigated with respect to the presence of an electron beam in section 3.3.2. Now, the electron beam is supposed to be the driving force behind ignition. The Gabor lens is operated at a state close to ignition, thus, 4 kV potential and 5.03 mT magnetic field are applied. The electron source was moved to several positions and a slightly smaller pressure than the corresponding ignition pressure was applied to the system, compare figure 3.30. The electron source was operated at $U_{\mathrm{BIAS}} = 170\,\mathrm{V}$ and $U_{\mathrm{GATE}} = 218\,\mathrm{V}$. During the measurements, the current of the anode power supply I_A was recorded with respect to the heating of the filament (figure 3.31) and with respect to loss current on the anode $I_{\mathrm{l,a}}$ (figure 3.32).

It can be observed that during the measurements, I_A is increased up to 35 µA, which can be identified as ignition. This is the maximum current for all tested positions and is limited by the current that is inserted by the electron source, which is kept constant. As a result, ignition of the Gabor lens utilizing an electron beam in order to compensate a lower pressure than usually required is possible. Comparing figure 3.32, the current extracted from the electron source is larger than the anode current. Therefore, in theory, the anode current may be a part of the source current and not the result of ignition. The bisectrix indicates that the anode current is larger than the loss current for $L = 60\,\mathrm{mm}$ and $L = 70\,\mathrm{mm}$, so for these results, the anode current is larger than the electron loss current. Thus, ignition is observed. Concerning the remaining measurements, the independence of loss current and anode current is furthermore thoroughly discussed at the end of section 3.3.1.

Repeating this experiment at the minimal pressure of $2 \times 10^{-7}\,\mathrm{mbar}$ does not yield any increase of I_A with respect to $I_{l,a}$. Therefore, the response in the measurement described by figures 3.31 and 3.32 is due to residual gas ionization via the electron beam.

The black curve in figure 3.31 was recorded with a much lower pressure relative to the ignition pressure than the other measurements, as the pumping limit was reached. Therefore, this curve shows the onset of the ignition via the electron source. If the pressure was larger, the curve would be congruent with the other measurements in this figure.

3.6 Density boosting

Besides aiding the ignition process, the electrons inserted by the electron source are supposed to increase the electron density inside the Gabor lens during conventional operation. In addition,

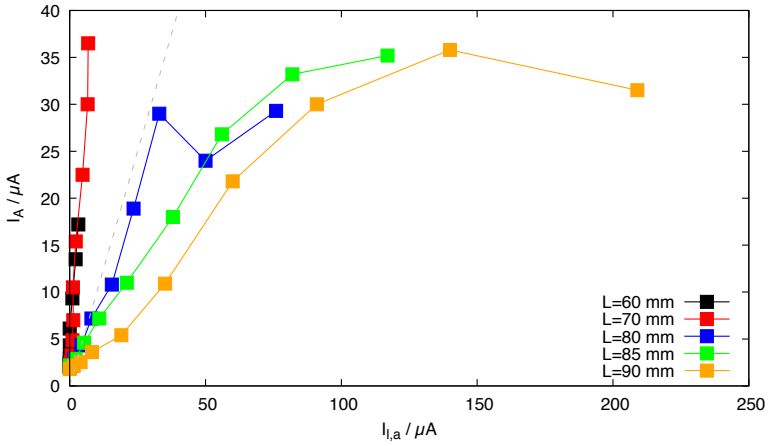

Figure 3.32: In comparison to figure 3.31, the same measurement results are plotted against the electron source loss current on the anode $I_{\mathrm{l,a}}$.

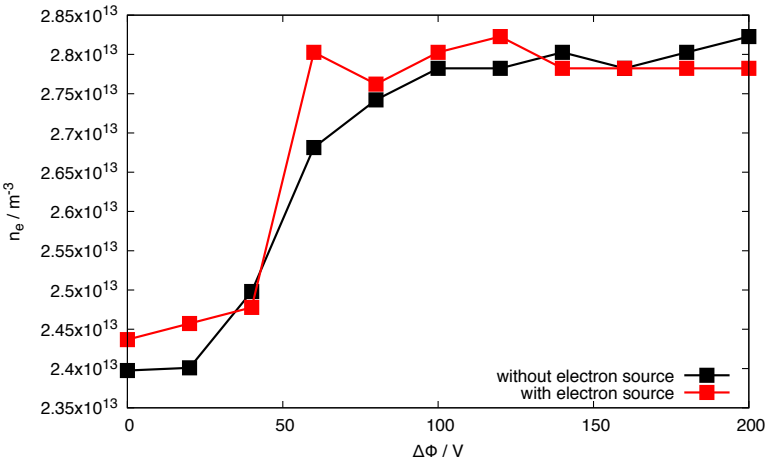

Figure 3.33: Comparison between the densities in the Gabor lens with and without electron beam with respect to the potential difference between anode and electron source.

the simulations presented in this thesis indicated that a potential difference between the anode and the electron source is beneficial for the resulting amount of confined electrons. The electron source was positioned at $L = 90\,\mathrm{mm}$ and He was used as residual gas at a pressure of 6.5 to $6.7 \times 10^{-6}\,\mathrm{mbar}$.

A second high-voltage power supply was used to adjust the voltage of the electron source separately from the anode. Therefore, the anode and electron source system were disconnected. As a result, it is not possible to measure $I_{l,a}$ in this configuration. The density was measured by obtaining a momentum spectrum of the residual gas ions, finding the maximum and calculate the potential depression due to confined electrons. As discussed before, the potential difference corresponds to the density of the electrons confined in the Gabor lens. The results of this measurement are shown in figures 3.33 and 3.34.

The potential difference is chosen in such a way that the potential of the anode is 4 kV and the potential of the electron source system is lower than the potential difference. The electron source was operated at $U_{\mathrm{BIAS}} = 170\,\mathrm{V}$ and $U_{\mathrm{GATE}} = 218\,\mathrm{V}$ with $I_f = 2.6\,\mathrm{A}$. During the measurements, the points for both curves were measured in an alternating pattern by switching the heating of the filament on or off. In this configuration, the potential difference contributes to the kinetic energy of the electrons as well as the extraction out of the electron source. Therefore, this effect can probably not be replicated by increasing the energy of the electrons by modifying U_{BIAS}.

It can be shown that a potential difference of 100 V between anode and electron source

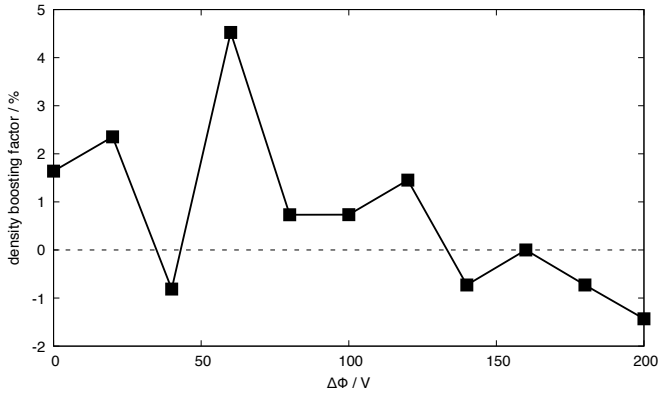

Figure 3.34: Percentual difference between the density measurement with and without electron source. Positive values indicate a density increase with the electron beam.

leads to a density increase of approximately 14 % independent of the density boosting effect of the electron beam. Comparing the boosted density with the non-boosted density, there is only a minor difference in the measured density of 5 % at most, compare figure 3.34. In certain configurations, the density is lower with the electron beam active. Especially in the regime of $\Delta\Phi > 100\,\mathrm{V}$, the presence of the electron beam does not make a noticeable difference, as the density measurement is at the limit of precision in this case. In order to increase the precision, the momentum spectrum has to be sampled with a smaller step size in the magnetic field of the dipole, which could be done in a future experiment.

3.7 Ageing effects

If a filament is in use over a longer period of time, a degrading effect can be observed which will eventually lead to breaking of the filament wire. During operation, the surface of the filament is severed, leading to a thinner wire over time, observable by the increasing resistance. Hence, the resistance is plotted against the number of measurements the filament has been used in in figure 3.35. Furthermore, the maximal temperature that was recorded in the gate ring during this measurement is plotted for reference as well. As most measurements have a similar duration, the axis of abscissas in this plot can be interpreted as a non-linearly scaled time axis.

If the temperature increases between two measurements, the resistance in the following measurement is predominantly higher. Nevertheless, sometimes the resistance is lower. Noticeable is the large peak close to measurement no. 20. The sharp increase in resistance could be explained by a very large temperature in the measurement just before, which was not the case. Instead, a short connection cable between filament and power supply had been swapped with a long cable. This could explain the sudden rise of the resistance as well.

Furthermore, the alumina layer of the gate ring seems to suffer deterioration, as the resistance between gate ring and electron source casing vanishes after approximately 10 to 20 hours of operation. Possibly, the oxygen is reduced in a very slow chemical reaction due to the heat of the filament, and the resulting oxygen molecules are removed from the system by the vacuum pumps. A comparison between two gate rings at two different times is shown in figure 3.36. Both gate rings lost the resistance towards the electron source casing at one point during the experiments. After some time, the resistance recovered but the gate ring was prone to a new breakdown of the insulation towards ground afterwards. Changing the gate ring, that is swapping ring 2 with ring 1, ring 2 being the ring that produced a breakdown and was in operation before swapping, did provide approximately 10 to 20 hours of operation without errors. Afterwards, ring 1 failed during the measurement. As the gate voltage dropped from 218 V to zero, the bias current increased tremendously to a little above 8 mA. During normal operation with the gate ring polarized, 3 to 4 mA of bias current are expected.

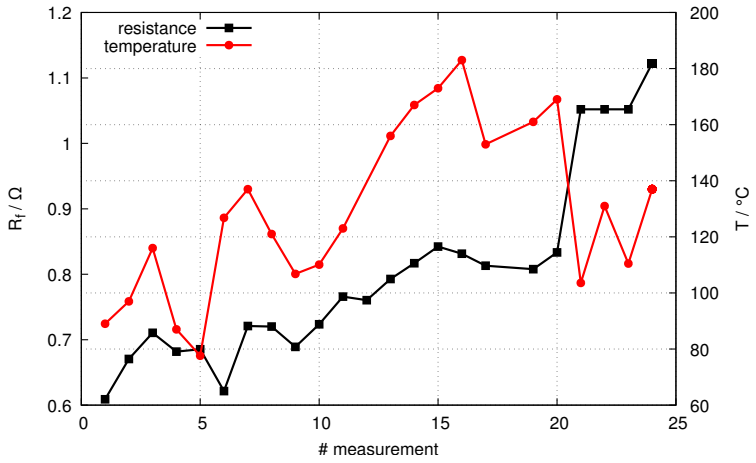

Figure 3.35: Resistance of the filament at the end of each measurement. During the different measurements, the resistance is increasing. This is an indicator of ageing of the filament. The maximum temperature measured in the electron source is plotted in red.

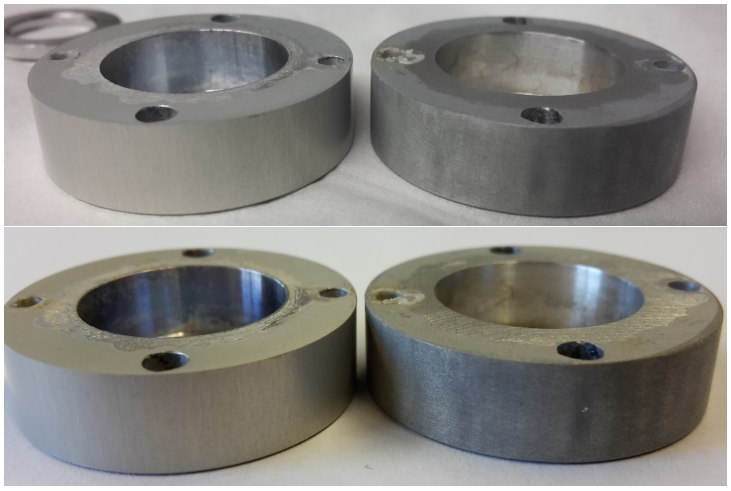

Figure 3.36: Comparison between a gate ring 1 (left) and 2 (right). Top: image taken after ring 2 lost insulation towards the chassis. Ring 2 was replaced by ring 1 in the electron source. Bottom: image taken after ring 1 lost insulation. The orentation of the rings with respect to the camera is the same in both images.

3.8 Conclusions of the experiments

During several measurement sessions in Bologna and Frankfurt, the electron source was optimized for the environment in a Gabor lens by adding a magnetic shield and a gate ring that acts as a Wehnelt cylinder. If the electron source is operated at a moderate heating power of 6.45 W, 0.8 to 1 mA electron current can be extracted. If the heating power is increased up to 7.15 W, up to 1.4 mA can be provided. Increasing the bias and gate voltages can supply up to 1.3 mA at 6.5 W heating power.

Furthermore, the electron source suffers from ageing and deterioration effects, as the resistance of the filament increases over time, which is displayed in figure 3.35. In addition, the gate ring suffers from breakdowns of the insulation towards the electron source casing after several hours of operation, compare figure 3.36. As the gate ring is composed of aluminium, the temperature inside the electron source has to be monitored in order to prevent a meltdown of the gate ring due to the hot filament. Due to the sensitivity to high temperatures, the continuous operation time is limited. Measurements of the decaying temperature after operation show that a duty cycle of at most 15 % can be achieved.

The electron source has no focussing device after the extraction grid. Therefore the emittance of the electron beam is presumably immense, compare figure 3.27. For this reason, it is very difficult to detect the electron beam with the CCD camera. Inserting a focussed beam is very interesting, as it would allow for easier observation of the way that electrons are inserted into the volume. Additionally, the bright light emitted by the filament leads to a disadvantageous signal to noise ratio when taking images with the camera. Therefore, neither the electron beam, nor the confined electron plasma could be observed precisely.

A photo diode was used in order to measure the brightness inside the Gabor lens with respect to the heating current of the filament. The brightness distribution, symbolized by the diode current, did not change with respect to the gate and bias voltages. As a result, diodes may be used in the future for optical diagnostics of the electron source or the electron plasma, since they are immune to electron beam exposure up to 0.9 µA.

Concerning the Gabor lens, the ignition parameters pressure, potential and magnetic field have been examined without the electron source in operation in order to obtain a guideline for further experiments. Here, only potential and magnetic field values that are part of the work function were utilized in order to simplify the measurement. These measurements determined the potential, magnetic field and pressure ranges for the further experiments. Since the ignition behaviour is dependent on potential, magnetic field and residual gas density and composition, more measurements than presented in this thesis have to be conducted in order to perform a proper characterization of the ignition behaviour.

Additionally, the ignition parameters on the work function have been examined with respect to the position of the electron source. For these measurements, potential and magnetic field have been held constant and the ignition pressure was measured with respect to the position of the electron source. Inserting the electron source into the plasma volume hinders ignition. This effect can be compensated by adding more residual gas atoms to the system by increasing the pressure. Finally, it was shown that the electron source can be used to supply enough electrons in order to perform an ignition without the need to increase the potential, magnetic field or pressure.

Furthermore, the density of the enclosed electron plasma was measured with respect to the potential of the electron source. Here, applying a potential to the electron source of 3.9 kV with respect to ground, while the anode is operated at 4 kV with respect to ground, improves the density of the enclosed electrons by roughly 14 %. Applying the electron beam is also beneficial, but only improves the density by a maximum of 5 %. In certain conditions, the density "boosted" by an electron beam is smaller than the density measured without electron beam.

Summary

During the course of this thesis, several simulations were conducted in order to evaluate four strategies of injecting an electron beam into a Gabor lens. First, an auxiliary coil was investigated, which was supposed to bend the magnetic field lines so that injection was possible. This configuration breaks the symmetry in the magnetic field. Since it was shown later simulations that the auxiliary coil was not necessary, it was not installed during the injection experiments.

Second, a cusp-shaped magnetic field was investigated, breaking the transversal confinement of the Helmholtz coils. This led to increased electron losses. A third coil was added in cusp configuration in order to achieve a configuration close to the original one used by Gabor. Here, a confining region was supposed to act as an reservoir for electrons, while the cusp region was meant to allow easy insertion of electrons. Due to the cusp, electron losses were immense. The fourth configuration utilized a μ-metal shield in order to attenuate the transversal magnetic field by the Gabor lens. This strategy delivered promising results. Therefore, the shielded configuration was further investigated with the help of the particle-in-cell code bender. Adding space charge effects to the simulations revealed confined electrons that were filling the plasma volume nearly homogeneously.

With the help of the simulations, a new anode with four ports was designed and integrated into the Gabor lens test stand in Frankfurt. In order to prepare an electron source for the conditions in the Gabor lens, measurements in Bologna were scheduled and revealed necessary modifications to the electron source, such as adding a Wehnelt cylinder to the filament chamber. After the electron source was ready for the experiments, it was installed into the newly designed anode and a high-voltage terminal was designed to carry the power supplies necessary for the operation of the electron source.

In the following experimental period, the electron source was thoroughly characterised, especially the electron current with respect to several parameters. During a joint measurement session with the researchers from Bologna and Frankfurt, measurements concerning the electron beam assisted ignition behaviour were commissioned and various interesting results obtained, which will be the subject of further investigations. Additionally, the effect of the electron source on the ignition properties has been examined, especially the effect of the position of the electron source and the potential difference between source and anode on the ignition behaviour.

Finally, it was shown that the electron source can be used to ignite a sub-critical plasma and that the electron beam is increasing the number of electrons in the enclosed plasma, thus boosting the plasma density in certain regimes. Furthermore, it was shown that a potential difference between anode and source is beneficial to the enclosed electron density regardless of the electron beam being present or not.

Although promising results were obtained, further measurements need to be conducted in order to characterise the new system. The aforementioned measurements have to be repeated at different points on the work function, for example 4.5 kV and 5 kV with corresponding magnetic fields. Furthermore, the electron source needs to be upgraded in order to withstand higher temperatures and allow for a long, continuous operation. Therefore, a cooling system may be integrated into the electron source. Small scale water cooling systems are available commercially, but the integration of water cooling into the tiny electron source will prove to be challenging. Alternatively, the gate ring may be replaced by an insulating macor ring with metallised interior which is put on gate potential. If performed correctly, the metallisation is stable up to the melting temperature of the processed metal. A different strategy involves a smaller outer ring crafted from macor for the insulation and an inner ring composed of stainless steel for the gate potential. A cheaper and faster alternative could be replacing the alumina layer with a layer

of lacquer that is heat resistant up to 300 °C, which is commercially available. While this is probably not a long term solution, applying the lacquer is less complicated and elaborate than renewing a broken alumina layer. Therefore, the lacquer can deliver an intermediate solution.

In addition, the extracted current needs to be increased in order to check if the plasma can be ignited at a lower pressure than shown in these measurements. It is also interesting to investigate the effects of a focussed electron beam; therefore, some kind of focussing device should be added to the electron source.

Acknowledgements

During the course of this thesis, many people provided support, council and help with the various tasks necessary in order to perform the aforementioned measurements and simulations. First and foremost, I like to thank Prof. Dr. Holger Podlech for offering the opportunity and support to conduct the present research at IAP. Additionally, I thank Dr. Kathrin Schulte for supervising my work by being a lively counterpart in many discussions and providing council and assistance, especially during the modification phase of the experiment test stand. In addition, I would like to thank Dr. Santo Gammino and Dr. David Mascalli from INFN-LNS Catania as well as Dr. Fabrizio Odorici, Dr. Alessandro Montanari and Dr. Luciana Malferrari from INFN Bologna for the opportunity to conduct research in the frame of an international collaboration, for the fruitful discussions, and for the opportunity to visit Bologna and conduct measurements abroad in the scope of this thesis, which was a very challenging, pleasant and enjoyable experience.

In addition, I thank Dr. Oliver Meusel for assistance and council during all aspects of the thesis, especially during the measurements, Dr. Daniel Noll for his support during the simulations, especially concerning the code bender and Thomas Kelly, for the support with computer hardware in order to reduce overall simulation time. I furthermore thank all members of the NNP Group at IAP for vast, fruitful and critical discussions about many aspects of this thesis and the pleasant environment and social atmosphere that is present for every member of the group. Especially Bernhard Scheible, Stephan Klaproth, Virginia Britten and Katrin Thoma contributed to this enjoyable atmosphere. I also thank Daniel Born and Thomas Kelly for proofreading this thesis.

Finally and probably most importantly, I thank my parents for the support during my studies. Without their support, the studies and the research in this thesis would hardly have been possible.

List of Figures

List of Tables

Bibliography

[1] D. Gabor. A space charge lens for the focusing of ion beams. *Nature*, 160(4053):89–90, 1947.

[2] F. Odorici, L. Malferrari, A. Montanari, R. Rizzoli, D. Mascali, G. Castro, L. Celona, S. Gammino, and L. Neri. Injection of auxiliary electrons for increasing the plasma density in highly charged and high intensity ion sources. *Review of Scientific Instruments*, 87(2):02A740, 2016.

[3] J.A. Palkovic. *Gabor lens focussing and emittance growth in a low energy proton beam*. PhD thesis, University of Wisconsin-Madison, 1991.

[4] K. Schulte. *Studies on the focusing performance of a Gabor lens depending on nonneutral plasma properties*. PhD thesis, Goethe University, Frankfurt am Main, 2013.

[5] O. Meusel. *Fokussierung und Transport von Ionenstrahlen mit Raumladungslinsen*. PhD thesis, Goethe University, Frankfurt am Main, 2006.

[6] R.C. Davidson. *Physics of nonneutral plasmas*. Imperial College Press London, 2001.

[7] D. Noll. *Investigations on the Transport of High-Intensity Beams Using Particle-in-Cell Simulations*. PhD thesis, Goethe University, Frankfurt am Main, 2016.

[8] K. Schulte, M. Droba, O. Meusel, and U. Ratzinger. Optical diagnostic on Gabor plasma lenses. In *EPAC*, volume 8, page 3221, 2008.

[9] K. Schulte, M. Droba, S. Klaproth, O. Meusel, D. Noll, U. Ratzinger, and S. Yaramyshev. Alternative compact lebt design for the FAIR injector upgrade. *Proceedings of LINAC2014, Geneva, Switzerland*, pages 1013 – 1015, 2014.

[10] K. Schulte, M. Droba, B. Glaeser, S. Klaproth, O. Meusel, U. Ratzinger, et al. Studies on electron cloud dynamics for an optimized space charge lens design. *IPAC11, San Sebastian, Spain, THPS034*, 2012, 2011.

[11] K. Schulte, M. Droba, B. Glaeser, S. Klaproth, O. Meusel, U. Ratzinger, et al. Electron cloud dynamics in a Gabor space charge lens. *Proceedings of IPAC 2012*, pages 1164–1166, 2012.

[12] M.S. Chung and T.E. Everhart. Simple calculation of energy distribution of low-energy secondary electrons emitted from metals under electron bombardment. *Journal of Applied Physics*, 45(2):707–709, 1974.

[13] J.A. Palkovic, F.E. Mills, C. Schmidt, and D.E. Young. Gabor lens focusing of a negative ion beam. 1989.

[14] R. Fitzpatrick. Introduction to plasma physics. *The University of Texas at Austin*, page 242, 2008.

[15] A.S. Gilmour. *Klystrons, traveling wave tubes, magnetrons, crossed-field amplifiers, and gyrotrons*. Artech House, 2011.

[16] A. Angelucci, A. Ciorba, L. Malferrari, F. Odorici, R. Rizzoli, M. Rossi, V. Sessa, M.L. Terranova, and G.P. Veronese. Field emission properties of carbon nanotube arrays grown in porous anodic alumina. *Physica Status Solidi. C: Current Topics in Solid State Physics*, 6(10):2164–2169, 2009.

[17] D. Noll, M. Droba, O. Meusel, U. Ratzinger, K. Schulte, and C. Wiesner. The particle-in-cell code bender and its application to non-relativistic beam transport. *Proceedings of HB2014, East-Lansing, MI, USA*, pages 304–308, 2015.

[18] Nist: Cross sections of nitrogen gas. `http://physics.nist.gov/cgi-bin/Ionization/graph_new.pl?element=N2.0`. Accessed: 29.07.2015.

[19] D. Noll. private communication, 2016.

[20] F. Odorici. private communication, 2016.

[21] J. Pozimski. Messungen an einer Gabor-Plasma-Linse. 2011.

[22] S. Alzubaidi, O. Meusel, U. Ratzinger, K. Volk, C. Wagner, and H. Dinter. A control system for the FRANZ accelerator. *Proceedings of IPAC2014, Dresden, Germany*, pages 3134–3136, 2014.

[23] O. Meusel. private communication, 2016.

Erklärung nach § 30 (12) Ordnung für den Bachelor- und den Masterstudiengang:

Hiermit erkläre ich, dass ich die Arbeit selbstständig und ohne Benutzung anderer als der angegebenen Quellen und Hilfsmittel verfasst habe. Alle Stellen der Arbeit, die wörtlich oder sinngemäß aus Veröffentlichungen oder aus anderen fremden Texten entnommen wurden, sind von mir als solche kenntlich gemacht worden. Ferner erkläre ich, dass die Arbeit nicht - auch nicht auszugsweise - für eine andere Prüfung verwendet wurde.

Frankfurt, den